Analysis and design of Fault-Tolerant drives

Michele Dai Prè

Ph.D. Thesis

University of Padova

Department of Electrical Engineering

Electric Drives Laboratory

January 31, 2008

Contents

Abstract

The field of fault–tolerant applications is surely among the most exciting and potentially innovative modern research of the electrical motor where the design is freedom and new solution can be explored. The cost of the permanent magnets and the drives allow to develop new solution, in particular surface mounted permanent magnet machine with fractional–slot winding and reluctance motor assisted from the permanent magnet. The reliability of these machines allows to apply these motors into critical applications where the electrical or mechanical redundancy are required.
As regard this argument the literature compare the performance of different solution. In this thesis I have applied a different approach, in particular a mathematical model is combined with the finite element method. This approach allows to use the flexibility of the analytical model and the precision of the finite element method. The larger part of my research activity has regarded the motors with fractional–slot winding and the multi-phase machines. The final part of my thesis tells the activity developed during the period spent in ABB Corporate Research Sweden. The aim of my research was to design several solution of electric generators for wave energy, in particular the aim was to design the optimal system that is a compromise among the different component: generator, mechanical converter, inverter, etc..

Sommario

L'ambito delle applicazioni "fault-tolerant" é sicuramente tra i piú eccitanti e potenzialmente innovativi campi della ricerca moderna sui motori elettrici in quanto lascia molta piú libertá nella progettazione e permette di esplorare nuove soluzioni. Il ridursi del costo dei magneti permanenti e dei sistemi di controllo ha permesso di sviluppare nuove soluzioni a magneti permanenti superfiaciali con avvolgimenti frazionari e motori a riluttanza assistiti dai magneti permanenti. L'affidabilitá di questi motori li rende particolarmente adatti a quelle applicazioni in qui é richiesta una ridondanza meccanica o elettrica. A differenza della letteratura che si basa sul confronto delle prestazioni di alcune macchine specifiche, l'impostazione che si é voluto dare in questa tesi é stata quella di determinare dei modelli matematici integrati con l'analisi agli elementi finiti. Questo approccio permette di sfruttare la grande capacitá di calcolo dei modelli analitici e la precisione numerica degli elementi finiti per le sole soluzioni piú promettenti.
Tra le diverse strategie di progetto, si dato maggiormente spazio alle soluzioni di motori con cave frazionarie e di motori multifase.
Nella parte finale della tesi viene descritta l'attiviá svolta durante la breve parentesi all'ABB Corpoarte Research svedese. Questa mi ha permesso di affrontare le problematiche legate alla progettazione di generatori per energie rinnovabili, in particolare per produrre energia elettrica dalle onde marine. In questa ricerca, l'attenzione é stata rivolta alla progettazione dell'intero sistema, che ha richiesto un'ottimizzazione di piú componenti e non del solo generatore elettrico.

Chapter 1

Introduction

Fault-tolerant design refers to a method for designing a system so it will continue to operate, possibly at a reduced level (also known as graceful degradation), rather than failing completely, when some part of the system fails. That is, the system as a whole is not stopped due to problems either in the hardware or the software.

Fault-tolerance or graceful degradation is the property that enables a system to continue operating properly in the event of the failure of (or one or more faults within) some of its components. If its operating quality decreases at all, the decrease is proportional to the severity of the failure, as compared to a naively-designed system in which even a small failure can cause total breakdown. Fault-tolerance is particularly sought-after in high-availability or life-critical systems.

Fault-tolerance is not just a property of individual machines; it may also characterize the rules by which they interact.

When the system detects that it has made an error, roll-forward recovery takes the system state at that time and corrects it, to be able to move forward.

Within the scope of an individual system, fault-tolerance can be achieved by anticipating exceptional conditions and building the system to cope with them, and, in general, aiming for self-stabilization so that the system converges towards an error-free state. However, if the consequences of a system failure are catastrophic, or the cost of making it sufficiently reliable is very high, a better solution may be to use some form of duplication.

1.1 Dependability

The original definition of dependability for a system gathers the following attributes or non-functional requirements:

- Availability: readiness for correct service;
- Reliability: continuity of correct service;

- Safety: absence of catastrophic consequences on the user(s) and the environment;
- Security: the concurrent existence of confidentiality and integrity.

1.2 System Availability

System Availability is calculated by modeling the system as an interconnection of parts in series and parallel. The following rules are used to decide if components should be placed in series or parallel:

- If failure of a part leads to the combination becoming inoperable, the two parts are considered to be operating in series.
- If failure of a part leads to the other part taking over the operations of the failed part, the two parts are considered to be operating in parallel.

1.2.1 Availability in Series

As stated above, two parts X and Y are considered to be operating in series if failure of either of the parts results in failure of the combination. The combined system is operational only if both Part X and Part Y are available. From this it follows that the combined availability is a product of the availability of the two parts. The combined availability is shown by the equation below:

$$A = A_x * A_y \tag{1.1}$$

The implications of the above equation are that the combined availability of two components in series is always lower than the availability of its individual components.

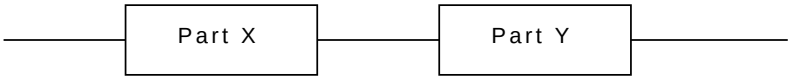

Figure 1.1: Availability in Series

1.2.2 Availability in Parallel

As stated above, two parts are considered to be operating in parallel if the combination is considered failed when both parts fail. The combined system is operational if either is available. The combined availability is shown by the equation below:

$$A = 1 - (1 - A_x)(1 - A_y) \tag{1.2}$$

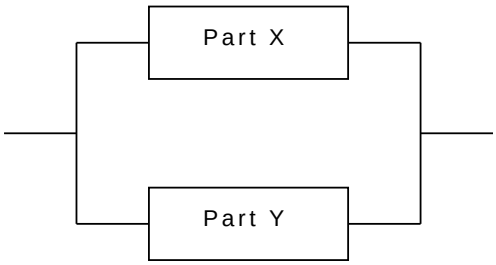

Figure 1.2: Availability in Series

1.2.3 Combined availability when the parts are operating in parallel

The combined availability of two components in parallel, (see (1.2), is always much higher than the availability of its individual components. Thus parallel operation provides a very powerful mechanism for making a highly reliable system from low reliability. For this reason, all mission critical systems are designed with redundant components.

1.3 Reliability

Reliability is the resistance to failure of a device or system.

Reliability engineers rely heavily on statistics, probability theory, and reliability theory. Many engineering techniques are used in reliability engineering, such as reliability prediction, Weibull analysis, thermal management, reliability testing and accelerated life testing. Because of the large number of reliability techniques, their expense, and the varying degrees of reliability required for different situations, most projects develop a reliability program plan to specify the reliability tasks that will be performed for that specific system.

The function of reliability engineering is to develop the reliability requirements for the product, establish an adequate reliability program, and perform appropriate analysis and tasks to ensure the product will meet its requirements. These tasks are managed by a reliability engineer, who usually holds an accredited engineering degree and has additional reliability–specific education and training.

1.3.1 Reliability requirements

For any system, one of the first tasks of reliability engineering is to adequately specify the reliability requirements. Reliability requirements address the system itself, test and assessment requirements, and associated tasks and documentation. Reliability requirements are included in the appropriate system/subsystem requirements

specifications, test plans, and contract statements.

1.3.2 System reliability parameters

Requirements are specified using reliability parameters. The most common reliability parameter is the mean–time–between–failure (MTBF), which can also be specified as the failure rate or the number of failures during a given period. These parameters are very useful for systems that are operated on a regular basis, such as most vehicles, machinery, and electronic equipment. Reliability increases as the MTBF increases. The MTBF is usually specified in hours, but can also be used with any unit of duration such as miles or cycles.

In other cases, reliability is specified as the probability of *"mission success"*. For example, reliability of a scheduled aircraft flight can be specified as a dimensionless probability or a percentage.

A special case of *"mission success"* is the single–shot device or system. These are devices or systems that remain relatively dormant and only operate once. Examples include automobile airbags, thermal batteries and power switch for electric grid. Single–shot reliability is specified as a probability of success, or is subsumed into a related parameter. Single–shot power switch for electric grid reliability may be incorporated into a requirement for the probability of hit.

In addition to system level requirements, reliability requirements may be specified for critical subsystems. In all cases, reliability parameters are specified with appropriate statistical confidence intervals.

1.4 Reliability modeling

This thesis doesn't explain the reliability modeling model and test requirements but in the following sections several concepts are shown.

Reliability modeling is the process of predicting or understanding the reliability of a component or system. Two separate fields of investigation are common:

1. The physics of failure approach uses an understanding of the failure mechanisms involved, such as crack propagation or chemical corrosion;

2. The parts stress modeling approach is an empirical method for prediction based on counting the number and type of components of the system, and the stress they undergo during operation.

For systems with a clearly defined failure time, the empirical distribution function of these failure times can be determined. This is done in general in an accelerated experiment with increased stress. These experiments can be divided into two main categories:

1. Early failure rate studies determine the distribution with a decreasing failure rate over the first part of the bathtub curve. Here in general only moderate

stress is necessary. The stress is applied for a limited period of time in what is called a censored test. Therefore, only the part of the distribution with early failures can be determined.
In so–called zero defect experiments, only limited information about the failure distribution is acquired. Here the stress, stress time, or the sample size is so low that not a single failure occurs. Due to the insufficient sample size, only an upper limit of the early failure rate can be determined. At any rate, it looks good for the customer if there are no failures.

2. In a study of the intrinsic failure distribution, which is often a material property, higher stresses are necessary to get failure in a reasonable period of time. Several degrees of stress have to be applied to determine an acceleration model. The empirical failure distribution is often parameterized with a Weibull or a log–normal model.

1.4.1 Reliability test requirements

Because reliability is a probability, even highly reliable systems have some chance of failure. However, testing reliability requirements is problematic for several reasons. A single test is insufficient to generate enough statistical data. Multiple tests or long–duration tests are usually very expensive. Some tests are simply impractical. Reliability engineering is used to design a realistic and affordable test program that provides enough evidence that the system meets its requirement. Statistical confidence levels are used to address some of these concerns. A certain parameter is expressed along with a corresponding confidence level: for example, an MTBF of 1000 hours at 90% confidence level. From this specification, the reliability engineer can design a test with explicit criteria for the number of hours and number of failures until the requirement is met or failed.

The combination of reliability parameter value and confidence level greatly affects the development cost and the risk to both the customer and producer. Care is needed to select the best combination of requirements. Reliability testing may be performed at various levels, such as component, subsystem, and system. Also, many factors must be addressed during testing, such as extreme temperature and humidity, shock, vibration, and heat. Reliability engineering determines an effective test strategy so that all parts are exercised in relevant environments. For systems that must last many years, reliability engineering may be used to design an accelerated life test.

Chapter 2

Theoretical basis

2.1 Base quantities and normalized parameters

For the sake of generality, the data are given in normalized values (small letters) referred to the base quantities defined in the following. In this way the results presented here can be extended to motors of any rated power. Moreover, the use of normalized values allows an easy comparison between different types of motor drive but with equal FW performance. The value of torque, electrical angular frequency and voltage exhibited under full load operation at the maximum speed of the constant torque region have been defined as base torque T_b, base angular frequency Ω_b and nominal voltage V_b. As far as the motor parameters and current is concerned their base values are fixed by considering the power balance

$$T_b \frac{\Omega_b}{p} = \frac{3}{2} V_b I_b \tag{2.1}$$

Then it results a base current

$$I_b = \frac{2T_b\Omega_b}{3pV_b} \tag{2.2}$$

a base inductance

$$L_b = \frac{3pV_b^2}{2T_b\Omega_b^2} \tag{2.3}$$

a base flux linkage

$$\Lambda_{mb} = L_b I_b = \frac{V_b}{\Omega_b} \tag{2.4}$$

The normalized quantities have been defined on the basis of these assumptions. With given nominal values of the motor, the normalized values are expressed by

$$t = T/T_b \tag{2.5}$$
$$i = I/I_b \tag{2.6}$$
$$v = V/V_b \tag{2.7}$$
$$\omega = \Omega/\Omega_b \tag{2.8}$$
$$\lambda_m = \Lambda_m/\Lambda_{mb} \tag{2.9}$$
$$l = L/L_b \tag{2.10}$$
$$\tag{2.11}$$

With this normalized values, each combination of PM flux linkage λ_m, two axis inductance l_d and l_q, then saliency ratio $\chi = l_d/l_q$ ($\xi = l_q/l_d$) and nominal current i_N satisfies:

the base torque	$t_b = 1$
at the base speed	$\omega_b = 1$
with a nominal voltage	$v_N = 1$

By applying the proposed normalization to the actual parameters of AC motors, their normalized value results within a typical range as illustrated in the following. The REL motor is characterized by a saliency ratio $\chi = l_d/l_q$, that strongly depends on the rotor structure. Generally it ranges from 3 to 7 with the normalized l_d varying from 0.3 to 0.9 and i_N from about 3.2 to 1.7. With an axially-laminated rotor a saliency ratio χ up to 20 can be obtained.
The SPM motor has a large and uniform equivalent airgap, since the PM relative permeability is close to unity. As a consequence the d- and q-axis inductances are equal and quite low. Typical normalized parameters of an SPM motor are $m = 10.95$, $l_d = l_q = 0.05 - 0.15$, $i_N = 1 - 1.1$. The SPM has a large airgap as well, thus the achievable saliency ratio $\chi = l_d/l_q$ is generally small and close to unity.
The IPM motor can exhibit two different rotor configurations: with circumferentially and with radially magnetized PM. Their typical saliency ratios are $\chi = l_d/l_q = 1.5 - 2.5$ and $\chi = 3 - 6$ respectively. The PM flux linkage m can be chosen from 0 to 1 and consequently the inductances and current values vary from those of an REL motor to an SPM motor.

2.1.1 General form of steady state motor drive equations

The steady state equations of the AC motor drive operation are studied with some simplifying assumptions:

1. the winding resistance is neglected;
2. the iron permeability is considered infinite so that the saturation effects are not taken into account;

3. no cross-coupling is assumed between the two axis;
4. the iron losses are neglected;
5. the PM irreversible demagnetization caused by the stator reaction is not considered, assuming a PM material with an appropriate coercive force and/or thickness.

The structure of an AC motor drive is shown in Fig. 2.1. It consists of a motor, an inverter and a control system forcing the current waveforms. In a well designed system, the rated motor current and voltage are within the inverter capabilities. Here we suppose that the rated current and voltage of the motor coincide with the inverter limits. Rated torque t_b is the maximum torque which can be obtained with rated current. The base angular frequency ω_b (in electrical radians per second) is the speed at which the drive delivers rated torque with rated voltage and current.

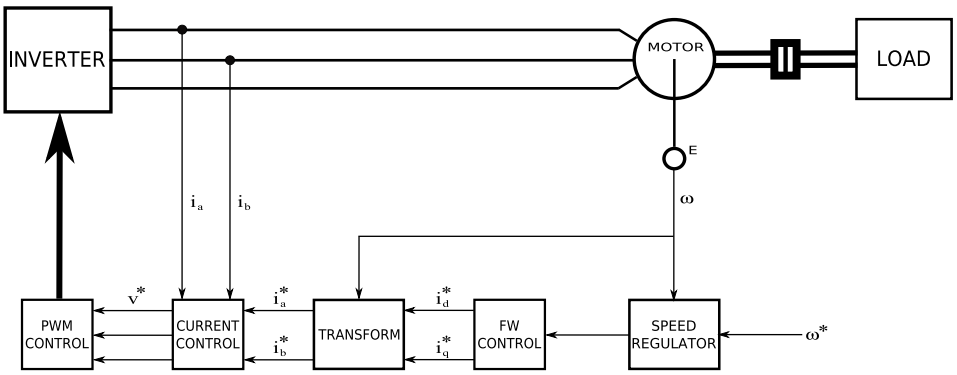

Figure 2.1: Electric drive scheme

2.1.2 Parameters to satisfy the base operating point

The first item yields a particular combination between the motor parameters [1]. In particular the nominal current I_N, and the d–axis and q–axis inductances L_d and L_q can be expressed as a function of the PM flux linkage Λ_m and the saliency ratio ξ. An example is reported in Fig. 2.2, according to $\xi = 6$, the values of I_N and L_q are reported as a function of Λ_m.

It is clear that the minimum value of nominal current is achieved with a PM flux linkage approaching unity. Ideally the minimum current results in $I_N = 1$ p.u. corresponding to a PM flux linkage $\Lambda_m = 1$ p.u.

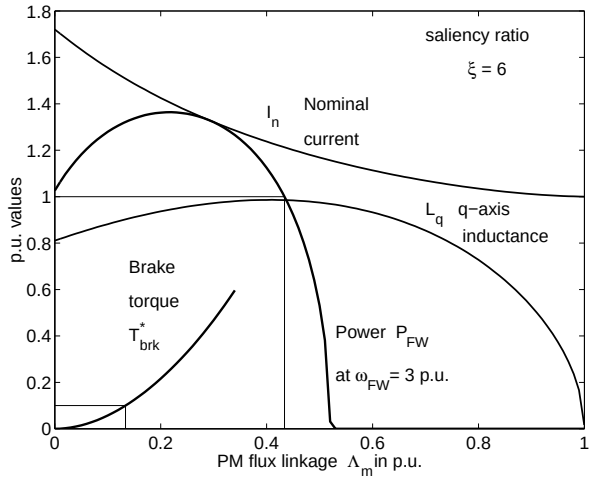

Figure 2.2: Parameters and performance of an IPM motor with $\xi = 6$

2.1.3 Parameters to satisfy the flux–weakening operating point

In order to satisfy the second item, only some combinations of motor parameters found above can be considered [1]. It has to be verified that the motor is able to exhibit a constant–power up to the flux–weakening speed ω_{FW}, that is, the output power has to be no lower than 1 p.u. up to the speed ω_{FW}. The flux–weakening power P_{FW} at ω_{FW} is computed for the various combinations of motor parameters, checking if $P_{FW} \geq 1$ p.u. is satisfied.

In the example of Fig. 2.2, the flux–weakening power P_{FW} computed at the speed $\omega_{FW} = 3$ p.u. is reported. It is worth noticing that a $P_{FW} \geq 1$ p.u. is achieved in the range $0 < \Lambda_m < 0.434$ p.u. As a consequence, the nominal current and the two axis inductances are limited as well. In order to achieve the lower nominal current, the higher flux linkage has to be selected, yielding a nominal current $I_N = 1.213$ p.u.

2.2 The star of slots

The star of slots is the phasor representation of the main EMF harmonic induced in the coil side of each slot. However, since it contains information of the winding distribution harmonics, the star of slots can be also used to represent all EMF harmonics induced in the coils and all MMF harmonics in the air–gap caused by the stator currents [2]. Information can be got about (**i**) harmonic orders, (**ii**) winding factor, and (**iii**) mutual inductance among the phases.

Let t be the machine periodicity, computed as the greatest common divisor ($G.C.D.$)

between the number of slots Q and the number of pole pairs p, which is

$$t = G.C.D.\{Q, p\} \tag{2.12}$$

The star of slots is characterized by Q/t spokes, each spoke containing t phasors. The slot angle is $\alpha_s = 2\pi/Q$ in mechanical radians and $\alpha_s^e = p\alpha_s$ in electrical radians (superscript e identifies the electrical angles). The stator slots are numbered consecutively and the corresponding phasors keep the same numeration. In order to represent the main star of slot (representing the main harmonic, whose order is equal to the pole pair), the consecutive phasors are drawn with an angular displacement α_s^e. Fractional–slot winding is feasible when the number of spokes is equal for each phase, that is, when Q/t is a multiple of the number of phases m.

An example is represented in Fig. 2.3 referring to a 24–slot 20–pole machine. The machine periodicity is $t = 2$: the star of slots has 12 spokes of 2 phasors each. The first 12 slots are in the same magnetic position of the following 12 slots.

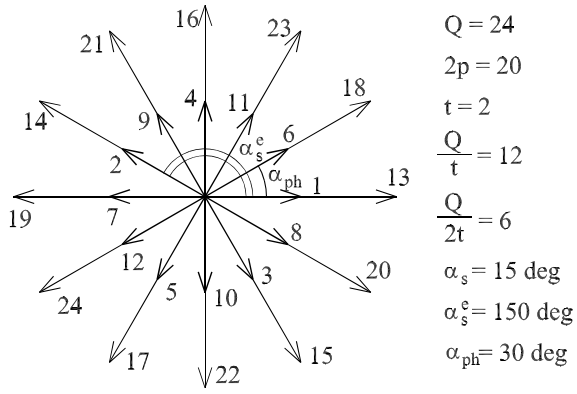

Figure 2.3: The star of slots of a 24–slot 20–pole machine

It is also useful to define:

- the **adjacent** phasors, such as the phasors 1 and 6 of Fig. 2.3. The angular displacement between them corresponds to the angle between two spokes:

$$\alpha_{ph} = t\alpha_s \tag{2.13}$$

- the **superimposed** phasors, such as the phasors 1 and 13 of Fig. 2.3. The difference between their reference number is equal to the number of spokes Q/t.
- the **opposite** phasors that are π radians out of phase, such as the phasors 1 and 7 of Fig. 2.3.

It is possible to demonstrate [2] that:

1. when Q/t is even the adjacent phasors are odd and even alternatively, and the superimposed phasors are all odd or all even.
2. when Q/t is odd the superimposed phasors are odd and even alternatively.
3. the opposite phasors (that exist only if Q/t is even) are both even or both odd, when $Q/(2t)$ is even, while they are one even and the other odd, when $Q/(2t)$ is odd.

These properties have important implications on the magnetic performance of the machine, as will be described in the following.

2.3 From double– to single–layer winding

Non–overlapped coil single–layer windings are proposed for fault–tolerant applications [3], in order to achieve a physical separation between the coils. Each coil is wound around a single tooth and separated from the others by a stator tooth, so that the phase–to–phase fault is very improbable.

From the design point of view, the single–layer winding can be achieved from a double–layer winding. The transformation from double– to single–layer winding is sketched in Fig. 2.4 referring to a 12–slot 10–pole surface–mounted PM (SPM) motor. Every one coil of the double–layer winding is removed and re–inserted into the stator according to the position of the coils of the same phase.

The star of slots of the double–layer winding 12–slot 10–pole SPM motor has 12 spokes of one phasor each (i.e. the first 12 phasors of the 24–slot 20–pole motor of Fig. 2.3). After the transformation into a single–layer winding all even phasors of the star of slots are removed, while only the odd phasors remain [4].

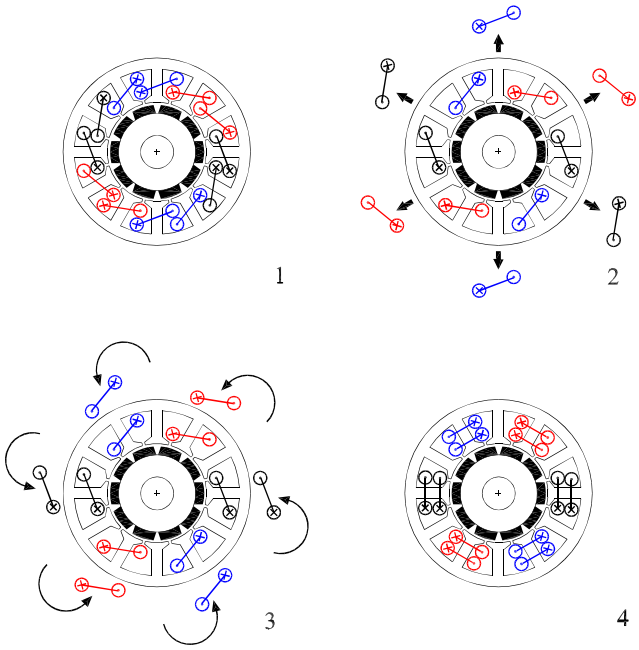

Figure 2.4: The basic idea of the transformation from double– to single–layer winding

2.3.1 Transformation constraints

The transformation is possible only if some geometrical and electrical constraints are satisfied [2].

As regards the **geometrical constraints**

1. the number of slots Q must be even;
2. the slot throw y_q must be odd (of course, in concentrated coil winding, in which $y_q = 1$, this constraint is inherently satisfied).

As regards the **electrical constraints**, once the machine periodicity t is computed as in (2.12), then

1. if t is even, the transformation is always possible. The machine exhibits different performance depending on the ratio Q/t is even or odd. Details will be given later.
2. if t is odd, the transformation is possible only if the ratio Q/t is even. In fact the number of coils that change their position has to be even.

Two examples of double– and single–layer fractional slot– winding are shown in Fig.2.5 and Fig.2.6. Other examples of this solutions are reported in [5–8].

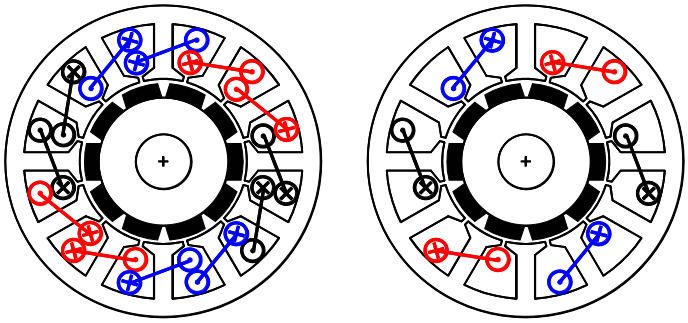

Figure 2.5: Three–phase 12–slot 8–pole PM motors with double– and single–layer winding.

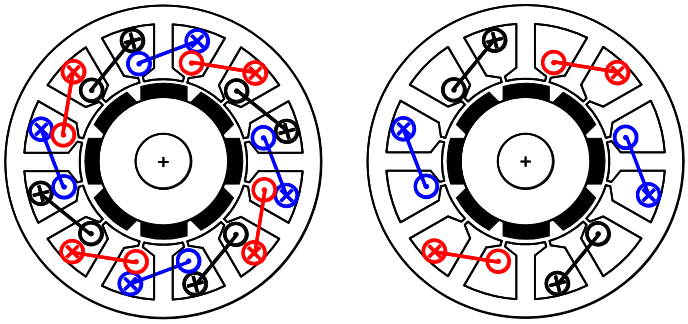

Figure 2.6: Three–phase 12–slot 10–pole PM motors with double– and single–layer winding.

2.4 Presence of MMF harmonics and their order

The fractional–slot winding motors are characterized by harmonic contents in the armature MMF distribution higher than that of the corresponding integer–slot winding motors. They can cause vibrations, when the MMF harmonic order matches the PM flux density harmonic order, and rotor losses [9]. Here, let us focus on the harmonic contents in the armature MMF distribution according to the star of slots theory and the choice of the number of slots Q and pole pairs p.

Various combinations are reported in Table 2.1. The upper part refers to double–layer windings, while the lower part refers to single–layer windings, which are obtained

by means of the transformation from the corresponding double–layer winding as described above.

Table 2.1 highlights the harmonic order (HO) of the armature MMF distribution. At first, the lower order of the MMF harmonic corresponds to the machine periodicity t and the other harmonics are multiple of t.

Referring to the double–layer winding, the MMF harmonics are only of odd order when Q/t even, so that the harmonic order can be expressed as $(2n-1)$ times t, where n is an integer positive number. This property holds with a single–layer winding too, provided that $Q/(2t)$ is even, thanks to the presence of the opposite phasors in the star of slots.

Conversely, with the other winding combinations, the order of the MMF harmonics are both odd and even. Then the harmonic orders are expressed as n times t. This result is referable to the odd number of spokes of the star of slots.

It has to be observed that, when the double–layer winding is transformed into a single–layer winding and Q/t is odd (the transformation is possible only if the machine periodicity t (2.12) is even), the machine periodicity decreases to $t/2$. Thus, harmonics of lower order (i.e. sub–harmonics) appear.

An example is reported in Fig. 2.7. The machine with 12 slots and 10 poles yields t=1, Q/t and $Q/(2t)$ even. Due to the low machine periodicity (t=1), the sub–harmonic of order ν=1 exists, as shown in the upper part of Fig. 2.7. Then, only harmonics of odd order exist (i.e. ν=5, 7, 11, 13, ...). When the double–layer winding is transformed into a single–layer one, the harmonics remain of the same order, but their amplitude increases. The winding factor of the main harmonic (i.e. of order ν=p=5) slightly increases.

The machine with 12 slots and 8 poles yields t=p=4 and Q/t odd. There are no sub–harmonics, but harmonics of odd and even order, multiply of 4 (i.e. ν=4, 8, 16, 20, ...). When the double–layer is transformed into a single–layer winding, the machine periodicity decreases to $t/2$=2. Various harmonics grow up, among them the sub–harmonics of order ν=2.

2.5 Winding factor

The winding factor can be graphically computed from the star of slots, as the ratio between the geometrical and the arithmetical sum of the phasors of the same phase. It can be computed for each harmonic order. In the following, some considerations are given for the winding factor k_w referring to the main harmonic (harmonic of order equal to the pole pair number p).

When all phasors of each phase are parallel, a unity winding factor is obtain. This occurs when the number of spokes of the star of slots are 3 or 6. In the other cases, the geometrical sum of the phasors is always lower than the arithmetical sum, and the winding factor is lower than 1. The main winding factor of fractional–slot winding can be computed as reported in [4].

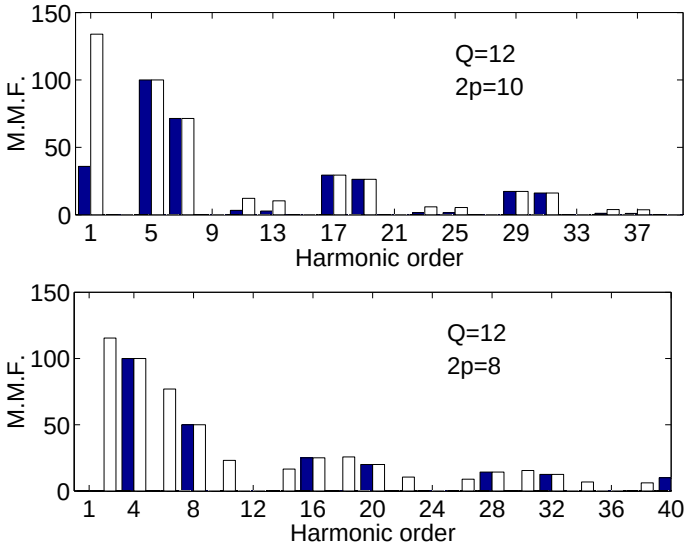

Figure 2.7: MMF harmonic contents of 12–slot 10–pole motor and 12–slot 8–pole motor respectively (black bars refer to double–layer winding, white bars refer to single–layer winding)

From the star of slots it is possible to verify that a single–layer winding can exhibit a winding factor even higher than that of the corresponding double–layer winding. It occurs when the number of spokes of the star of slots decreases. It is possible to demonstrate that this occurs when $Q/(2t)$ is even: the opposite phasors of the star of slots are both even and both odd [2]. Then, when the even phasors are removed, all spokes containing them are removed. As a consequence, the main k_w increases. This is generalized in Table 2.1.

2.6 Mutual inductance equal to zero

If the fractional–slot winding has to be designed for fault–tolerant applications a common requirement is that the mutual coupling among the phases is zero, i.e. M=0. This is to avoid the interaction between the healthy and the faulty phases.

To this purpose, windings with non–overlapped coils (i.e. with a unity coil throw $y_q = 1$) are firstly adopted.

Secondly, the winding of each phase can be split in couples of coils producing rectangular–shaped MMF distributions of opposite sign. The positive contribution of one coil is compensated by the negative contribution of the other coil. Therefore the resulting MMF distribution is zero in any point not embraced by these two coils. An example is shown in Fig. 7.13 that reports the armature MMF distribution due

Table 2.1: Harmonic order (HO) and winding factor (k_w) change for different combinations of slots and pole pairs

<table>
<tr><td colspan="4">Machine periodicity $t = G.C.D.\{Q, p\}$</td></tr>
<tr><td colspan="4">Feasibility: number of spokes per phase $Q/(mt)$ integer</td></tr>
<tr><td></td><td colspan="2">Q/t even</td><td>Q/t odd</td></tr>
<tr><td rowspan="3">Double Layer</td><td colspan="2">• Adjacent phasors are odd and even alternatively
• Superimposed phasors are all odd or all even
• HO: $(2n-1)t$
• Mutual inductance $M = 0$ when $y_q = 1$</td><td rowspan="3">• Superimposed phasors odd or even alternatively
• HO: nt
• $M \neq 0$</td></tr>
<tr><td>$Q/(2t)$ even</td><td>$Q/(2t)$ odd</td></tr>
<tr><td>• Opposite phasors are both even or both odd</td><td>• Opposite phasors are one even and the other odd</td></tr>
<tr><td colspan="4">Transformation from double– to single–layer winding
Geometrical constraints: Q even and y_q odd</td></tr>
<tr><td rowspan="2">Single Layer</td><td rowspan="2">• k_w increases
• HO: $(2n-1)t$
• $M = 0$ remains when $y_q = 1$</td><td rowspan="2">• k_w unchanged
• HO: nt
• $M \neq 0$</td><td>(only if t is even)</td></tr>
<tr><td>• k_w unchanged
• HO: $nt/2$
• $M \neq 0$</td></tr>
</table>

n is an integral positive number

to only one phase of a 12–slot 10–pole machine and a 12-slot 8–pole machine. In the upper case, the MMF is different from zero only where there are the supplied coils. In the lower case, the MMF distribution is never equal to zero, which means that a flux is linked also by the coils that are not supplied. Further examples are in [10] and in [11] where a 36–slot 30–pole motor and a 36–slot 42–pole PM motor have been considered respectively.

2.6.1 General rule to achieve M=0

A general rule can be found to achieve a winding with no coupling among the phases. It occurs when Q/t is even with a double–layer winding, and when $Q/(2t)$ is even with a single–layer winding. This general result is also reported in Table 2.1.

The examples mentioned above (12–slot 10–pole, 36–slot 30–pole, and 36–slot 42–pole motors) belong to this group. In fact all of them have y_q=1 and Q/t even. In the case of single–layer winding, they show $Q/(2t)$ even so as M=0 as well.

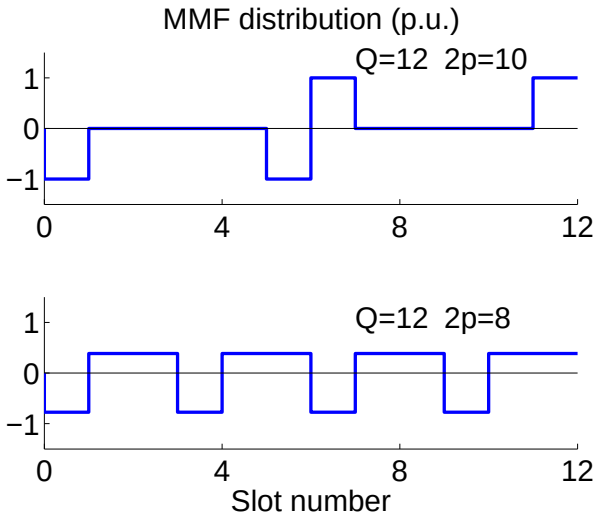

Figure 2.8: Armature MMF distribution of a 12–slot 10–pole (with $M = 0$) and of a 12–slot 8–pole motor (with $M \neq 0$)

2.7 Magnetic loading against the PM

In this section, the magnetic loading due to stator currents of a fractional–slot winding motor is compared with that of a full–pitch winding motor, characterized by one slot per pole per phase, i.e. q=1. For the sake of a correct comparison, the two motors have to exhibit a winding distribution with the same main harmonic. This is achieved by rearranging the number of series conductors per slot n_c of the fractional–slot winding according to the main winding factor k_w and the slot number, yielding

$$n_{c(f)} = n_{c(i)} \frac{Q_{(i)}}{Q_{(f)}} \frac{k_{w(i)}}{k_{w(f)}} \tag{2.14}$$

where subscript (f) refers to fractional–slot winding, while subscript (i) refers to integer–slot full–pitch winding. Eqn. (2.14) holds for both double– and single–layer windings.

Adopting non–overlapped coil windings, each coil contributes to the stator magnetic potential independently. Then, referring to the time instant in which one phase current assumes the maximum value $\hat{I}$ and the other two phases the value $-\hat{I}/2$, the peak value of the stator magnetic potential is given by

$$\hat{U}_s = \frac{n_{c(f)}}{2} \hat{I} \tag{2.15}$$

for a double–layer winding. This value doubles for a single–layer winding. For the sake of comparison, the peak value of the stator magnetic potential of full–pitched

winding corresponds to

$$\hat{U_s} = n_{c(i)} \frac{Q_{(i)}}{m2p} \hat{I} \tag{2.16}$$

that reduces to $n_{c(i)}\hat{I}$ when q=1. Let us remember that the number of conductors per slot has to be rearranged as in (2.14) when integer– and fractional–slot windings are compared.

Then (2.15) is useful during the design of the machine: it allows to identify the maximum PM demagnetization. Letting g and t_m be the air–gap and the PM thickness respectively, the peak flux density due to stator currents is given by

$$\hat{B}_g \approx \mu_0 \frac{\hat{U_s}}{g + t_m} \tag{2.17}$$

2.8 Magnetizing inductance

In this section, the magnetizing inductance of a fractional–slot winding motor is compared with that of a full–pitch winding motor, characterized by one slot per pole per phase, i.e. q=1. The main difference in the inductance of the various configurations is mainly due to the magnetizing rather than the leakage inductance, so that the former is investigated here.

The magnetizing inductance of the machine is computed from the magnetic energy when the unique source of magnetic field is the stator current. The PMs are de–energized (demagnetized) and only the stator coils are supplied, then the magnetic energy is computed in the air–gap and in the volume occupied by the de–energized PMs [12].

It is interesting to consider the magnetic energy, to which the magnetizing inductance is proportional, as the sum of the contributions of the various MMF harmonics. The superposition of the effects of the magnetic energy terms is possible only because the MMF harmonics form a series of orthogonal functions. In comparing integer– and fractional–slot windings, the magnetic energy term corresponding to the main harmonic (of order $\nu = p$) is the same due to gauge taken in (2.14). The other magnetic energy terms correspond to all but the main magnetic potential harmonics (i.e. of order $\nu \neq p$) and vary according to the harmonic contents of the winding distribution.

Referring to the peak value of the air–gap flux density due to the stator currents, i.e. $\hat{B}_g$ of (2.17), the average magnetic energy density can be expressed as

$$w_m = \frac{1}{2\mu_0} \left[\frac{1}{Q/t} \sum_{k=1}^{Q/t} \left(\frac{B_k}{\hat{B}_g} \right)^2 \right] \hat{B}_g^2 \tag{2.18}$$

where B_k represents the air–gap flux density in front of the kth tooth. The computation can be done at the time instant in which one phase current is $\hat{I}$ and the others are $-\hat{I}/2$. It is easy to verify that in full–pitch integer–slot windings, the term within

the square brackets is equal to 0.5 with q=1, while this term decreases as the number of slot per pole per phase q increases.

In fractional–slot windings with non–overlapped coil ($y_q = 1$), each coil contributes independently to the air–gap flux density in front of the corresponding tooth. Then, it can be verified that the term within the square brackets of (2.18) is equal to 0.5 as well. Thus, in comparing the full–pitch winding with q=1 and the fractional–slot winding with y_q=1, the ratio between the magnetizing inductances corresponds to the ratio between the peak air–gap flux density squared, i.e. $\hat{B}_g^2$.

When a single–layer winding is adopted, the air–gap flux density becomes double, but the energized air–gap volume halves, with respect the double–layer winding. Thus, the magnetic energy and then the magnetizing inductance become double too.

Due to the non–ideal paths of the flux density lines, the effective increment is slightly lower. In the finite element analysis of the two configurations under test, see Fig. 2.9, it has been computed an increase of the magnetic energy in the air–gap volume of almost 85 %. Anyways, (2.18) gives preliminary information of the influence of the slot and pole combination on the magnetizing inductance.

Due to the moderate variation of the slot leakage inductance (whose value is comparable with that of the magnetizing inductance in an SPM machine), the variation of the total phase inductance of the two motors of Fig. 2.9 results lower. It has been computed that the inductance of the single–layer winding motor is 50 % higher than the inductance of the double–layer winding. The experimental test confirms substantially the finite element computation: an increase of 59 % has been measured.

Finally, let us remember that a high magnetic energy (and magnetizing inductance) means a lower power factor, but also a reduced short–circuit current. This is a further requirement in fault–tolerant applications.

2.9 Stator yoke flux density

A characteristic of several fractional–slot machines with double–layer winding is that only a portion of the stator yoke is interested by the flux produced by the stator current. Fig. 2.9(a) shows the flux map of a 12–slot 10–pole motor due to the stator currents only (PMs have been de–energized). The stator yoke is only partially interested by the flux of the stator winding and these parts of the stator yoke carry the flux of the PM only.

In order to draw generalizations from this result, this happens adopting a double–layer winding in which adjacent teeth are wound by coils of the same phase but with opposite polarity. In the corresponding star of slots each phasor has opposite and following phasors that are adjacent, i.e. $\alpha_s^e = \pi \pm \alpha_{ph}$. This is the case of 12–slot 10–pole machine or of 24–slot 20–pole machine, shown in Fig. 2.3. Rearranging this equation, one obtains

$$2p = Q \pm 2t \tag{2.19}$$

An immediate consequence of these considerations is that a portion of the stator

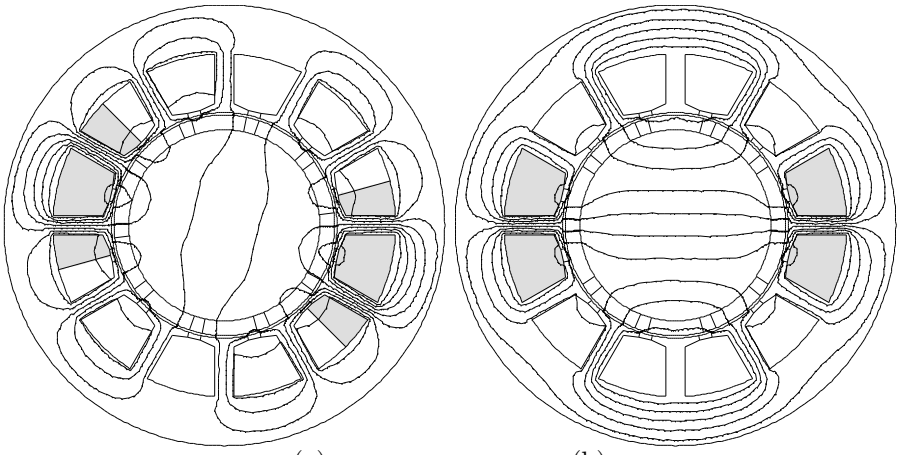

Figure 2.9: Flux plot of a 12–slot 10–pole motor, with (a) double– and (b) single–layer winding

yoke can be reduced, yielding an additional space for clamping the laminations or for improving the cooling of the coils. The stator can be even split in pieces that are wound separately and then assembled together. In [13] a different magnetic loading in the stator teeth has been also observed, so as unequal teeth have been designed.

2.10 Examples

Some common combinations of number of poles $2p$ and slots Q are reported in Table 2.2. All combinations refer to a PM machine with a number of phases m=3 and to a slot throw y_q=1. The winding factor k_w, the machine periodicity t, and the ratio Q/t are reported for each combination. According to the values of t and Q/t, as depicted in Section 2.3, Table 2.2 marks if the single–layer winding (S.L.) is possible or not.

The even values of Q/t are reported in bold type. Since y_q=1, the configurations with Q/t even yield a mutual inductance M equal to zero. In addition, if Q/t is multiple of 4, the property $M = 0$ remains also after the transformation into a single–layer winding. This is the case of the 12–slot 10–pole configuration (an asterisk has been added in Table 2.2).

The second–last column of Table 2.2 reports the peak of the stator magnetic potential $\hat{U}_s$, as a percentage of the corresponding potential of the full–pitch q=1 winding. It is the ratio between (2.15) and (2.16). For instance, the value of the 9–slot 8–pole motor is compared with that of the 24–slot 8–pole motor (where the number 24 comes from $2pqm$=8·1·3). In all comparisons it is assumed that the stator

bore diameter and length remain the same, as well as the current amplitude, while $n_{c(f)}$ are adjusted as in (2.14). Therefore the average torque remains the same for each configuration.

For the sake of comparing solutions with different pole number, it is worth to consider that the number of conductors per slot $n_{c(i)}$ varies in inverse relation to p, to have q=1. Thus, for given current, the stator magnetic potential $\hat{U}_s$ (2.16) also varies in inverse relation to p. The percentage numbers reported in Table 2.2 should be divided by p for an overall comparison.

Finally, the last column of Table 2.2 reports the magnetic energy, expressed as the percentage of the corresponding energy of the full–pitch q=1 winding motor. Once again the comparison makes sense for the same number of poles. For the sake of comparing solutions with different p, the percentage values have to be divided by p^2.

Table 2.2: Combinations of poles and slots, winding factor, MMF peak and magnetic energy (all values for m=3 and y_q=1)

$2p$	Q	k_w	t	Q/t	S.L.	$\hat{U}_s$ (%)	W_m (%)
2	3	0.866	1	3	—	115	133
4	3	0.866	1	3	—	231	534
	6	0.866	2	3	yes	115	133
6	9	0.866	3	3	—	115	133
8	6	0.866	2	3	yes	231	534
	9	0.945	1	9	—	141	199
	12	0.866	4	3	yes	115	133
	15	0.711	1	15	—	113	127
10	9	0.945	1	9	—	176	310
	12	0.933	1	**12***	yes	134	180
	15	0.866	5	3	—	115	133
	18	0.735	1	**18**	yes	113	128
12	9	0.866	3	3	—	231	534
	18	0.866	6	3	yes	115	133
14	12	0.933	1	**12***	yes	188	352
	15	0.951	1	15	—	147	217
	18	0.902	1	**18**	yes	129	167
	21	0.866	7	3	—	115	133

Even Q/t are printed in bold type.
When $Q/(2t)$ is even an asterisk is added.

Part I

Mechanical Redundancy

Chapter 3

Definitions

Redundancy in engineering is the duplication of critical components of a system with the intention of increasing reliability of the system, usually in the case of a backup or fail-safe.

In many safety-critical systems, such as fly-by-wire aircraft, some parts of the control system may be triplicated. An error in one component may then be out-voted by the other two. In a triply redundant system, the system has three sub components, all three of which must fail before the system fails. Since each one rarely fails, and the sub components are expected to fail independently, the probability of all three failing is calculated to be extremely small.
Three example of mechanical redundancy are shown in the following section.

3.1 Automotive

The electric power steering EPS (see Fig. 3.1) presents several advantages over the conventional hydraulic power steering, e.g. improved fuel economy, ability to vary the assist as a function of vehicle speed, ability to provide assist even when the engine is off, simplified engine accessory drive, modular assembly, easily tunable steering characteristics, and elimination of the hydraulic fluid. On the other hand a fault-tolerant electric motor drive with mechanical redundancy is required. A flexible motor configuration is proposed to increase the redundancy against motor failures. It is recommended that the use of direct-drive multiple motors on the same shaft improves redundancy Fig. 3.4.

For safety's sake, a redundant system is adopted, in which all the electric components of the EPS are doubled. In particular, the solution adopted by the authors makes provision for two batteries, two inverters, two feeding circuits and two electric motors driving the steering–rack. Fig. 3.4 shows the two rotating electric motors that are fitted on the same shaft. They drive the linear movement of the steering–rack by means of a ball–screw system.

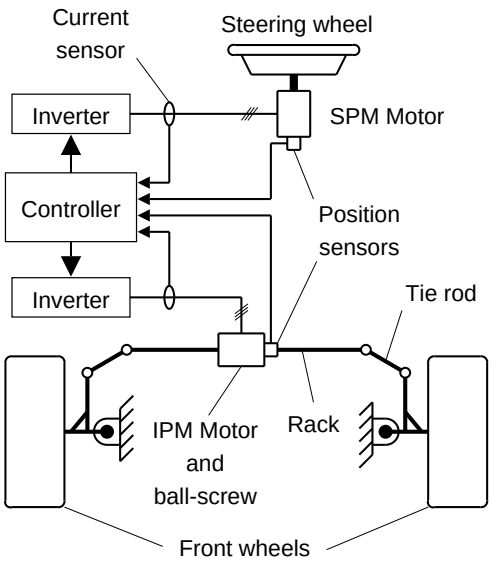

Figure 3.1: Scheme of the steer-by-wire system

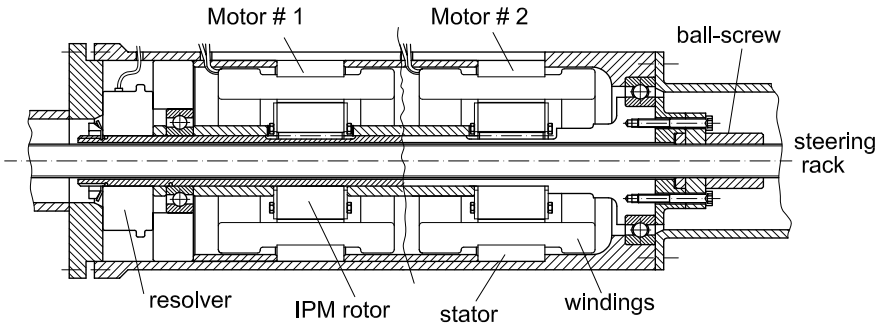

Figure 3.2: Electric power steering rack highlighting the two motors and the ballscrew system

The steering functions are then guaranteed even in case of failure of one of the two drives or motors, although with reduced performance. Such a reduction is a function of the type of failure. At worst, a complete loss of one inverter or one motor is considered, so that only one healthy motor drive can operate. The corresponding EPS performance (force, acceleration and speed) are halved, and full operations are temporarily allowable.

However, a further aspect has to be considered: it is essential that the faulty IPM machine does not brake so as to jam the steer mechanism and the remaining healthy motor has to be able to move the steering–rack. Braking torque may occur in PM motors since a short–circuit current is sustained by the back EMF induced by the PM buried in the rotor.

3.2 Marine Propulsion

A diesel-electric power station secures multiple redundancy as shown in Fig. 3.3. In the event of malfunction of a main engine adequate power remains available for the ship to operate safely under any circumstances. Plant reliability is further enhanced by a reduced number of ancillary support systems for the engines. Twin electric propulsion drives secure redundancy and get-you-home capability. Attractions of Electric Propulsion Operations in heavy weather in restricted waters without tug assistance or during dynamic positioning are supported by the impressive torque characteristics, also at low speeds, of the electric propulsion drive. Machinery availability and fire safety are enhanced by the ability to arrange the key power station elements in separate self-sufficient watertight compartments.

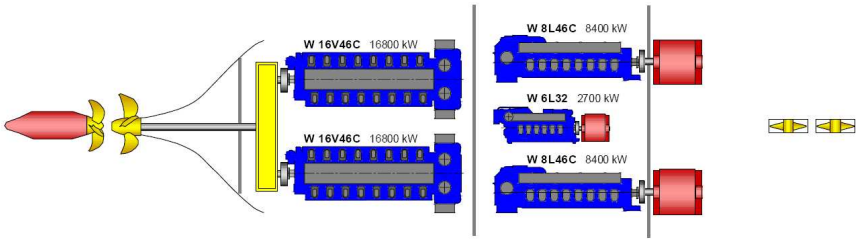

Figure 3.3: Marine propulsion

3.3 Aircraft System

The aircraft utility hydraulic system can operate by splitting the production utility system, with its two interconnected flow paths, single reservoir and redundant hydraulic pumps (one driven by each engine or electric motor) or thanks to two distinct systems with two totally independent flow paths, separate reservoirs and non-redundant hydraulic pumps (each driven by only one engine or electric motor). The second one insured that an actuator failure in one of the thrust vectoring nozzles would not result in a complete loss of the utility hydraulic system.

The only common connection between the utility systems is at the emergency generator. A priority valve selects which utility system powers the emergency generator.

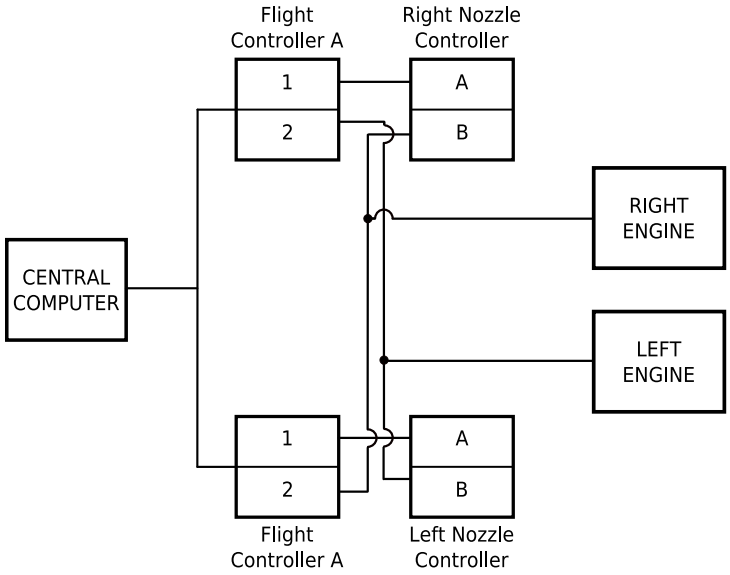

Figure 3.4: Aircraft system

For redundancy, each nozzle has been designed to accommodate up to two independent hydraulic sources, although only a single utility source is used per nozzle. The aircraft's Utility 1 system drives the left nozzle's divergent actuators, while Utility 2 powers the right nozzle's actuators. Each utility supply line bifurcates into the associated nozzle's dual-line system at the nozzle/aircraft interface.

Chapter 4

Fault Analysis

4.1 Analysis of a three–phase short–circuit

Among the different faults that may occur on the motor, the more dangerous condition is considered the three–phase short–circuit [14]. Because of the PM flux linkage, the IPM motor works as a brake, limiting the steering movement.

The analysis is carried out in the synchronous $d-q$ reference frame. The voltages are given by

$$\begin{aligned} v_d &= Ri_d + \frac{d\lambda_d}{dt} - \omega\lambda_q \\ v_q &= Ri_q + \frac{d\lambda_q}{dt} + \omega\lambda_d \end{aligned} \tag{4.1}$$

where the d– and q–axis flux linkages are $\lambda_d = \Lambda_m + L_d i_d$ and $\lambda_q = L_q i_q$ respectively, in the hypothesis of magnetic linearity.

In the case of a three–phase short–circuit, $v_d = v_q = 0$. The i_d and i_q currents are computed from (4.1). Fig. 4.1 shows the i_d and i_q current behaviors versus time during a three–phase short–circuit. The IPM motor data used in the simulation are reported in the Appendix. Fig. 4.2 shows the i_d and i_q currents in the $(i_d,\ i_q)$ plane. The dashed line represents the ellipse trajectory described by the currents when the stator resistance is zero. Conversely, the solid line refers to the case with a resistance different from zero. The currents move from their initial value I_{d0} and I_{q0} given by the operating point before the fault (and highlighted by the circle in Fig. 4.2) towards the steady–state short–circuit value, defined by

$$I_{d,shc} = -\frac{\omega^2 L_q \Lambda_m}{R^2 + \omega^2 L_d L_q} \tag{4.2}$$

and

$$I_{q,shc} = -\frac{\omega \Lambda_m R}{R^2 + \omega^2 L_d L_q} \tag{4.3}$$

and the amplitude is

$$I_{shc} = \frac{\sqrt{(\omega^2 L_q \Lambda_m)^2 + (\omega \Lambda_m R)^2}}{R^2 + \omega^2 L_d L_q} \tag{4.4}$$

In the example of Fig. 4.1 and Fig. 4.2, it corresponds to $I_{d,shc} = -3.85$ p.u. and $I_{q,shc} = -0.083$ p.u.

4.1.1 Simplified study with null stator resistance

In the case of zero resistance, the behaviors of the two–axis currents are given by

$$i_d(t) = -\frac{\Lambda_m}{L_d} + \left(I_{d0} + \frac{\Lambda_m}{L_d}\right)\cos(\omega t) + \left(\frac{L_q}{L_d} I_{q0}\right)\sin(\omega t) \tag{4.5}$$

and

$$i_q(t) = -\frac{L_d}{L_q}\left(I_{d0} + \frac{\Lambda_m}{L_d}\right)\sin(\omega t) - I_{q0}\cos(\omega t) \tag{4.6}$$

where I_{d0} and I_{q0} are the initial values of the d– and q–axis currents. In the example they are $I_{d0} = -0.686$ p.u. and $I_{q0} = 0.877$ p.u.. At last, the steady–state short–circuit value coincides with the point ($I_{d,shc} = -\Lambda_m/L_d$, $I_{q,shc} = 0$). The ratio Λ_m/L_d is called machine characteristic current [15].

In the case of null stator resistance, the behaviors of the two-axis currents are given by

$$i_d(t) = -\frac{\Lambda_m}{L_d} + \left(i_{d0} + \frac{\Lambda_m}{L_d}\right)\cos(\omega t) + \left(\frac{L_q}{L_d} i_{q0}\right)\sin(\omega t) \tag{4.7}$$

and

$$i_q(t) = -\frac{L_d}{L_q}\left(i_{d0} + \frac{\Lambda_m}{L_d}\right)\sin(\omega t) - i_{q0}\cos(\omega t) \tag{4.8}$$

where i_{d0} and i_{q0} are the initial values of the d-axis and the q-axis currents. The steady-state value coincides with $i_{d,shc} = -\Lambda_m/L_d$ and $i_{q,shc} = 0$ when the stator resistance is null.

The minimum d–axis current is important since it represents the peak negative current that may demagnetize the PM. As a consequence, the IPM motor has to be designed so as to sustain this current. It is computed as

$$I_{d,min} = -\frac{\Lambda_m}{L_d} - \sqrt{\left(I_{d0} + \frac{\Lambda_m}{L_d}\right)^2 + \left(\frac{L_q}{L_d} I_{q0}\right)^2} \tag{4.9}$$

In the reported example it is $I_{d,min} = -10$ p.u. Its amplitude is more than nine times the nominal current (see Appendix), that is, higher than 2.5 times the machine characteristic current Λ_m/L_d. Assuming the nominal amplitude of the initial current, the worst case is with q–axis current only, that is, $I_{q0} = I_N$ and then $I_{d0} = 0$. In

this case the ideal ellipse exhibits the largest area, and the minimum d–axis current becomes

$$I_{d,min} = \frac{-\Lambda_m - \sqrt{\Lambda_m^2 + (L_q I_N)^2}}{L_d} \tag{4.10}$$

reaching $I_{d,min} = -11.58$ p.u. in the considered example.

If the PM flux linkage is higher than the initial q–axis flux linkage, i.e. $\Lambda_m >> (L_q I_N)$, then the minimum d–axis current can be approximated as $I_{d,min} \approx -2\Lambda_m / L_d$. Conversely, in the case of a reluctance motor, where $\Lambda_m = 0$, the minimum d–axis current becomes $I_{d,min} = -\xi I_N$.

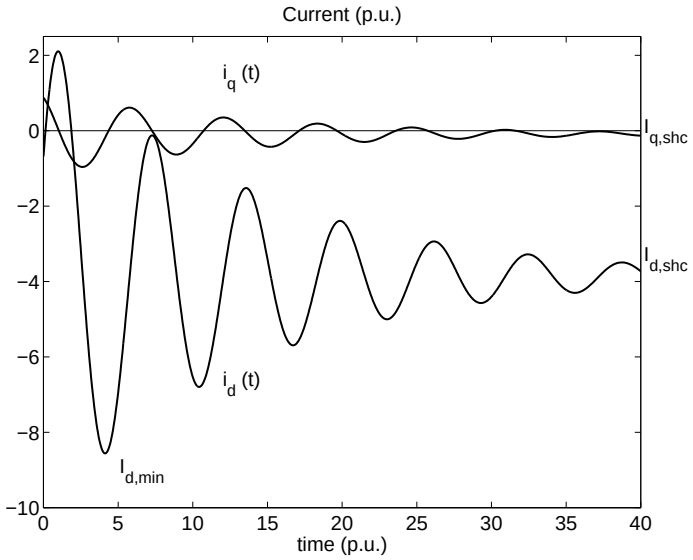

Figure 4.1: Short–circuit current behavior of the IPM motor whose parameters are reported in the Appendix

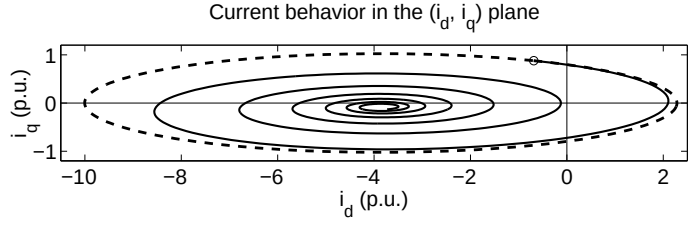

Figure 4.2: Short–circuit current trajectory in the (i_d, i_q) plane

4.2 Steady–state braking torque

The analysis of the steady–state braking torque is carried out in the synchronous $d-q$ reference frame. The voltage equations are expressed by (4.1) without derivatives and with $v_d = v_q = 0$. The steady–state braking torque [15] results in

$$T_{brk} = -\frac{3}{2} p R \Lambda_m^2 \, \omega \, \frac{R^2 + \omega^2 L_q^2}{(R^2 + \omega^2 L_d L_q)^2} \tag{4.11}$$

and the short–circuit current amplitude is obtained by (4.2) and (4.3), resulting in

$$I_{shc} = \frac{\sqrt{(\omega^2 L_q \Lambda_m)^2 + (\omega R \Lambda_m)^2}}{R^2 + \omega^2 L_d L_q} \tag{4.12}$$

It is possible to verify that the short–circuit current always increases with the speed ω, approaching Λ_m / L_d.

A typical behavior of the braking torque (negative with the motoring convention) and the short–circuit current are shown in Fig. 4.9 as a function of the motor speed. It is worth noticing that a non appropriate choice of the motor may cause a braking torque even higher than the rated torque. Its maximum is twice the rated torque, with the IPM motor data reported in the Appendix.

4.2.1 Maximum braking torque

The maximum amplitude of T_{brk} is computed by equating the derivative of (4.11) with respect to the speed ω to zero. The maximum braking torque results in

$$T^*_{brk} = \frac{3}{2} p \frac{\Lambda_m^2}{L_q} f(\xi) \tag{4.13}$$

and it occurs at the speed

$$\omega^* = \frac{R}{L_q} \sqrt{\chi} \tag{4.14}$$

where the function $f(\xi)$ is

$$f(\xi) = \sqrt{\chi} \frac{1 + \chi}{\left(1 + \dfrac{\chi}{\xi}\right)^2} \tag{4.15}$$

with

$$\chi = \frac{1}{2} \left[3(\xi - 1) + \sqrt{9(\xi - 1)^2 + 4\xi} \right] \tag{4.16}$$

It is worth noticing that $f(\xi)$ in (4.15) is only a function of the saliency ratio $\xi = L_q / L_d$. Its behavior is reported in Fig. 4.4. In the range between $\xi = 2$ and $\xi = 6$, such a function can be approximated by the straight line $f(\xi) \approx \xi - 1$, that is shown in the same Fig. 4.4 by a dashed line.

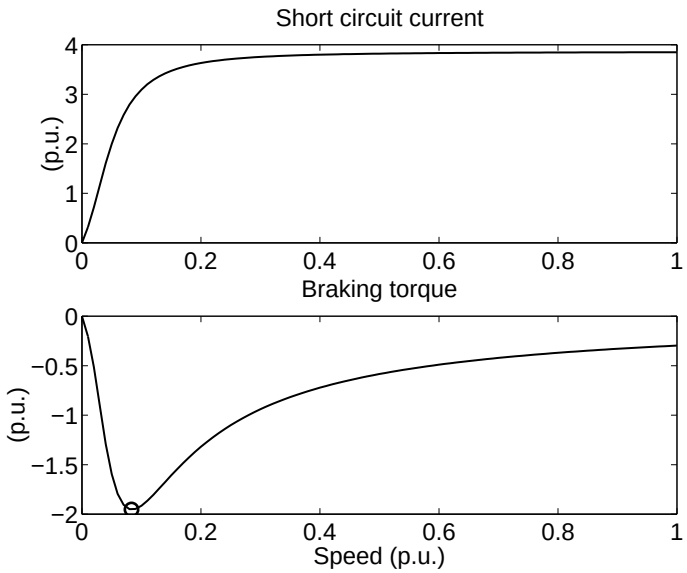

Figure 4.3: p.u. braking torque and p.u. current vs. p.u. speed

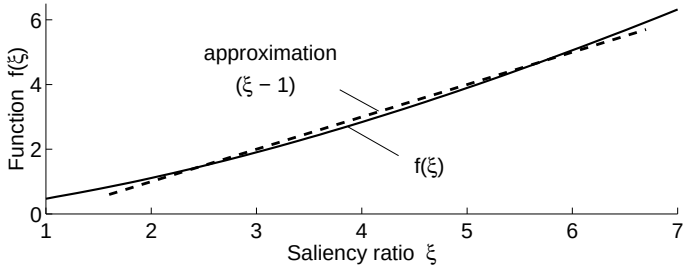

Figure 4.4: The function $f(\xi)$

4.3 Examples

Some examples are reported referring to SPM and IPM motors, whose the p.u. value of the parameters are reported in Table 4.1.

Table 4.1: p.u. value of the PM motor parameters

	IPM #1	IPM #2	SPM #1	SPM #2	
Λ_m	0.8	0.15	0.98	0.707	PM flux linkage
L_q	0.744	0.824	0.2	0.5	q-axis inductance
L_d	0.186	0.206	0.2	0.5	d-axis inductance
ξ	4	4	1	1	saliency ratio
R	0.05	0.05	0.05	0.05	resistance
I_n	1.052	1.632	1.02	1.414	nominal current
ω	1	1	1	1	speed

The p.u. parameters are normalized with respect the mechanical power, thus all the motors exhibit a unity torque at unity speed, when they are fed with nominal current and unity nominal voltage. In particular, SPM motors are characterized by $L_d = L_q = \Lambda_m\sqrt{1-\Lambda_m^2}$ and $I_n = 1/\Lambda_m$.

Fig. 4.5 and Fig. 4.6 show the i_d and i_q current behaviors computed from (4.1) during a three–phase short–circuit, referring to the SPM motors #1 and #2. Such behaviors are reported versus time and in the i_d–i_q plane. The dashed line represents the ideal ellipse described by the currents when the stator resistance is null, while the solid line refers to the case with a finite value of resistance.

Similar results are reported in Fig. 4.7 and Fig. 4.8, referring to the IPM motors #1 and #2.

4.4 Selection of the IPM motor parameters

The choice of the IPM motor parameters is determined by various requirements, often yielding different results. Such requirements are summarized hereafter, adopting the p.u. values in order to extend the result to motor drives of any power.

i. The motor has to satisfy the base operating point. This corresponds to a motor exhibiting a unity torque $T_B = 1$ p.u. at a unity electric speed $\omega = \omega_B = 1$ p.u., and fed by a unity voltage $V = V_B = 1$ p.u.

ii. The motor has to satisfy the flux–weakening operating point. This corresponds to satisfy a prefixed torque–to–speed characteristic. In the case under study, a constant power is required up to a flux–weakening speed $\omega = \omega_{FW} = 3$ p.u.

iii. Finally, the motor has to exhibit a prefixed maximum braking torque T^*_{brk}. In the case under study, a p.u. value of $T^*_{brk} = 0.1$ p.u. is fixed.

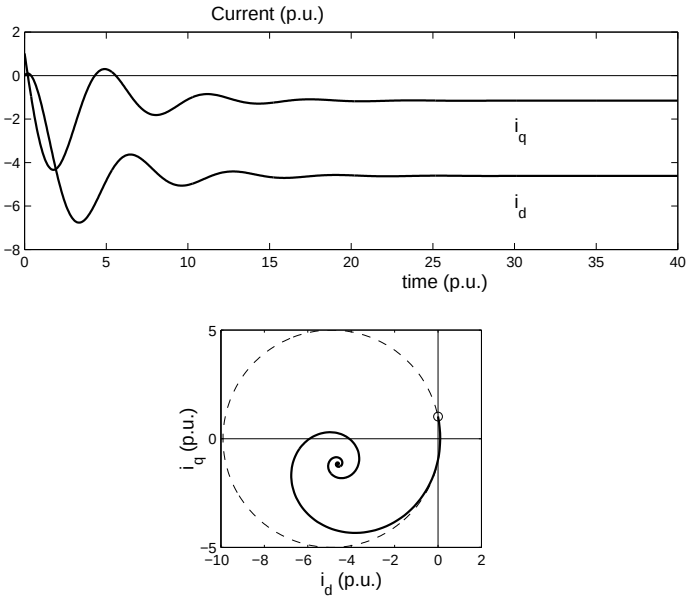

Figure 4.5: Short–circuit current behaviors of SPM motor #1

Thus, the design of the IPM motor has to be bound to the constraints above. The saliency ratio ξ is supposed to be given, according to the adopted configuration of the rotor (e.g. with one, two, or more flux–barrier per pole). In the following procedure, the adopted criterion is to minimize the nominal current of motor and inverter.

4.4.1 Parameters to limit the braking torque

The third item deals with the maximum braking torque of the motor during a three–phase short–circuit, that has to be kept lower than a fixed value (e.g. 0.1 p.u.). The maximum braking torque can be computed for the various combinations of the IPM motor parameters, using (4.13) with $f(\xi)$ computed for $\xi = 6$. The constraint of its maximum value implies a further reduction of the feasible combinations.

Referring to the example reported in Fig. 2.2, T^*_{brk} is drawn versus Λ_m. It increases rapidly with Λ_m, thus only a portion is drawn. The solution with $\Lambda_m = 0.434$ p.u. that satisfies the first two items yields a braking torque higher than $T^*_{brk} = 0.95$ p.u., that can not be accepted. The constrain $T^*_{brk} \leq 0.1$ p.u. is highlighted in Fig. 2.2: it limits PM flux linkage Λ_m to be lower than 0.136 p.u., with a corresponding nominal current $I_N \geq 1.51$ p.u..

The cost of reducing the maximum braking torque under a fixed value depends on different factors, among which the saliency ratio and the flux–weakening requirements. In the example above, such a cost can be considered as the increase of the volt–ampere

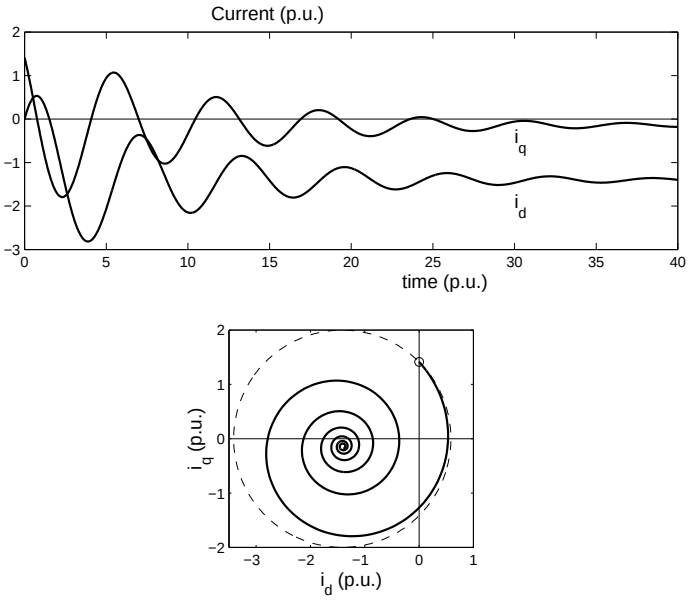

Figure 4.6: Short–circuit current behaviors of SPM motor #2

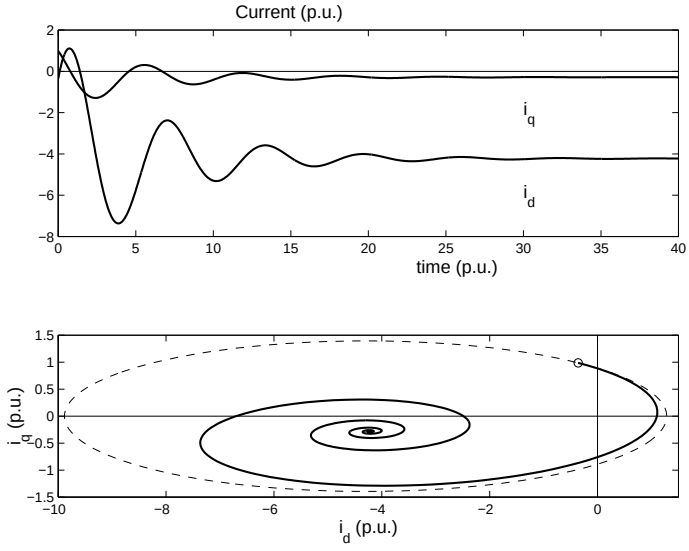

Figure 4.7: Short–circuit current behaviors of IPM motor #1

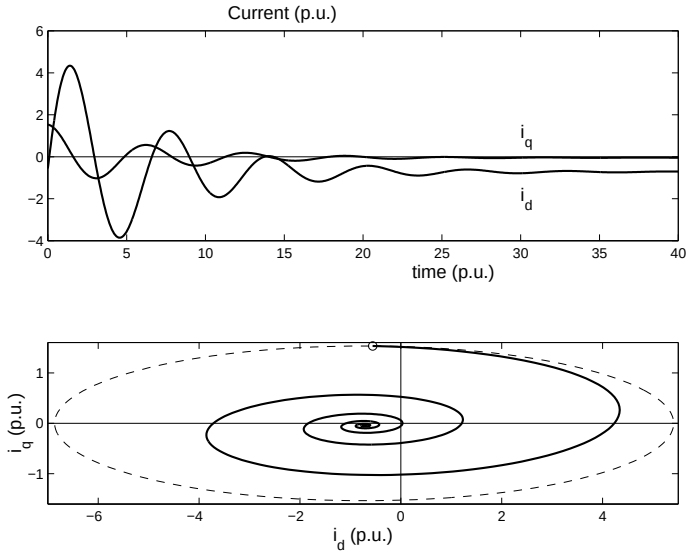

Figure 4.8: Short–circuit current behaviors of IPM motor #2

rating of the motor drive of about 25% (computed as 1.51/1.213).

Similar computation can be carried out fixing a different saliency ratio, for instance if $\xi = 4$ is fixed, it results $\Lambda_m = 0.18$ p.u. and $I_N = 1.56$ p.u.

4.4.2 Parameters for given maximum short–circuit current

If the value of the steady–state short–circuit current is fixed, it is possible to identify analytically the IPM motor parameters. Let k_{shc} be the ratio between the short–circuit current I_{shc} and the nominal current I_N, that is, $I_{shc} = k_{shc} I_N$, fixed to a given value. Assuming the resistance to be zero, it results $I_{shc} = \Lambda_m / L_d$, so that the

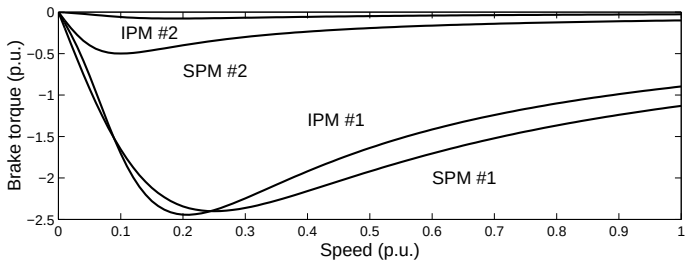

Figure 4.9: The p.u. brake torque as a function of the p.u. motor speed

PM flux linkage becomes $\Lambda_m = k_{shc} L_d I_N$.

The torque and voltage relationships can be arranged as

$$\begin{aligned} T = & \frac{3}{2} p \left[\frac{k_{shc}}{\xi} \sin \alpha_i^e + \left(\frac{1}{\xi} - 1 \right) \frac{\sin 2\alpha_i^e}{2} \right] L_q I_N^2 \\ = & \; c_\tau L_q I_N^2 \end{aligned} \tag{4.17}$$

and

$$\begin{aligned} \left(\frac{V}{\omega} \right)^2 = & \left[\left(\frac{k_{shc}}{\xi} + \frac{\cos \alpha_i^e}{\xi} \right)^2 + (\sin \alpha_i^e)^2 \right] (L_q I_N)^2 \\ = & \; c_\lambda^2 \left(L_q I_N \right)^2 \end{aligned} \tag{4.18}$$

where α_i^e is the vector current angle, determined by imposing the maximum torque–to–current ratio [1]. Finally, the saliency ratio ξ is supposed to be known according to the adopted rotor configuration. Since at base operating point $T = T_B = 1$ p.u., $V = V_B = 1$ p.u., and $\omega = \omega_B = 1$ p.u., then (4.17) and (4.18) define a system of two equations where the two unknowns L_q and I_N can be determined as

$$L_q = \frac{c_\tau}{c_\lambda^2} \qquad I_N = \frac{c_\lambda}{c_\tau} \tag{4.19}$$

As an example, Fig. 4.10 shows the reduction of the PM flux linkage Λ_m as a function of ξ for different values of the ratio k_{shc}. As expected, Λ_m increases when k_{shc} increases (a higher short–circuit current is tolerated). Besides, it can be observed that the higher the saliency ratio, the lower the PM flux linkage. This implies that the reluctance torque becomes predominant with respect to the PM torque, with a slight increase of the nominal current (without considering the saturation).

4.5 IPM design

4.5.1 Performance requirement to each motor

Let us refer to the steer–by–wire system shown in Fig. 4.11 to transform the rotary movement into linear movement a ball–screw is adopted The ball–screw gear ratio has been selected to be 5 mm per revolution. Its mechanical efficiency is about 80%. From the mechanical requirements, the maximum speed of the motor results equal to 3000 rpm (i.e. 314.2 rad/s).

In order to guarantee the peak force, the maximum torque required to the couple of motors is 10 Nm (including the ball–screw efficiency). Therefore, the maximum torque of each motor is 5 Nm, with a duty cycle of 8.5%.

The maximum angular acceleration is about 10000 rad/s^2 (corresponding to the acceleration of 8 m/s^2). This value is a reasonable value for PM machines [16].

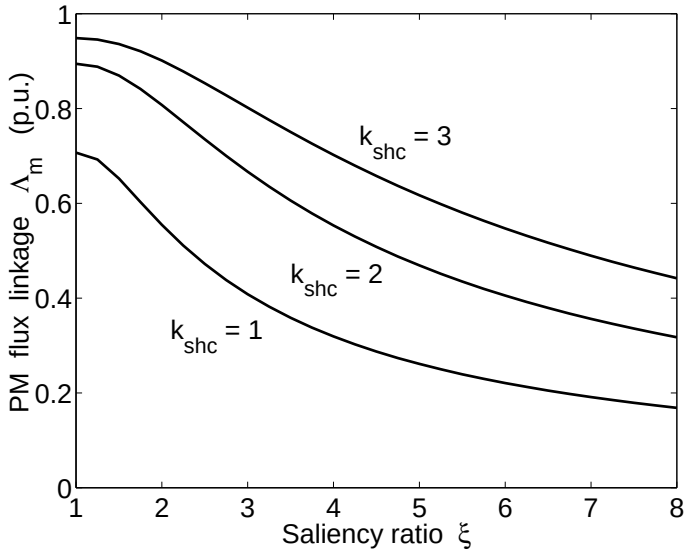

Figure 4.10: Λ_m (in p.u.) vs. ξ for different k_{shc} with $T = T_B = 1$ p.u., $V = V_B = 1$ p.u., and $\omega = \omega_B = 1$ p.u.

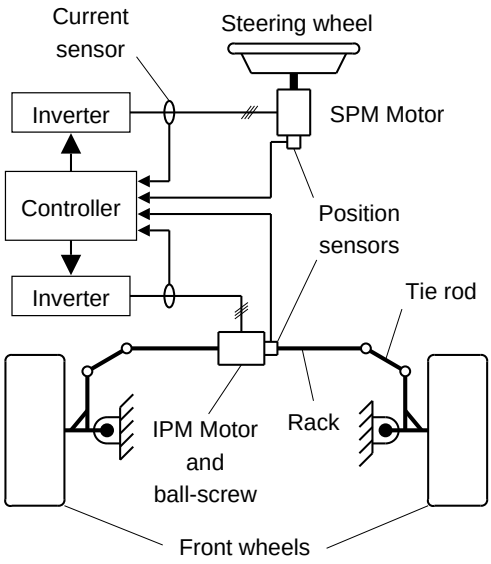

Figure 4.11: Scheme of the steer-by-wire system

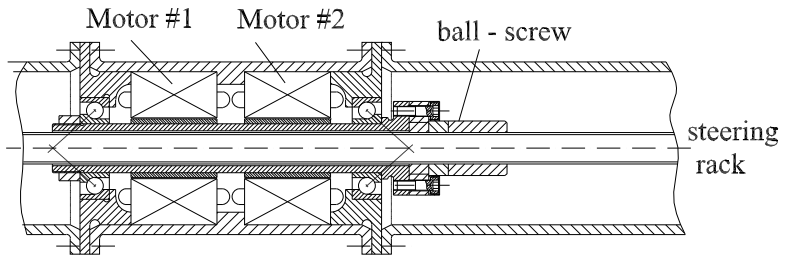

Figure 4.12: Electric power steering rack highlighting the two motors and the ballscrew system

In order to guarantee the other operating conditions, each motor has to be satisfy 3.8 Nm at a speed 480 rpm (duty–cycle 60%), and 1.5 Nm at a speed 2400 rpm (duty–cycle 25%).

4.5.2 Geometrical constraints

A commercial lamination has been selected for the stator. The external diameter was imposed to be $D_e = 120$ mm by the application. The corresponding inner diameter is $D = 70$ mm for a 4–pole motor. For this size, commercial laminations are found with a number of slots $Q = 24$. As far as the harmonics contents due of the air–gap M.M.F. distribution is concerned, a different number of slots should be preferred, e.g. $Q = 36$.

The air–gap thickness was fixed equal to $g = 0.5$ mm, and the stack length equals $L_{stk} = 40$ mm. As will be described hereafter, the total length was obtained by means of two modules, of 20 mm each, skewed of an appropriate angle.

In order to facilitate the experimental tests in the laboratory, the motor was designed for a voltage higher than 42 V, that is becoming a standard in automotive applications. The motor winding was designed for a D.C. bus of 300 V.

Due to the high temperature that can occur in the considered application, so that the temperature rise is low, the current density has to be adequately reduced.

4.5.3 Design considerations

From the required specifications, it is found that the mechanical characteristic of the IPM motor has a constant–torque region, followed by a constant–power region. Therefore the IPM motor has to exhibit a flux–weakening capability. Fixing the base speed equal to 900 rpm, the flux–weakening speed–range is 3.33.

The consideration above, together with that of a low braking torque in case of fault, yield an IPM motor characterized by a limited amount of PM. As a consequence, the IPM motor has to be characterized by a high saliency. The solution adopted is an

IPM rotor with three flux–barriers per pole. With such a rotor configuration, the estimated saliency ratio approaches $\xi = 6$.

As regards the maximum braking torque, a value $T^*_{brk} = 0.33$ Nm has been fixed. The number of poles is $2p = 4$, the saliency ratio $\xi = 6$, and then $f(\xi) \approx 5$. Since the air–gap volume is fixed ($D = 70$ mm, $L_{stk} = 40$ mm, and $g = 0.5$ mm), the maximum air–gap flux–density (the peak value of the ideally sinusoidally distributed waveform) results $\hat{B}_{g0} = 0.1$ T.

4.5.4 Finite element simulations

A finite element analysis is used to refine the IPM motor design. The IPM motor configuration that has been chosen is reported in Fig. 4.14 and Fig. 4.13, that reports the flux plot and the computed flux linkages of the motor.

The computed unsaturated q–axis inductance results $L_{qu} = 0.317$ H, while the d–axis inductance is $L_d = 0.055$ H. Thus the unsaturated saliency ratio results almost $\xi = 5.7$.

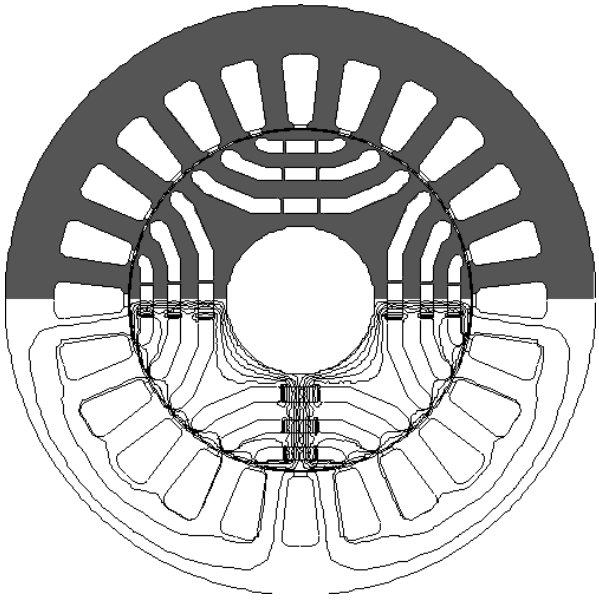

Figure 4.13: Finite element analysis of the IPM motor: Structure and flux plot at no–load

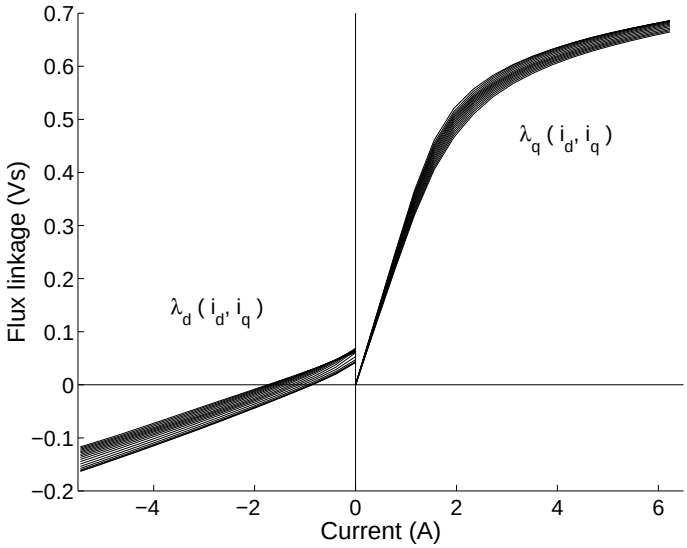

Figure 4.14: Finite element analysis of the IPM motor: $d-q$ axis flux linkages vs. currents

4.5.5 Torque ripple minimization

The finite element analysis helped in the research of that IPM motor configuration suitable to reduce the torque ripple.

At first the rotor length $L_{stk} = 40$ mm was split in two modules of 20 mm. These two modules have been connected to the shaft with a skewing angle to reduce the torque harmonic of 24–th order. This is shown in Fig. 4.15, showing that the torque harmonic of 12–th order remains almost the same, that of 24–th order is almost cancelled, while these of upper order are reduced.

Finally, thanks to the special applications, requiring two motors on the same shaft, it is possible to skewed one motor with respect to the other, so that the torque harmonics are 180 degrees out of phase. This is accomplished to the aim to cancel the torque harmonic of 12–th order. The final effect is shown in the third part of Fig. 4.15, that refers to the average torque of the combination of the two motors.

Referring to a rated torque of 2.6 Nm, the estimated torque ripple is slightly higher than 2%.

4.5.6 Measurements on the prototype

At first, the PM flux linkage has been measured at no–load. The IPM motor was rotated at a speed of 1000 rpm, and the back E.M.F. has been measured. By integrating the back E.M.F. the flux linkages due to the PM are obtained. Fig. 4.16 shows the

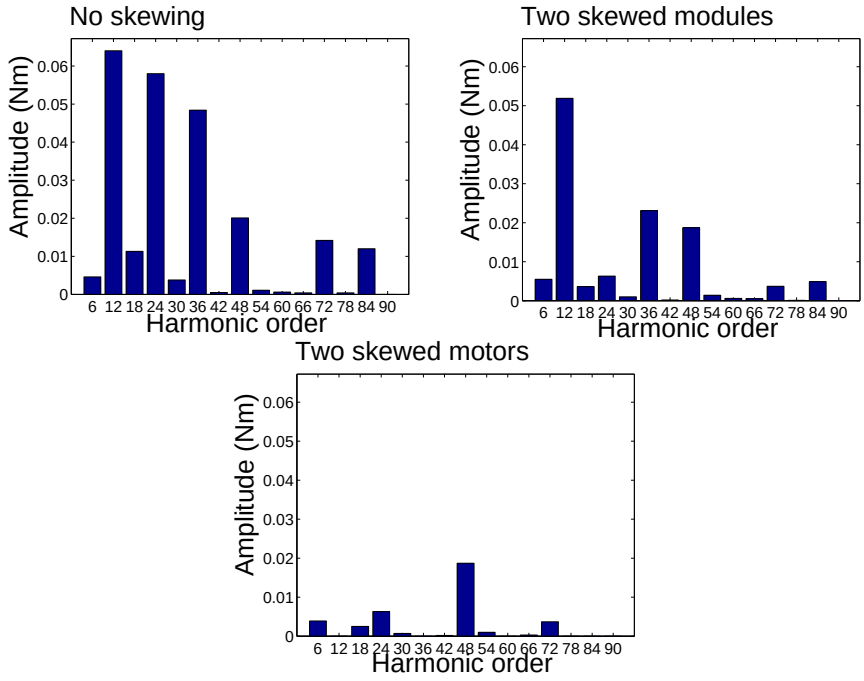

Figure 4.15: Torque harmonics in different motor solutions

measured flux linkages due to the PM.

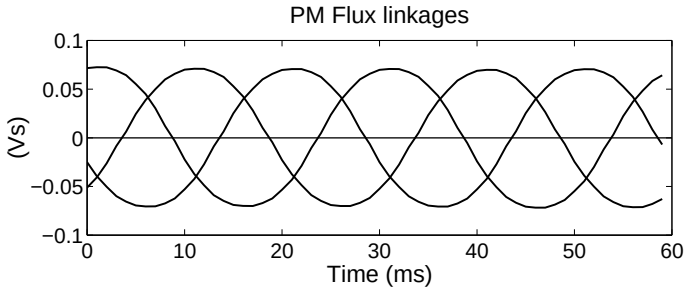

Figure 4.16: Measured flux linkages due to the PM

The electromechanical torque has been tested at different d– and q–axis currents. The dots in Fig. 4.17 refer to the measured torque in the d– q–axis current plane. In the same Fig. 4.17 the solid line refer to the torque values resulting from the finite element simulation. The comparison shows a good agreement between measurements and simulations.

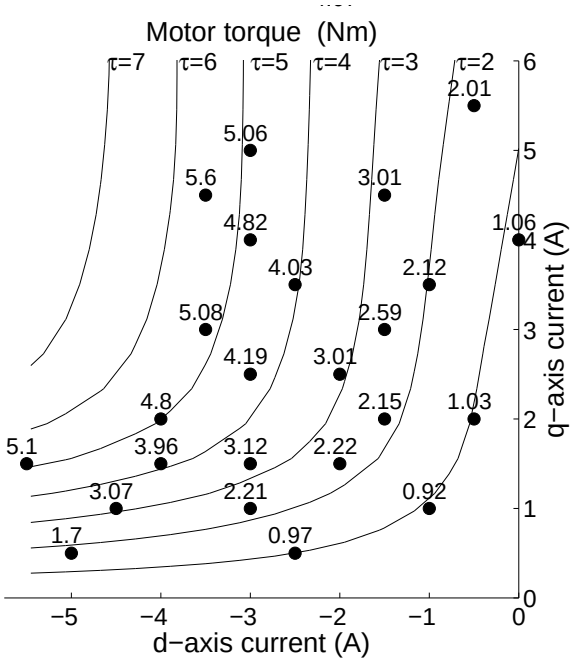

Figure 4.17: Measured torque of the IPM motor: solid lines are simulated value, while dots are measured values

In order to measure the short–circuit current and the corresponding braking torque, the three terminals were short–circuited, and the IPM motor was rotated at different speeds. The three–phase current waveforms are almost sinusoidal, as shown in Fig. 4.18 according to a motor speed of 1000 rpm.

The short–circuit current and the corresponding braking torque at different motor speed are reported in Fig. 4.19. With $R = 7.3\ \Omega$ (according to a temperature rise of 60C), a saliency ratio $\xi = 5.7$, and a PM flux linkage $\Lambda_m = 75$ mVs, the maximum braking torque is found from 4.13 to be $T^*_{brk} = 0.25$ Nm at the mechanical speed $\omega^* = 43.5$ rad/s. The measurements reported in Fig. 4.19 confirm this analytical result.

4.6 Conclusion

This chapter has presented the whole electrical drive system for a steerbywire application, in particular the design hints of the electric motors. The electrical motors have been designed to exhibit an inherent faulttolerant capability, in order to enhance driver safety. For critical application, a redundant solution with two motors placed on the same shaft is imperative. However this is not enough when PM motors are

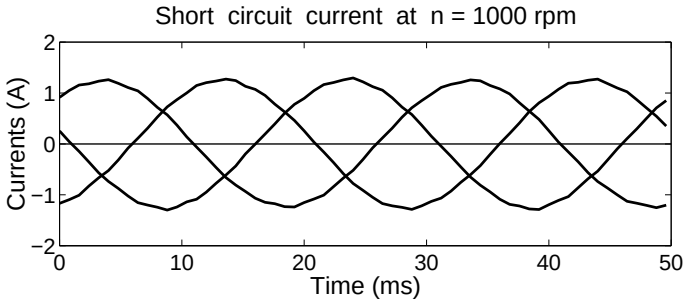

Figure 4.18: Measured short–circuit currents

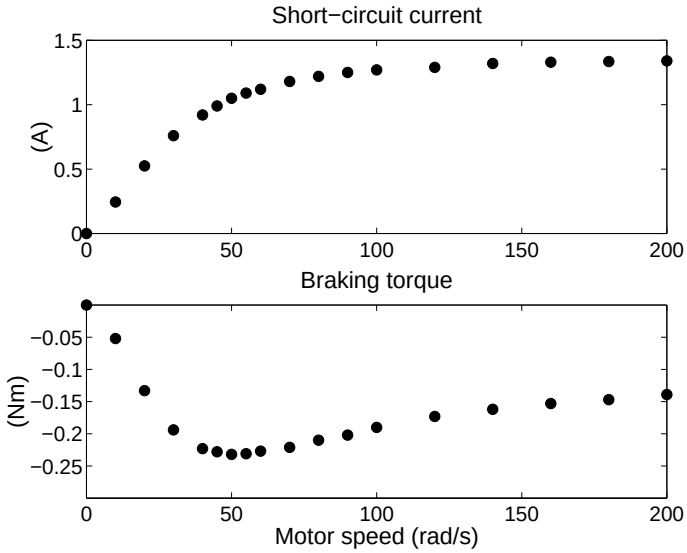

Figure 4.19: Measured short–circuit current (peak value) and braking torque at different motor speed

used, due to the presence of PMs on the rotor that induce an e.m.f. on the winding. Thus, in case of fault, a short-circuit current is forced in the stator winding. The analysis of the three-phase short-circuit fault, considered the worst case, is carried out. From the computation of the maximum brake torque it is possible to achieve a suitable relationship to determine the more appropriate parameters of the motor. In particular, reduced braking torque and torque ripple have been accomplished. The design was oriented to the application to a commercial car, already mass-produced with the conventional power assisted steering. All of the technical specifications and

parameters used in the design and test of the proposed system have derived from a tight collaboration with the car manufacturer, which will also look after the details of the final transposition on the vehicle.

Part II

Electrical Redundancy

Chapter 5

Motor Design for Electric Redundancy

This chapter describes experimental results from a permanent magnet machine, which has been designed with fault tolerance in mind. The main thrust of this contribution is concerned with demonstrating that the fault-tolerant electromagnetic performance can be achieved. The machine must be designed so that even with a winding or switching device short circuit, the fault currents are limited to a level within steady state thermal limits. Penalties must be considered in terms of machine volume and power switching device rating, although it is shown that these penalties are not severe.

5.1 Requirements of a fault-tolerant drive

There are many potential faults which can occur in a drive system: inevitably within this work the range of faults under consideration must be restricted. For example, a design which is insensitive to the failure of a position transducer would probably require sensorless operation, which is beyond the scope of this thesis. The principal electromagnetic faults which may occur within the machine are:

- winding open circuit
- winding short circuit (phase-ground or within a phase)
- winding short circuit at the terminals.

Within the power converter the faults under consideration are:

- power device open circuit
- power device short circuit

- DC link capacitor failure

The aim is to develop a drive which can continue to operate with any one of these faults. The first solution is a complete redundant system of two motors and two inverters as shown in Fig.5.1. This solution increase the fault tolerance of the system but in case of fault the output rating torque is half of the torque in healthy mode.

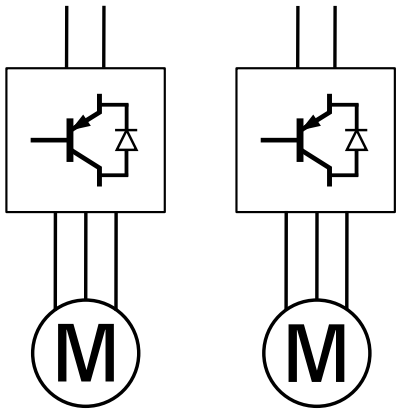

Figure 5.1: double motor and double inverter

It has become clear that the most successful design approach involves a multiple phase drive in which each phase may be regarded as a single module. The operation of any one module must have minimal impact upon the others, so that in the event of that module failing the others can continue to operate unaffected.

Fig.5.2 shows the first solution with modular approach where the converters are commercial three–phase inverter. On the contrary, the motor shows a special winding with complete electrical, magnetic and thermal isolation between phases. More details will be shown in chapter 7.

An alternative solution is to adopt a multi–phase motor drive. A five–phase drive is shown in Fig.5.3. The performance of this system is greater than the previous solution but it demands a special lamination (see chapter 6) and a five–phase inverter with five separate modules as will be described in section 5.2.

The modular approach requires that there should be minimal electrical, magnetic and thermal interaction between phases of the drive. This philosophy must extend to both the machine and the power converter.

5.1.1 Fault tolerance in permanent magnet machine drive

The requirements outlined in the previous Section naturally fix certain features of the machine design and drive configuration. These requirements will be considered for a voltage fed inverter drive.

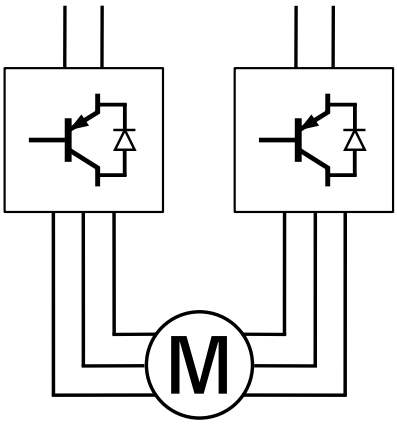

Figure 5.2: single motor and double inverter

Complete electrical isolation between phases

This can be shown to be an essential requirement if continued operation is to occur with either a power device or winding short-circuited. For instance, in a star connected system the star point may rise to the DC link voltage, so that no net torque capability remains. The clear alternative is to drive each phase from a separate single-phase bridge. This doubles the number of power devices but only marginally increases the total power electronic device volt-ampere rating, because each device need only withstand the phase voltage rather than the line voltage of star connected systems.

Implicit limiting of fault currents

The most difficult machine fault to accommodate is a winding short-circuit. A power electronic device short-circuit failure produces a similar condition to a winding terminal short circuit, except that the fault current flows through the converter as well as the winding. Thus, a phase terminal short-circuit has received particular attention. The system was designed without any fuses incorporated into the drive, as the reliability of fuses is generally poor. This leaves two possibilities for dealing with the above fault conditions.

- The machine can be deliberately designed with a low per unit inductance, so that a large fault current flows. Thus, a winding short–circuit fault will result in a very large winding short-circuit fault current, the faulted winding will overheat and subsequently produce an open-circuit. Equally a device short circuit will produce a very large faulted device current, and the subsequent heating will eventually produce an open-circuit condition.

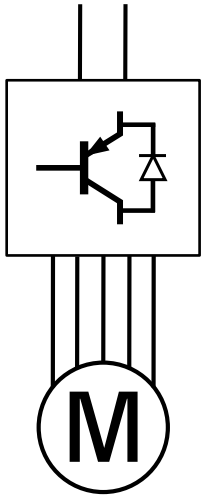

Figure 5.3: Five–phase drive

- Alternatively, the machine can be designed with a per unit inductance approaching 1.0 per unit, so that a phase terminal short circuit will not result in steady state motor currents beyond 1.0 per unit. The thermal limit of the faulted winding will not be exceeded and the short circuit can be accommodated over an extended period.
  Torque ripple resulting from the short-circuit current in the faulted phase will inevitably be large unless special measures are employed. The second of the above approaches provides a more reliable, fault-tolerant solution, as the first option allows very large per unit fault currents to flow in failed power electronic devices until they turn open circuit. The faulted device will experience large thermal stresses, which may lead to disintegration of the packaging and propagation of the fault into surrounding power devices.
  Producing an effective d axis inductance of one per unit is generally considered difficult to achieve in a small permanent magnet machine, but it is shown in a later section that this can in fact be achieved relatively easily.

Magnetic isolation between phases

Without magnetic isolation, fault currents in one phase induce large voltages in other phases, preventing adequate control of them. Furthermore, the current flowing in unfaulted phases supplements the magnet MMF and so increases the EMF driving fault current.

Thus it becomes clear that for a given unfaulted armature reaction field the single phase short-circuit fault current is substantially greater when there is mutual coupling

between phases. A torque controller has been developed to minimize the machine output torque ripple when operating in the faulted condition. The controller identifies current profiles which produce a given torque demand for minimum Joule loss under both normal and faulted conditions, thus giving closed loop torque control. This torque control was found to be severely impaired by substantial phase-phase mutual coupling.

The above results show that both the faulted and unfaulted phases perform substantially worse when there is mutual coupling between phases, so the machine should be designed with minimal phase-phase mutual coupling. In surface mounted magnet designs the airgap flux due to armature reaction is small and a substantial amount of the phase inductance arises due to cross-slot leakage flux. If this is to remain solely a self inductance component then each slot should contain the conductors of one phase only. The component of armature reaction flux which crosses the airgap will always contain an element which links the other phases.

However, if a surface mounted magnet design with a nonmagnetic retaining sleeve is employed, then the presence of the sleeve, combined with relatively deep magnets, greatly reduces the airgap component of the armature reaction field, so that in effect the mutual coupling is often insignificant.

Effective thermal isolation between phases

If the stator outer surface is well cooled then the dominant temperature rise in the machine is within each slot. By ensuring that each slot contains only a single phase winding then thermal interaction between phases is minimized.

Physical isolation between phases

A phase-phase fault is especially serious, since it will disable two phases. By placing each winding round a single tooth then all phase windings (including the end windings) are physically separated, thus virtually eliminating the possibility of a phase to phase fault.

Number of phases

The basic criteria used is that the drive should continue to produce rated power in the event of the failure of one phase. Hence, if there are n phases, each phase must be overrated by a fault-tolerant rating factor, F, where F = n/(n - 1). Thus, if there are three phases, each drive must be overrated by 50% in order to give full capability when faulted. Clearly, F falls as the number of phases rises, but this must be balanced against the increasing complexity of a high phase number and the inevitably greater chance of a failure.

Summary

With regard to the machine design, the essential conclusions are that the machine should have (i) a surface mounted magnet rotor design, (ii) a one per-unit armature self inductance, (iii) each winding wound around a single tooth and (iv) only one phase winding per slot. The first two conclusions appear to be in conflict because a surface mounted magnet machine generally has a low per unit reactance. However, the key to achieving these requirements is to design a machine with a large leakage inductance by controlling the depth and width of the slot opening, commonly called the stator reactance slot. In the event of a phase winding short circuit then one half of the magnet flux which normally passes up one tooth must be shunted across each reactance slot. To avoid undue saturation the reactance slot depth is designed to be approximately one half of the tooth width, with the reactance slot width chosen according to the required inductance.

5.2 The full–bridge vs. half–bridge inverter for five–phase PM motor

For the sake of limiting the electrical interaction, the phases have to be supplied separately. To this aim, both the terminals of each phase are brought out to the motor and each phase is supplied by a full–bridge inverter as shown in Fig. 5.4. The advantage of this solution is the high partitioning among the phases: the motor drive can operate even with a short–circuited phase, since it is no longer supplied by the corresponding bridge of the inverter [17]. As far as the cost of the half– and full–bridge inverters solutions is concerned, it is convenient to refer to the same output motor power P_{out}, so that the motor cost remains the same. In the first solution the rms phase voltage is

$$E' = \frac{V_{dc}}{2\sqrt{2}\sin\left(\frac{2\pi}{5}\right)} \tag{5.1}$$

while in the second solution it is

$$E'' = \frac{V_{dc}}{\sqrt{2}} \tag{5.2}$$

As a consequence, according to a lossless system and unity power factor, the rms current results:

$$I' = \frac{2\sqrt{2}\sin\left(2\pi/5\right)P_{out}}{5V_{dc}} \tag{5.3}$$

$$I'' = \frac{2\sqrt{2}P_{out}}{5V_{dc}} \tag{5.4}$$

It results that the Volt–Amps rating (given by the product of rated current by *dc* voltage and by the switch numbers) of the full–bridge inverter is about 105% the Volt–Amps rating of the half–bridge inverter.

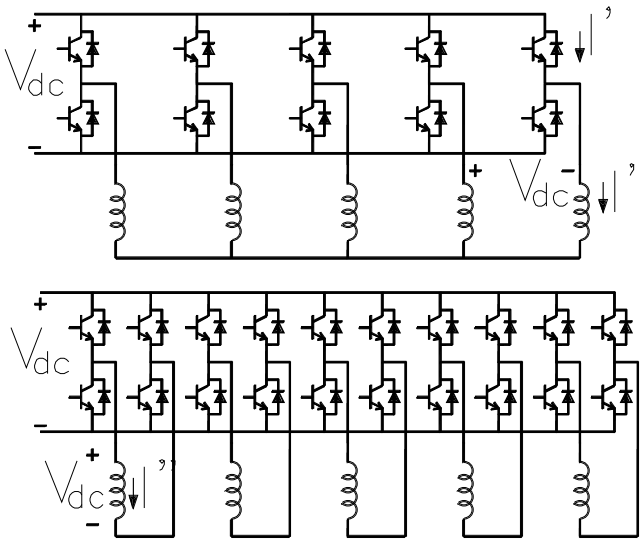

Figure 5.4: 5–phase inverter: half–bridge and full–bridge

5.3 Multi-phase inverter

A multi–phase inverter has been built in Laboratory. For each phase a full–bridge converter is used, so as to achieve a complete electrical insulation between phases. In order to avoid the design of the control regulators of the test bench, a hysteresis current control has been implemented.

The basic principle of current control is based on the classical hysteresis control. The voltage applied to each phase (see Fig.5.5) is +Vdc/2 (switching on the switches, $S1$ and $S4$), - Vdc/2 (switching on the switches $S3$ and $S2$) and 0 volts (switching on the switches $S1$ and $S2$ or $S3$ and $S4$).

The commutation frequency depends on phase voltages v and e, the current band ΔI and inductance L. The motor equation is:

$$u = Ri + L\frac{di}{dt} + e \tag{5.5}$$

Defining i^* as the current reference and u^* the voltage reference, the equation becomes

$$u^* = Ri^* + L\frac{di^*}{dt} + e \tag{5.6}$$

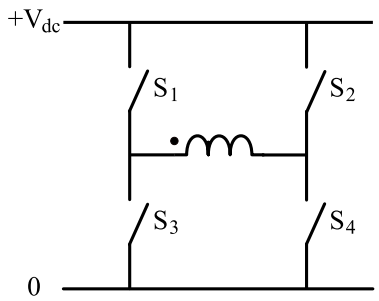

Figure 5.5: Full–bridge inverter

Subtracting (5.6) to (5.5) it is

$$R\delta + L\frac{d\delta}{dt} = u - u^* \tag{5.7}$$

where δ_i is error signal as shown in Fig.5.6.

$$\delta = i - i^* \tag{5.8}$$

Neglecting the resistance, (5.7) becomes

$$L\frac{\Delta\delta}{\tau_p} = u - u^* \tag{5.9}$$

The inverter supplies a phase voltage equal to $\pm V_{dc}$, therefore the rise time and the descend time can be expressed as

$$\tau_p = \frac{4L\Delta I}{Vdc - u^*} \qquad \tau_n = \frac{4L\Delta I}{Vdc - u^*} \tag{5.10}$$

The period is the sum of the rise time and the descend time, therefore the frequency is

$$f = \frac{1}{T} = \frac{V_{dc}\left(1 - \frac{{u^*}^2}{V_{dc}}\right)}{8L\Delta I} \tag{5.11}$$

The frequency is a function of the band amplitude ΔI and of the inductance L.

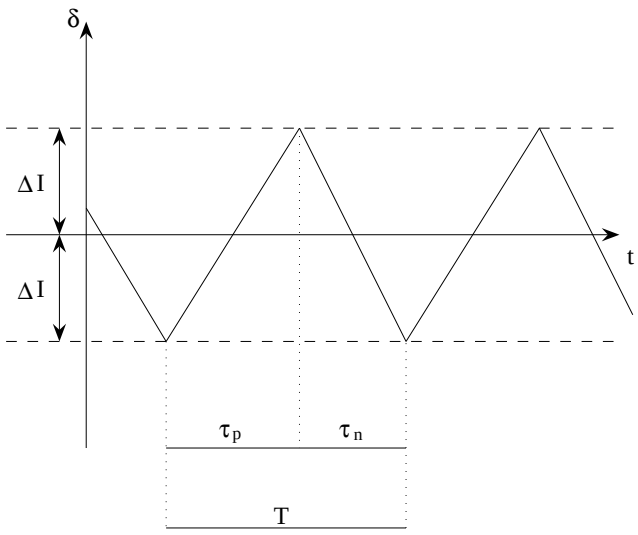

Figure 5.6: Current error

Chapter 6

Five–Phase PM Motor

This chapter deals with the analysis of five–phase fractional–slot PM motors with non–overlapped coils, suitable for fault–tolerant applications.

In order to verify the fault–tolerant capability of the motor, some post–fault operations are analyzed. Proper current control strategies can be adopted, so as to guarantee safe drive operation after fault occurrence. As an example two faults are considered: one open–circuited phase and one short–circuited phase. Two motors with two different windings are compared, under each fault type.

6.1 Five–phase PM machines

The five–phase PM motor has been proposed recently for its inherently high fault–tolerant capability [18,19]: to reduce the fault occurrence, as well as to operate indefinitely in the presence of fault [3]. In fact, many applications require a fault–tolerant capability to electrical motor drives, for instance automotive [20] and aeronautic applications [21].

The electric power in a five–phase motor is divided into more inverter legs, reducing the current of each switch [17, 22]. In addition, with five independent phases, in the event of failure of one or more phases, the remaining healthy phases let the motor to operate properly [23].

Proper current control strategies have been proposed for the post–fault operations [24], sometimes accepting a few additional (redundant) components. These control strategies can be successfully adjusted to face the post–fault situation, with a minimum impact of the fault on torque ripple, noise [25–27] and losses [28].

Two five–phase PM motor prototypes are considered. An example of a five–phase PM motor with 10 slots and 8 poles is shown in Fig. 6.1. They are characterized by a double– and a single–layer winding, respectively.

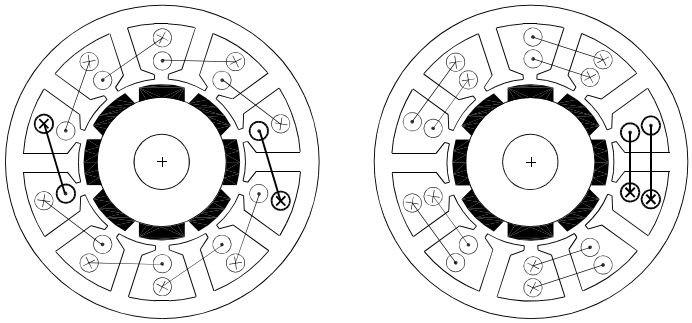

Figure 6.1: Five–phase 10–slot 8–pole PM motors with double– and single–layer winding.

6.2 Five–phase motor prototypes

The experimental results described hereafter in this chapter refer to two five–phase 20–slot 18–pole motor prototypes.

Fig. 6.2 and Fig. 6.3 show a double– and single–layer fractional–slot winding with unity coil throw and their star of slots, respectively.

In the single–layer winding each slot contains only coil sides of the same phase. This winding type reduces the physical contact between phases [4, 16, 29].

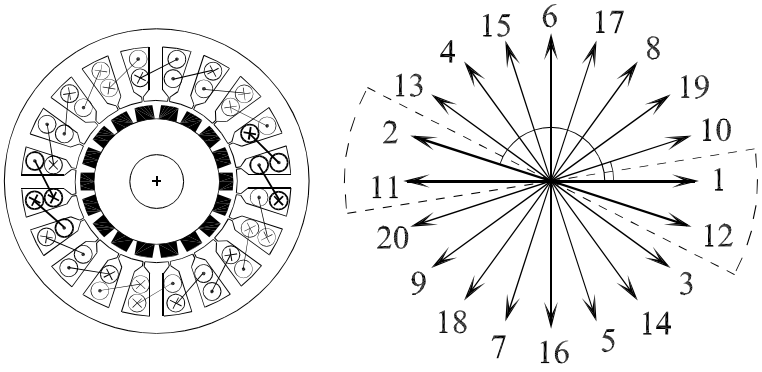

Figure 6.2: 5–phase 20–slot 18–pole PM motor: star of slots with double–layer winding.

A special stator lamination has been used, to get a number of slots Q multiple of 5. The external diameter is 120 mm and the stack length is 50 mm. The first stator is characterized by a double–layer fractional–slot winding with unity coil throw shown

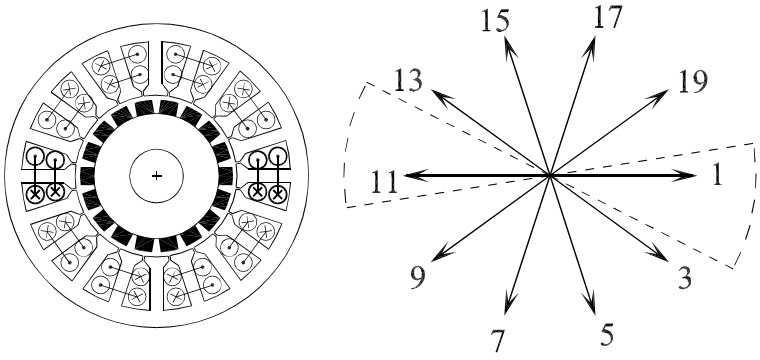

Figure 6.3: 5–phase 20–slot 18–pole PM motor: star of slots with single–layer winding.

on the left hand side of Fig. 6.4. The second stator is characterized by a single–layer winding, as shown in the right hand side of Fig. 6.4. The two windings have been designed as described in [2].

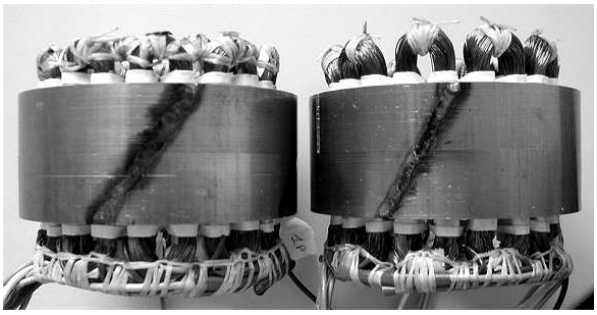

Figure 6.4: A 5–phase 20–slot stator with double–layer and single–layer winding

The machine with 20 slots and 18 poles yields a machine periodicity t=1. Therefore, both Q/t and $Q/(2t)$ are even. Both motors exhibit only odd–order harmonics in the air–gap MMF distribution. However, the single–layer winding is characterized by a high MMF sub–harmonic, as also shown in Fig. 6.5.

Due to the low machine periodicity (t=1), the sub–harmonic of order ν=1 exists, as shown in Fig. 6.5. Then, only harmonics of odd order exist. When the double–layer winding is transformed into a single–layer one, the harmonics remain of the same order, but their amplitude increases. The winding factor of the main harmonic (i.e. of order ν=p=9) slightly increases.

In both 20–slot 18–pole motors, the mutual coupling between phases is almost zero. It is easily recognizable from the distribution of the magnetic scalar potential,

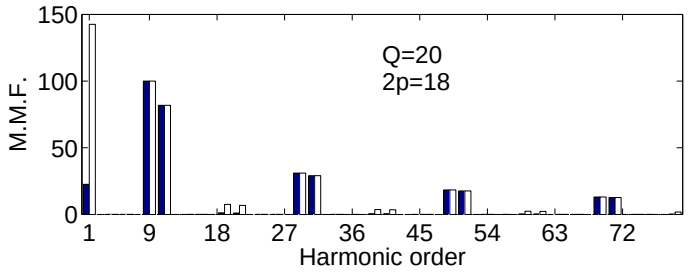

Figure 6.5: 5–phase 20–slot stator MMF harmonic contents (black bars refers to the double–layer winding, white bars refers to the single–layer winding)

as in Fig. 6.6.

The PM flux–linkage Λ_m, the self inductance L_a, and mutual inductances M_{ba} and M_{ca} between adjacent and non–adjacent phases respectively, are reported in Table 6.1. The phase resistance is $R = 24.6\ \Omega$ at 25^oC ($R = 32\ \Omega$ at 100^oC). Nominal current is $\hat{I}_1$=0.85 A (peak value) and the nominal torque T_n is slightly lower than 6 Nm, for both motors.

When a single phase is supplied by sinusoidal current, in phase with the corresponding back EMF, the torque has an average value and other oscillating terms. The amplitudes of the first three harmonic terms are used to determine the suitable current waveforms in post–fault operations. They are the average torque T_1, the second order term T_3 and the fourth order term T_5. Their value is reported in the second part of Table 6.1.

Table 6.1: Flux–linkage, self and mutual inductances, and coefficients T_ν of the two motors under test

motor type		double–layer	single–layer
Λ_m	(Vs)	0.288	0.292
L_a	(mH)	31.19	47.00
M_{ba}	(mH)	0.002	0.005
M_{ca}	(mH)	0.011	0.032
T_1	(Nm)	2.346	2.373
T_3	(Nm)	-0.330	-0.364
T_5	(Nm)	0.041	0.052

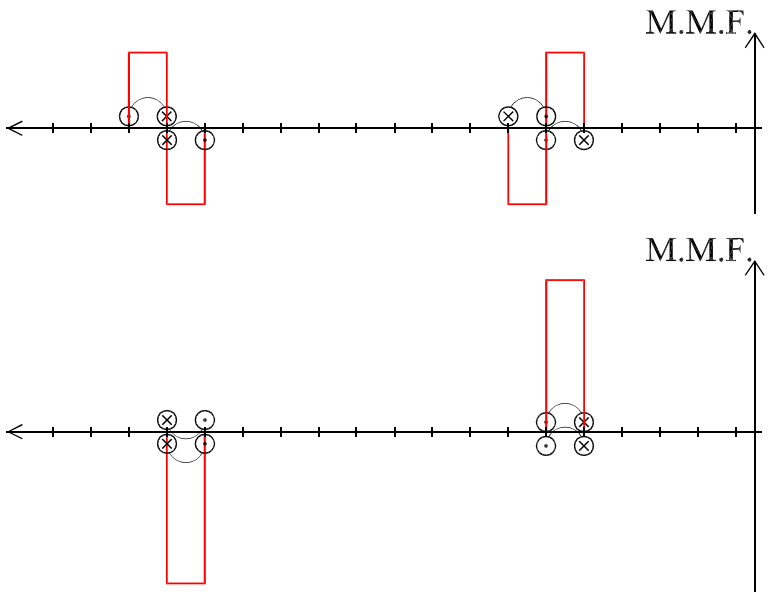

Figure 6.6: Magnetic scalar potential of the 5–phase 20–slot 18–pole PM motor with double– and single–layer winding.

6.3 Motor model

Because of the zero mutual inductance between phases, the motor model results particularly simple. Let us assume also that mutual coupling between phases is zero even in presence of iron saturation and the motor losses are negligible. This lets the torque contribution of each phase be considered individually, and then summed to that of the other phases, as in [29].

The air–gap flux–density distribution due to the PMs can be expressed by means of the Fourier series expansion. Let us suppose that the rotor position is $\vartheta_m^e = 0$ at the time instant $t = 0$, so that $\vartheta_m^e = \omega t$. Then

$$B(\vartheta_s^e, t) = \sum_{\xi} \hat{B}_{\xi} \cos \xi(\vartheta_s^e - \omega t) \tag{6.1}$$

where θ_s^e is the angular coordinate in the stator reference frame in electrical radians. Similarly, the conductor density distribution of the mth phase can be described as

$$n_m(\vartheta_s^e) = \sum_{\nu} \hat{n}_{d\nu} \sin \nu \left(\vartheta_s^e - k_m \frac{2\pi}{5} \right) \tag{6.2}$$

where $\hat{n}_{d\nu} = 2k_{w\nu}N_s/(\pi D)$ is the peak of the νth order harmonic of the conductor density distribution, the subscript $m = a, b, c, d, e$ and $k_a = 0$, $k_b = 1$, $k_c = 2$, $k_d = 3$, $k_e = 4$. The mth phase current can be expressed as

$$i_m(t) = \hat{I}_n \tilde{i}_m(t) \tag{6.3}$$

where $\hat{I}_n$ is the nominal current peak and $\tilde{i}_m(t)$ is a dimensionless function that describes the current behavior vs. time (that is vs. rotor position, since $\vartheta^e_m = \omega t$). Then, the mth phase electrical loading, given by $n_m(\vartheta^e_s)i_m(t)$, becomes

$$K_m(\vartheta^e_s, t) = \sum_\nu \hat{K}_\nu \sin\nu \left(\vartheta^e_s - k_m \frac{2\pi}{5}\right) \tilde{i}_m(t) \tag{6.4}$$

where $\hat{K}_\nu = 2k_{w\nu}N_s\hat{I}_n/(\pi D)$. Then the torque produced by the mth phase is given by

$$\tau_m(t) = -\frac{D^2 L_{stk}}{4} \int_0^{2\pi} B(\vartheta^e_s, t) K_m(\vartheta^e_s, t) d\vartheta^e_s \tag{6.5}$$

Only harmonics of flux–density and electrical loading of the same order (i.e. $\xi = \nu$) produce a torque contribution different from zero. After some arrangements, the torque of the mth phase becomes

$$\tau_m(t) = -\sum_\nu \left[\frac{\pi}{4} D^2 L_{stk} \hat{B}_\nu \hat{K}_\nu\right] \sin(\nu\varphi_m) \tilde{i}_m(t) \tag{6.6}$$

where φ_m is defined as

$$\varphi_m = \omega t - k_m \frac{2\pi}{5} \tag{6.7}$$

and $\hat{B}_\nu$ and $\hat{K}_\nu$ are the peaks of flux–density and electrical loading harmonic of νth order. The terms within the square bracket in (6.6) are referred to as T_ν. These torque harmonics T_ν are obtained by means of finite element analysis. For the predisposed prototype, the first three terms were T_1= 2.346 Nm, T_3= –0.330 Nm, and T_5= 0.041 Nm at the nominal current $\hat{I}$=0.85 A.

The current functions can be expressed as

$$\tilde{i}_m(t) = \cos(\varphi_m + \alpha^e_i) \tag{6.8}$$

where α^e_i is the current phase and φ_m is given in (6.7). Adopting a surface–mounted PM motor, α^e_i is fixed to $\pi/2$ (i.e. the stator current is controlled to be along the q–axis of the synchronous reference frame). Introducing (6.8) into (6.6), it can be noted that the first addend ($\nu = 1$) of (6.6) consists of a constant term and a term oscillating at 2ω, the second addendum ($\nu = 3$) consists of two terms oscillating at 2ω and 4ω, and so forth as shown in Fig.6.7. The motor total torque can be written as

$$\tau_n(t) = -\sum_m \sum_\nu T_\nu \sin(\nu\varphi_m) \tilde{i}_m(t) \tag{6.9}$$

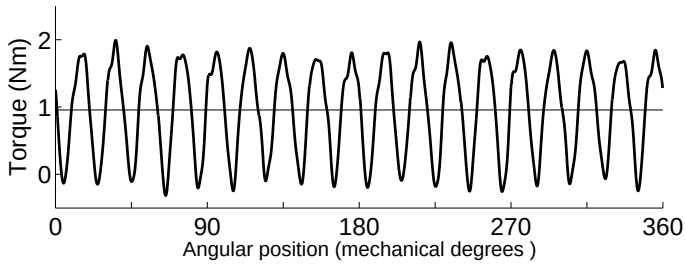

Figure 6.7: Single–layer winding motor. Torque behavior of only one phase.

where $m = a, b, c, d, e$.

Finally, the total torque becomes

$$\tau_n(t) = -\sum_m \sum_\nu T_\nu \sin(\nu\varphi_m)\cos(\varphi_m + \alpha_i^e) \tag{6.10}$$

In healthy mode as shown in Fig. 6.8, only torque harmonics of order $\nu = 1 + 10k$ with $k = 0, \pm1, \pm2, ...$ (i.e. $\nu = 1, 9, 11, 19, 21, ...$) are different from zero [30].

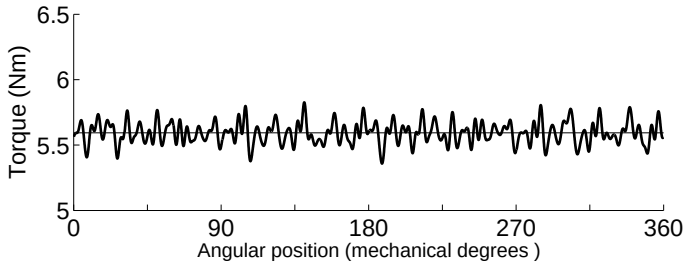

Figure 6.8: Single–layer winding motor. Torque behavior in healthy mode operation (experimental test).

6.4 Strategies for faulty mode current control

The faults that are investigated are the open circuit of one and two phases and the short–circuit of one phase. The proposed current control strategies are chosen so as to achieve a smooth and adequately high torque even in presence of one or two faulty phases. Actually, even if torque amplitude falls down, due to the decreasing number of active phases, the torque profile is maintained fairly smooth.

The motor drive can satisfactorily operate in the presence of fault with a minimum torque ripple. Thanks to the analytical approach, the results can be applied to five–phase motors in a broad power range. Since the current waveforms are sinusoidal or,

at the most, with a third time–harmonic superimposed, they are easily implemented in any control unit.

Current control strategies are considered to the aim of enabling a smooth running after fault. Only fundamental and third time–harmonics of current are considered. Every control strategy is tied by the null zero–sequence current bond (i.e. $\sum \tilde{i} = 0$) and has to deliver a reasonable average torque. Symbol $\tilde{i}_m(t)$ is a dimensionless function that describes the current behavior vs. time (that is vs. rotor position, since $\vartheta_m^e = \omega t$) and subscript m could be $m = a, b, c, d, e$.

Purposely, a smooth torque after fault is sought, accepting a decrease in the average torque. This is not always acceptable: when the application is a compressor or a pump, it is imperative to maintain the nominal torque and speed after fault [21, 29]. On the contrary, the motor considered in this chapter is a low–speed 18–pole motor. An overrated post–fault torque is not a stringent requirement, and the after-fault voltage demand is not a problem.

For each fault, the current control strategy is found by adopting a three–step procedure:

1. the current phasors are tied to satisfy the bond $\sum \tilde{i} = 0$,
2. the second order torque harmonic is cancelled by means of a proper choice of the current phasor angles of the healthy phases,
3. the fourth order torque harmonic is cancelled including the third time–harmonic of current (together with a rearrangement of the angle of the fundamental current phasors).

6.5 One–phase open–circuit fault

In this section, let us suppose that the a–phase remains continuously open due to a fault, i.e. $\tilde{i}_a = 0$. The resulting torque is obtained by subtracting (6.6) from (6.10), yielding

$$\begin{aligned} \tau_{i_a=0}(t) &= \tau_r(t) - \tau_a(t) \\ &= \sum_{m=b,c,d,e} \sum_{\nu} T_\nu \sin(\nu\varphi_m) \cos(\varphi_m + \alpha_i^e) \end{aligned} \tag{6.11}$$

where the loss of the a–phase in the series should be noted. Thus

$$\begin{aligned} \tau_{\tilde{i}_a=0}(t) = \; & T_1[\sin(\varphi_b)\cos(\varphi_b + \alpha_i^e + \beta) + \sin(\varphi_c)\cos(\varphi_c + \alpha_i^e + \gamma) + ...] + \\ & + T_3[\sin(3\varphi_b)\cos(\varphi_b + \alpha_i^e + \beta) + \sin(3\varphi_c)\cos(\varphi_c + \alpha_i^e + \gamma) + ...] + \\ & + T_5[\sin(5\varphi_b)\cos(\varphi_b + \alpha_i^e + \beta) + \sin(5\varphi_c)\cos(\varphi_c + \alpha_i^e + \gamma) + ...] + ... \end{aligned}$$

Since one of the five phases is missed and the torque produced by one–phase contains an average and a pulsating value, thus it is expected a reduction of the

average torque of about 20% and a peak–to–peak torque ripple of about 40% with respect to the healthy–mode operation (that is a ripple of 50% referred to the average torque in faulty–mode operation). Figs. 6.9 and 6.10 shows the torque behavior during healthy–mode operation (dashed line) and under the open–circuited a–phase fault without any change of the other currents (dotted line). The simulated average torque results in 79.5% of the nominal torque (as expected), and the torque ripple is 44% (slightly lower than expected).

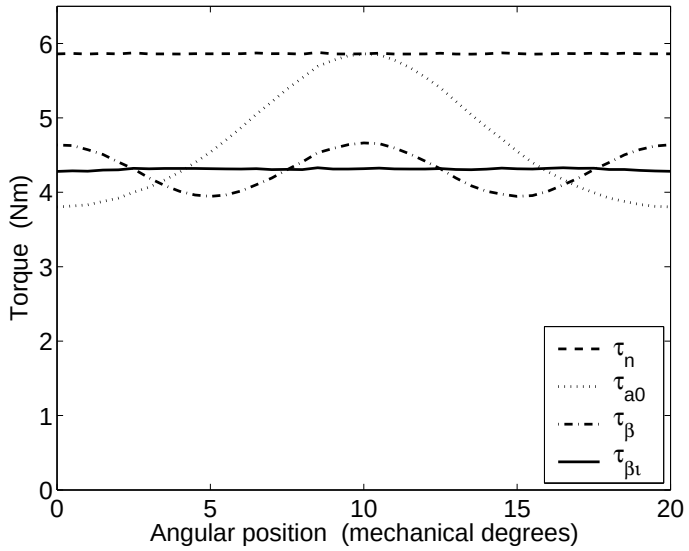

Figure 6.9: Double–layer winding motor. Torque behavior with a–phase open–circuited.

In case of fault, the a–phase current disappears, and the amplitude and phase of the other currents are modified, as sketched in Fig. 6.11. The angles β, γ, δ, ϵ refer to the phase b, c, d, and e respectively. In the research of the more suitable current control, some reasonable constraints are fixed:

1. the first one is to maintain the current amplitude equal for each healthy phase;
2. the second one is to maintain the symmetry with respect the fault. This constraints the current angles to satisfy

$$\begin{aligned} \epsilon &= -\beta \\ \delta &= -\gamma \end{aligned} \tag{6.12}$$

3. the third requirement is that $\sum i = 0$, that is, a null zero–sequence current. Adopting the constraints 1. and 2., this requirement yields a further constraint

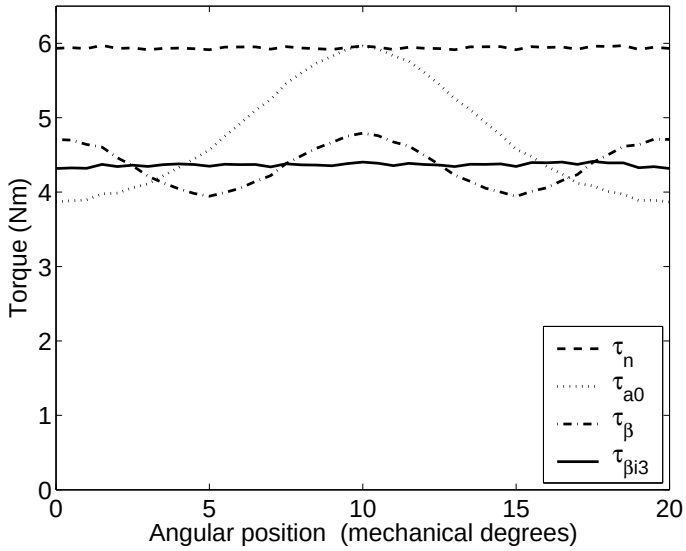

Figure 6.10: Single–layer winding motor. Torque behavior with a–phase open–circuited.

on the current angles, given by

$$\beta + \gamma = \frac{\pi}{5} \tag{6.13}$$

The system of the currents becomes

$$\begin{aligned} \tilde{i}_a(t) &= 0 \\ \tilde{i}_b(t) &= \cos(\varphi_b + \alpha_i^e + \beta) \\ \tilde{i}_c(t) &= \cos(\varphi_c + \alpha_i^e - \beta + \frac{\pi}{5}) \\ \tilde{i}_d(t) &= \cos(\varphi_d + \alpha_i^e + \beta - \frac{\pi}{5}) \\ \tilde{i}_e(t) &= \cos(\varphi_e + \alpha_i^e - \beta) \end{aligned} \tag{6.14}$$

6.5.1 Fundamental harmonic of flux–density

As a first estimation, let us consider only the fundamental harmonic of flux–density distribution (ξ=1 in (6.1)). In this case the torque (6.11), considering the constraint

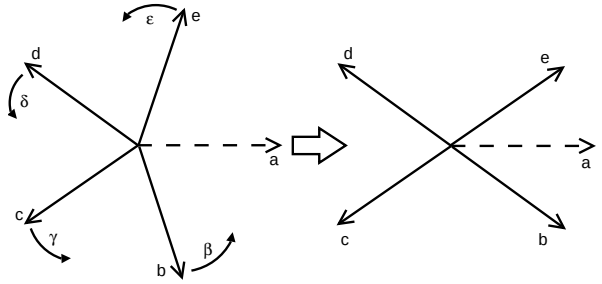

Figure 6.11: Current phasor diagram in case of open–circuited a–phase fault

(6.12), becomes

$$\begin{aligned}\tau'_{\bar{i}_a=0}(t) = \quad & \tfrac{T_1}{2}[\sin(2\varphi_b + \alpha_i^e + \beta) + \sin(-\alpha_i^e - \beta) + \\ & \sin(2\varphi_c + \alpha_i^e - \beta + \tfrac{\pi}{5}) + \sin(-\alpha_i^e + \beta - \tfrac{\pi}{5}) + \\ & \sin(2\varphi_d + \alpha_i^e + \beta - \tfrac{\pi}{5}) + \sin(-\alpha_i^e - \beta + \tfrac{\pi}{5}) + \\ & \sin(2\varphi_e + \alpha_i^e - \beta) + \sin(-\alpha_i^e + \beta)]\end{aligned} \tag{6.15}$$

The condition to obtain a zero torque ripple is to equate the time derivative of (6.15) to zero, achieving

$$\left[\cos\left(\beta - \frac{4\pi}{5}\right) + \cos\left(\beta + \frac{7\pi}{5}\right)\right] = 0 \tag{6.16}$$

that is $\beta = \pi/5 \pm n\pi$, with $n = 0, 1, 2, ...$ Assuming $\beta = \pi/5$ (36 degrees), thus $\gamma = 0$ from (6.13), and $\delta = 0$ and $\epsilon = -\frac{\pi}{5}$ from (6.12). In Fig. 6.11(b) the variation of the current phasors is represented.

Table 6.2: Average torque and ripple

case	$T_{avg}(Nm)$	T_{avg}/T_n	ripple (%)
τ_{nsin}	5.863	1	0.69
$\tau_{i_a=0}$	4.669	0.7954	49.75
τ_{a0be36}	3.897	0.7235	0.85

6.5.2 Complete flux–density waveform, sinusoidal currents

Unfortunately the effect of the harmonics in the flux–density distribution can not negligible. The torque is given by (6.12) and, considering the constraints on the

stator currents, can be rewritten (considering only the first three terms) as

$$\tau_\beta(t) = T_1 A_1(t) + T_3 B_1(t) + T_5 C_1(t) \tag{6.17}$$

in which

$$\begin{aligned} A_1(t) &= 2\cos\left(\beta - \frac{\pi}{10}\right)\cos\frac{\pi}{10} + 2\cos 2\left(\varphi_a + \alpha_i^e\right)\cos\left(\beta + \frac{3\pi}{10}\right)\cos\frac{11\pi}{10} \\ B_1(t) &= 2\cos 2\left(\varphi_a + \alpha_i^e\right)\cos\left(\beta - \frac{\pi}{2}\right)\cos\frac{13\pi}{10} + \\ &+ 2\cos 4\left(\varphi_a + \alpha_i^e\right)\cos\left(\beta + \frac{7\pi}{10}\right)\cos\frac{3\pi}{10} \\ C_1(t) &= 0 \end{aligned} \tag{6.18}$$

In order to reduce the second harmonic of the torque to zero, from (6.17) and (6.18), it has to be satisfy

$$T_1\cos\left(\beta + \frac{3\pi}{10}\right)\cos\frac{11\pi}{10} + T_3\cos\left(\beta - \frac{\pi}{2}\right)\cos\frac{13\pi}{10} = 0 \tag{6.19}$$

that, after some manipulations, yields

$$\tan\beta = \frac{T_1\cos\frac{11\pi}{10}\cos\frac{3\pi}{10}}{T_1\cos\frac{11\pi}{10}\sin\frac{3\pi}{10} - T_3\cos\frac{13\pi}{10}} \tag{6.20}$$

In the case of the motors under test, it has been computed:

$\beta^{(ds)}$=0.581 rad (33.27 degrees) in the case of double–layer winding,

$\beta^{(ss)}$=0.577 rad (33.04 degrees) in the case of single–layer winding.

Let us observe that the two value are slightly different, and they are also different from $\beta=\pi/5$ rad (36 degrees) computed above when the higher order harmonic of flux–density distribution are neglected.

The corresponding torque behaviors are reported in Figs. 6.9 and 6.10 using dot–dash lines. Although the second harmonic has been reduced to zero, it is worth noticing that a fourth–harmonic torque remains. Its amplitude is not negligible, the torque ripple being about 19.5%

6.5.3 Complete flux–density waveform, third time-harmonic current injection

The means to reduce also the fourth–harmonic torque to zero is to inject a third time–harmonic of current. However, since this current harmonic produce both a second and a fourth harmonic in the torque, the fundamental current harmonic has to be modify consequently.

The third current harmonic has been chosen in phase with the fundamental current, and with an rms value I_3. The new system of currents become

$$\begin{aligned}
\tilde{i}_a &= 0 \\
\tilde{i}_b &= \cos(\varphi_b + \alpha_i^e + \beta) + \iota \cos 3(\varphi_b + \alpha_{i3}^e + \beta_3) \\
\tilde{i}_c &= \cos\left(\varphi_c + \alpha_i^e - \beta + \frac{\pi}{5}\right) + \iota \cos 3\left(\varphi_c + \alpha_{i3}^e - \beta_3 + \frac{\pi}{5}\right) \\
\tilde{i}_d &= \cos\left(\varphi_d + \alpha_i^e + \beta - \frac{\pi}{5}\right) + \iota \cos 3\left(\varphi_d + \alpha_{i3}^e + \beta_3 - \frac{\pi}{5}\right) \\
\tilde{i}_e &= \cos(\varphi_e + \alpha_i^e - \beta) + \iota \cos 3(\varphi_e + \alpha_{i3}^e - \beta_3)
\end{aligned} \tag{6.21}$$

where $\iota = I_3/I_1$. In the following it is assumed that $\alpha_{i3}^e = \alpha_i^e$ and $\beta_3 = \beta$.

The torque can be rewritten as

$$\tau_{\beta\iota}(t) = T_1 A_1(t) + T_3 B_1(t) + T_5 C_1(t) + \iota[T_1 D_1(t) + T_3 E_1(t) + T_5 F_1(t)] \tag{6.22}$$

where $A_1(t), B_1(t), C_1(t)$ remain as in (6.18), and

$$\begin{aligned}
D_1(t) &= 2\cos 2\,(\varphi_a + \alpha_i^e)\cos\left(3\beta_3 + \frac{\pi}{10}\right)\cos\frac{9\pi}{10} + 2\cos 4\,(\varphi_a + \alpha_i^e)\cos\left(3\beta_3 + \frac{\pi}{2}\right)\cos\frac{\pi}{10} \\
E_1(t) &= 2\cos\left(3\beta_3 - \frac{3\pi}{10}\right)\cos\frac{3\pi}{10} + 2\cos 6\,(\varphi_a + \alpha_i^e)\cos\left(\beta_3 + \frac{7\pi}{10}\right)\cos\frac{3\pi}{10} \\
F_1(t) &= 0
\end{aligned} \tag{6.23}$$

The two conditions to reduce the second and the fourth torque harmonics to zero are

$$T_1 \cos(\beta + \tfrac{3\pi}{10})\cos\tfrac{11\pi}{10} + T_3 \sin\beta \cos\tfrac{13\pi}{10} + \iota T_1 \cos(3\beta_3 + \tfrac{\pi}{10})\cos\tfrac{9\pi}{10} = 0 \tag{6.24}$$

$$T_3 \cos(\beta + \tfrac{7\pi}{10})\cos\tfrac{3\pi}{10} + \iota T_1 \cos(3\beta_3 + \tfrac{\pi}{2})\cos\tfrac{\pi}{10} = 0 \tag{6.25}$$

where the two unknowns are β and ι. The solution of system (6.24) is

$$\beta = -\frac{3\pi}{10} + \arccos\left\{-\frac{T_3 \cos\frac{3\pi}{10}}{T_1 \cos\frac{\pi}{10}}\left[\sin\beta + \frac{\cos(\beta + \frac{7\pi}{10})\cos(3\beta + \frac{\pi}{10})}{\sin 3\beta}\right]\right\} \tag{6.26}$$

and

$$\iota = -\frac{T_3 \cos\frac{3\pi}{10}\cos(\beta + \frac{7\pi}{10})}{T_1 \cos\frac{\pi}{10}\cos(3\beta + \frac{\pi}{2})} \tag{6.27}$$

In the case of the motors under test, it results

$\beta^{(ds)}$=0.551 rad (31.6 degrees) and $\iota^{(ds)}$=0.0806 in the case of double–layer winding,

$\beta^{(ss)}$=0.546 rad (31.3 degrees) and $\iota^{(ss)}$=0.0876 in the case of single–layer winding.

By feeding the healthy phases using these values for β and ι a smooth torque is obtain as shown in Figs. 6.9 and 6.10 (solid lines). Although the average torque is slightly reduced, becoming about 73.5% or the nominal torque, the peak–to–peak torque ripple remains limited to 2%. The results are reported in Table 6.3.

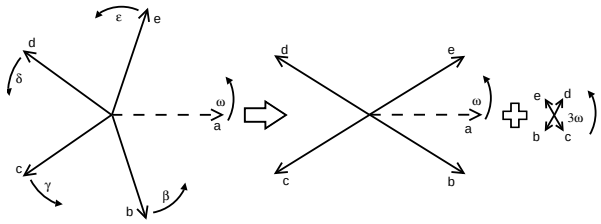

Figure 6.12: Current phasors with $\beta = -\epsilon = 31.6^o$, $\iota = 0.08$ and $\gamma = -\delta = 4.4^o$

Table 6.3: Average torque and torque ripple with different current control strategies corresponding to Fig.6.9 and Fig.6.10

double–layer			
case	$T_{avg}(Nm)$	T_{avg}/T_n	ripple(%)
τ_n	5.863	1	0.4
τ_{a0}	4.669	0.796	44.12
τ_β	4.31	0.735	16.67
$\tau_{\beta\iota}$	4.31	0.735	1.16
single–layer			
case	$T_{avg}(Nm)$	T_{avg}/T_n	ripple(%)
τ_n	5.939	1	0.98
τ_{a0}	4.731	0.797	44.26
τ_β	4.37	0.736	19.46
$\tau_{\beta\iota}$	4.366	0.735	2.19

6.5.4 Experimental results

The current control strategies computed above have been tested adopting a 3–phase inverter. The coils of e– and c–phase are connected together (with opposite polarity) and similarly the coils of the b–phase and d–phase. The currents are forced as described above. The measured torque vs. mechanical angle is reported in Fig. 6.13 and Fig. 6.14.

Fig. 6.13(a) and Fig. 6.14(a) show the measured torque behaviors imposing $\beta = \pi/5$ radians. It is evident a torque ripple higher than 25% and a decrease of the average torque of 20%, as predicted in the analytical study (see Table 6.3). The highest torque harmonics are of second and fourth order (i.e. with 18 and 36 periods per rotor turn). Figs. 6.13(b) and 6.14(b) and Figs. 6.13(c) and 6.14(c) highlight the favorable effect of the post fault control strategies, proposed above. It is worth noticing that with this latter current control strategy both torque harmonics of second and fourth order are strongly reduced.

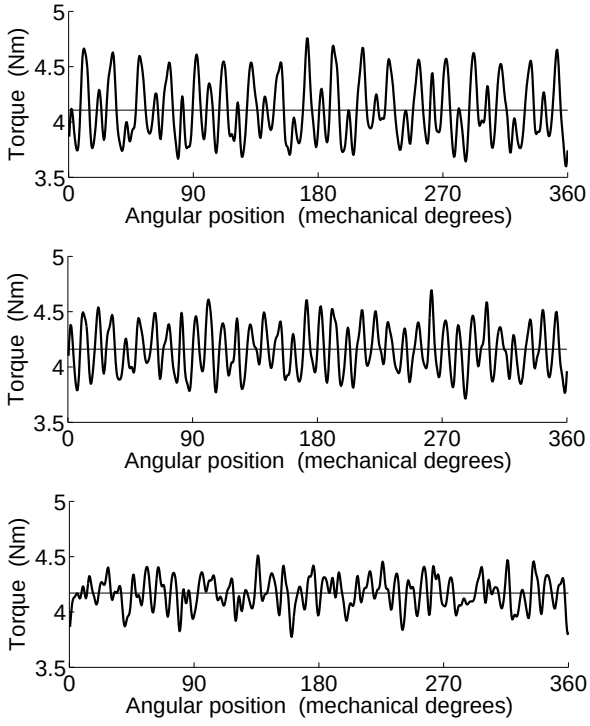

Figure 6.13: Double–layer winding motor. Open circuit of one phase: torque behaviors measured: (a) $\beta = \pi/5$ radians and ι=0, (b) β=0.581 radians and ι=0, (c) β=0.551 radians and ι=0.0806. (Experimental tests)

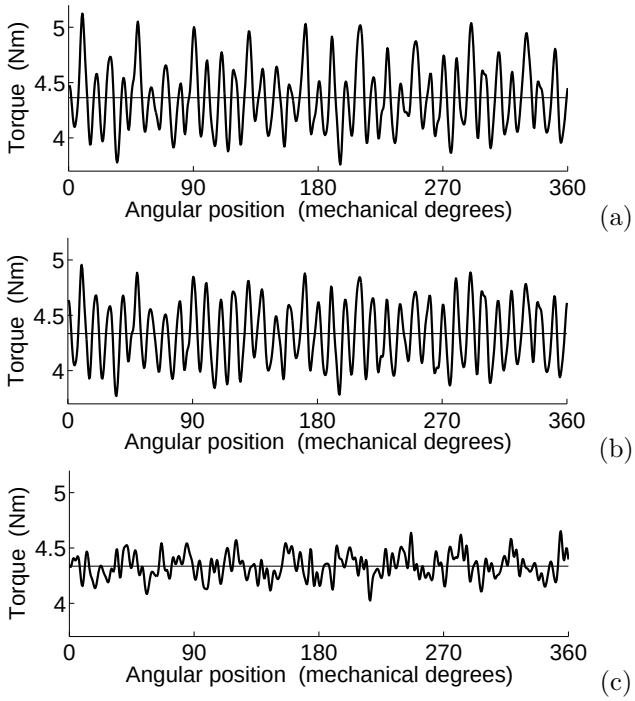

Figure 6.14: Single–layer winding motor. Open circuit of one phase: torque behaviors measured: (a) $\beta = \pi/5$ radians and ι=0, (b) β=0.577 radians and ι=0, (c) β=0.546 radians and ι=0.0876. (Experimental tests)

6.6 Two open–circuited non–adjacent phases

6.6.1 Sinusoidal currents

In this subsection, let us consider that the amplitude of the healthy phase current is equal. The fault implies $\tilde{i}_b = 0$ and $\tilde{i}_e = 0$, while the other currents can be expressed as

$$\begin{aligned} \tilde{i}_a &= \cos(\varphi_a + \alpha_i^e + \alpha) \\ \tilde{i}_c &= \cos(\varphi_c + \alpha_i^e + \gamma) \\ \tilde{i}_d &= \cos(\varphi_d + \alpha_i^e + \delta) \end{aligned} \tag{6.28}$$

where the positive direction of α, γ and δ is the counterclockwise direction.

The constraint of having symmetry with respect to the faulty phase yields

$$\begin{aligned} \alpha &= 0, \\ \delta &= -\gamma \end{aligned} \tag{6.29}$$

and the constraint of having $\sum i = 0$ yields

$$\begin{aligned} \gamma &= 2\pi/15\,\text{rad}(24\text{degrees}), \\ \delta &= -2\pi/15\text{rad}(-24\text{degrees}). \end{aligned} \tag{6.30}$$

The resulting system of currents corresponds to the well–known symmetrical three–phase current system (three phasors of equal amplitude and $2\pi/3$ rad out of phase). However, only a marginal improvement is carried out as regards the resulting torque behavior: the average torque reduces to 56.8% of the rated torque torque and the torque ripple is about 33%.

From that results, it is realized that the imposed constraints are too heavy. The requirement of equal amplitude of the current of the healthy phase is removed.

6.6.2 Sinusoidal currents, but with different amplitude

The new current system becomes

$$\begin{aligned} \tilde{i}_a &= \cos(\varphi_a + \alpha_i^e + \alpha) \\ \tilde{i}_c &= \rho_1 \cos(\varphi_c + \alpha_i^e + \gamma) \\ \tilde{i}_d &= \rho_1 \cos(\varphi_d + \alpha_i^e + \delta) \end{aligned} \tag{6.31}$$

where an equal factor ρ_1 has been added to both the currents i_c and i_d, to maintain the symmetry with respect to the faulty phases. The symmetry yields (6.29), while the constraint $\sum \tilde{i} = 0$ yields

$$\rho_1 = \frac{-1}{2\cos(\gamma - \frac{4\pi}{5})} \tag{6.32}$$

Using the current system (6.31), the torque (neglecting the term T_5 with respect to T_1 and T_3) becomes

$$\tau_{\rho\gamma}(t) = T_1 A_4(t) + T_3 B_4(t) \tag{6.33}$$

where

$$A_4(t) = \frac{1}{2} + \rho_1 \cos\gamma + \left[\frac{1}{2} + \rho_1 \cos\left(\gamma + \frac{2\pi}{5}\right)\right] \cos 2(\varphi_a + \alpha_i^e) \tag{6.34}$$

$$B_4(t) = \left[\frac{1}{2} + \rho_1 \cos\left(\gamma - \frac{2\pi}{5}\right)\right] \cos 2(\varphi_a + \alpha_i^e) + \tag{6.35}$$

$$+ \left[\frac{1}{2} + \rho_1 \cos\left(\gamma + \frac{4\pi}{5}\right)\right] \cos 4(\varphi_a + \alpha_i^e) \tag{6.36}$$

The condition to reduce the second harmonic of the torque to zero is

$$T_1 \left[\frac{1}{2} + \rho_1 \cos\left(\gamma + \frac{2\pi}{5}\right)\right] + T_3 \left[\frac{1}{2} + \rho_1 \cos\left(\gamma - \frac{2\pi}{5}\right)\right] = 0 \tag{6.37}$$

from which, together with (6.32), one obtains

$$\tan\gamma = \frac{(T_1+T_3)\sin\frac{3\pi}{5}\sin\frac{\pi}{5}}{T_1\sin\frac{3\pi}{5}\cos\frac{\pi}{5}+T_3\sin\frac{\pi}{5}\cos\frac{3\pi}{5}} \tag{6.38}$$

In the case of the motors under test, from (6.38) and (6.32), it has been computed:

$\gamma^{(ds)}$=0.544 rad (31.15 degrees) and $\rho_1^{(ds)}$=1.287 in case of double–layer winding,

$\gamma^{(ss)}$=0.536 rad (30.70 degrees) and $\rho_1^{(ss)}$=1.264 in case of single–layer winding.

The corresponding torque behaviors are reported in Figs. 6.16 and 6.17. Dashed line refers to the healthy operating condition, dotted line refers to the faulty operating condition with no modification of the currents: a high second harmonic of the torque is evident. The dot–dash line refers to the current control strategy just presented: the second harmonic of the torque is reduced to zero and only a fourth torque harmonic remains.

It is worth noticing that the currents in the c and d phases result 28.7% higher than the nominal value (see factor ρ_1). This implies that the Joule losses increase of about 66%, however this is not dangerous since it compensates only partially the loss of two–phase.

6.6.3 Third time-harmonic current injection

As in the previous case, a third time-harmonic current is injected to the aim of reduce also the fourth torque harmonic. The system of the healthy currents becomes

$$\begin{aligned}
\tilde{i}_a(t) &= \cos(\varphi_a+\alpha_i^e)+\iota\cos 3(\varphi_a+\alpha_{i3}^e)\\
\tilde{i}_c(t) &= \rho_1\cos(\varphi_c+\alpha_i^e+\gamma)+\iota\rho_3\cos 3(\varphi_c+\alpha_{i3}^e+\gamma)\\
\tilde{i}_d(t) &= \rho_1\cos(\varphi_d+\alpha_i^e-\gamma)+\iota\rho_3\cos 3(\varphi_d+\alpha_{i3}^e-\gamma)
\end{aligned} \tag{6.39}$$

where factor ρ_3 has been introduced for the third harmonic. In addition, $\alpha_{i3}^e=\alpha_i^e$ and $\gamma_3=\gamma$ are fixed. To the aim of satisfying the symmetry (6.29) holds, while of satisfying the constraint $\sum i=0$ (6.32) and

$$\rho_3 = \frac{-1}{2\cos(3\gamma-\frac{2\pi}{5})} \tag{6.40}$$

hold.

The torque can be expressed as

$$\tau_{\rho\gamma\iota}(t) = T_1A_4(t)+T_3B_4(t)+\iota[T_1C_4(t)+T_3D_4(t)] \tag{6.41}$$

where the terms $A_4(t)$ and $B_4(t)$ are given in (6.34), and

$$C_4(t) = \left[\frac{1}{2} + \rho_3 \cos\left(3\gamma + \frac{2\pi}{5}\right)\right] \cos 2(\varphi_a + \alpha_i^e) + \tag{6.42}$$

$$+ \left[\frac{1}{2} + \rho_3 \cos\left(3\gamma + \frac{4\pi}{5}\right)\right] \cos 4\,(\varphi_a + \alpha_i^e) \tag{6.43}$$

$$D_4(t) = \left[\frac{1}{2} + \rho_3 \cos 3\gamma\right] + \left[\frac{1}{2} + \rho_3 \cos\left(3\gamma - \frac{4\pi}{5}\right)\right] \cos 6\,(\varphi_a + \alpha_i^e) \tag{6.44}$$

From (6.41) and (6.42), one can reduce the second and the fourth torque harmonics to zero by setting

$$T_1 \left[\frac{1}{2} + \rho_1 \cos\left(\gamma + \frac{2\pi}{5}\right)\right] + T_3 \left[\frac{1}{2} + \rho_1 \cos\left(\gamma - \frac{2\pi}{5}\right)\right] +$$

$$+\iota T_1 \left[\frac{1}{2} + \rho_3 \cos\left(3\gamma + \frac{2\pi}{5}\right)\right] = 0 \tag{6.45}$$

$$T_3 \left[\frac{1}{2} + \rho_1 \cos\left(\gamma + \frac{4\pi}{5}\right)\right] + \iota\ T_1 \left[\frac{1}{2} + \rho_3 \cos\left(3\gamma + \frac{4\pi}{5}\right)\right] = 0 \tag{6.46}$$

that, together with (6.32) and (6.40), form a system of four equations in the unknowns γ, ι, ρ_1 and ρ_3. Its solution yields

$$\gamma = \frac{\pi}{5} + \arcsin\left\{-\frac{T_3 \sin\frac{\pi}{5}}{T_1 \sin\frac{2\pi}{5}} \left[\sin(\gamma - \frac{3\pi}{5}) - \frac{\sin\gamma \sin 3\gamma}{\sin(3\gamma + \frac{\pi}{5})}\right]\right\} \tag{6.47}$$

and

$$\iota = -\frac{T_3 \sin\frac{4\pi}{5} \cos(3\gamma - \frac{2\pi}{5}) \sin\gamma}{T_1 \sin\frac{3\pi}{5} \cos(\gamma - \frac{4\pi}{5}) \sin(3\gamma + \frac{\pi}{5})}. \tag{6.48}$$

and then ρ_1 and ρ_3 are achieved from (6.32) and (6.40).

In case of the motors under test, it can be computed as

$\gamma^{(ds)}$=0.495 rad (28.33 degrees), $\iota^{(ds)}$=-0.108, $\rho_1^{(ds)}$=1.154, and $\rho_3^{(ds)}$=-0.513 in the case of double–layer winding,

$\gamma^{(ss)}$=0.484 rad (27.75 degrees), $\iota^{(ss)}$=-0.112, $\rho_1^{(ss)}$=1.130, and $\rho_3^{(ss)}$=-0.510 in the case of single–layer winding.

The resulting torque behaviors are shown in Fig. 6.16 and 6.17, while the numerical results are reported in Table 6.4.

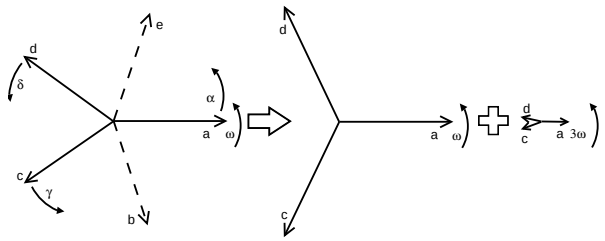

Figure 6.15: Current phasors with γ=28.33 deg, ρ_1=1.154, ρ_3=-0.513 and ι=-0.108

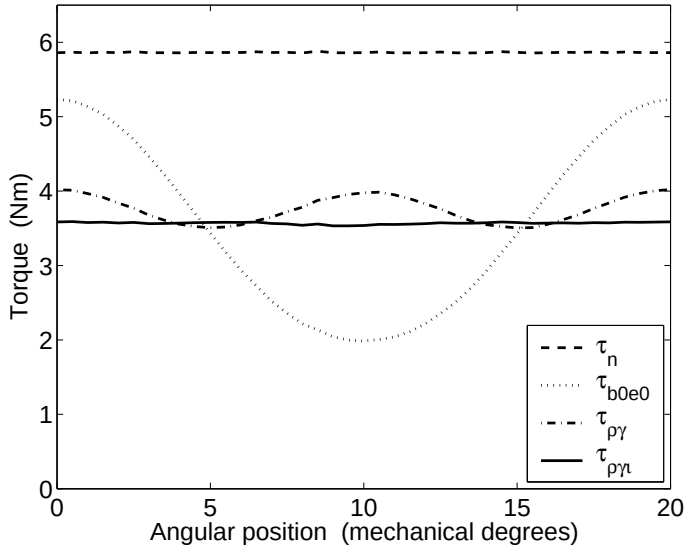

Figure 6.16: Double–layer winding motor. Torque behavior with the non–adjacent b– and e–phase open circuit fault (Finite element simulation).

6.6.4 Experimental results

The currents are forced in the coils as described above, achieving $\tau_{\rho\gamma}$ and $\tau_{\rho\gamma\iota}$. The measured torques vs. mechanical angle are reported in Fig. 6.18 and Fig. 6.19. As far as the average value is concerned, both torques $\tau_{\rho\gamma}$ and $\tau_{\rho\gamma\iota}$ reach the predicted values (over than 3.7 Nm and over 3.5 Nm respectively for both motors).

The torque ripple is almost as predicted. The torque harmonic of fourth order (i.e. with 36 periods per rotor turn) is visible in Fig. 6.18(a) and Fig. 6.19(a). It disappears when the third time–harmonic is adopted, as shown in Fig. 6.18(a) and Fig. 6.19(b). Although the behavior of the two motors is similar, the lower ripple are

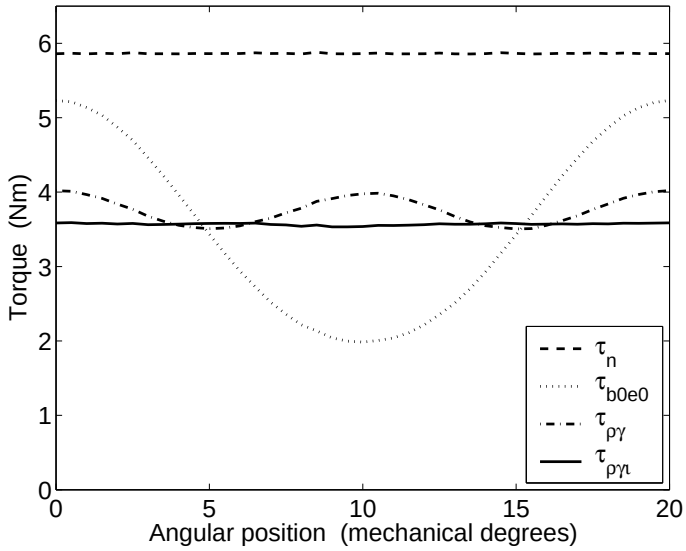

Figure 6.17: Single–layer winding motor. Torque behavior with the non–adjacent b– and e–phase open circuit fault (Finite element simulation).

found with single–layer winding motor.

Table 6.4: Average torque and torque ripple with different current control strategies corresponding to Fig. 6.16 .

double–layer			
case	$T_{avg}(Nm)$	T_{avg}/T_n	ripple(%)
τ_n	5.863	1	0.40
τ_{b0e0}	3.560	0.607	91.21
$\tau_{\rho\gamma}$	3.758	0.641	13.72
$\tau_{\rho\gamma\iota}$	3.569	0.609	1.59
single–layer			
case	$T_{avg}(Nm)$	T_{avg}/T_n	ripple(%)
τ_n	5.939	1	0.98
τ_{b0e0}	3.608	0.608	88.77
$\tau_{\rho\gamma}$	3.768	0.634	15.46
$\tau_{\rho\gamma\iota}$	3.578	0.602	3.11

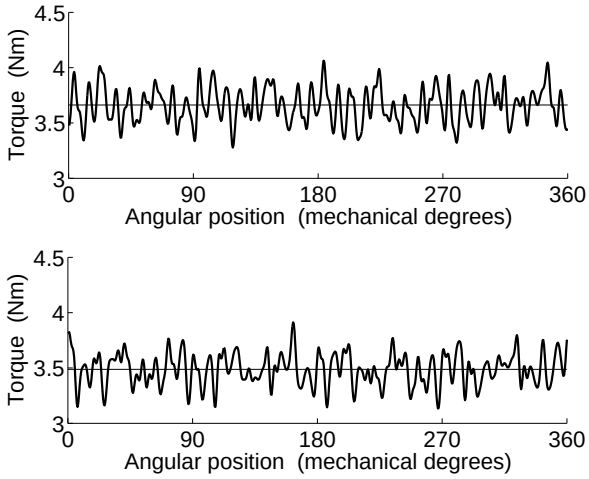

Figure 6.18: Double–layer winding. Open circuit of two non–adjacent phases: torque behavior (a) without and (b) with third time–harmonic of current (Experimental test).

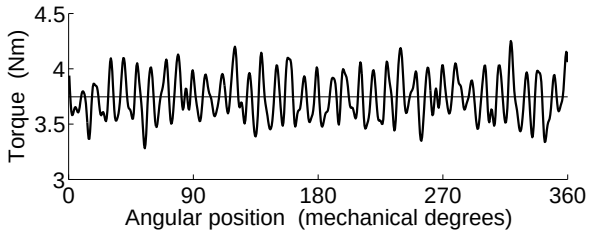

(a)

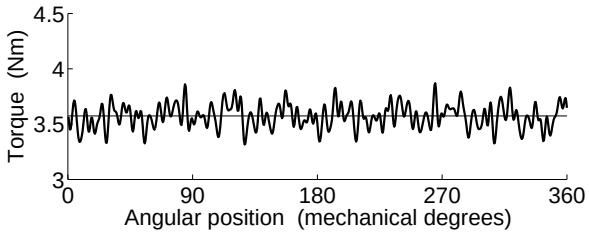

(b)

Figure 6.19: Single–layer winding. Open circuit of two non–adjacent phases: torque behavior (a) without and (b) with third time–harmonic of current (Experimental test).

6.7 Two open–circuited adjacent phases

6.7.1 Sinusoidal currents

In this subsection, let us consider that the amplitude of the healthy phase current is equal. The fault implies $\tilde{i}_c = 0$ and $\tilde{i}_d = 0$, while the other currents can be expressed as

$$\begin{aligned} \tilde{i}_a(t) &= \cos(\varphi_a + \alpha_i^e + \alpha) \\ \tilde{i}_b(t) &= \cos(\varphi_b + \alpha_i^e + \beta) \\ \tilde{i}_e(t) &= \cos(\varphi_e + \alpha_i^e + \varepsilon) \end{aligned} \tag{6.49}$$

where the positive direction of α, β and ε is the counterclockwise direction, as shown in Fig. 6.23. The torque becomes

$$\begin{aligned} \tau_{c0d0}(t) &= T_1[\cos^2(\varphi_a + \alpha_i^e) + \cos^2(\varphi_b + \alpha_i^e) + \cos^2(\varphi_e + \alpha_i^e)] + \\ &+ T_3[\cos(\varphi_a + \alpha_i^e)\cos 3(\varphi_a + \alpha_{i3}^e) + \qquad (6.50) \\ &+ \cos(\varphi_b + \alpha_i^e)\cos 3(\varphi_b + \alpha_{i3}^e) + \cos(\varphi_e + \alpha_i^e)\cos 3(\varphi_e + \alpha_{i3}^e)] \quad (6.51) \end{aligned}$$

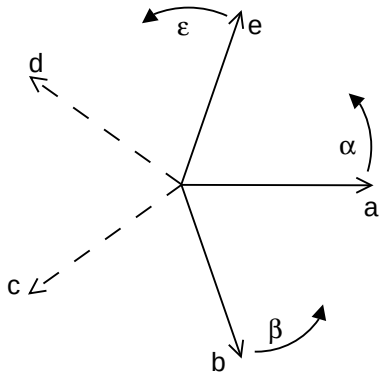

Figure 6.20: Current phasor with open–circuited of b and e phases

The symmetry with respect the faulty phases requires

$$\begin{aligned} \alpha &= 0 \\ \epsilon &= -\beta, \end{aligned} \tag{6.52}$$

while the constraint $\sum i = 0$ imposes

$$\begin{aligned} \beta &= -4\pi/15 \ (-48 \text{ degrees}) \\ \epsilon &= 4\pi/15 \ (48 \text{ degrees}) \end{aligned} \tag{6.53}$$

coming back to the result of the symmetrical three–phase current system (three phasors of equal amplitude and $2\pi/3$ rad out of phase). However, as above, the result is not acceptable: the average torque reduces to about 42% of the rated torque with a torque ripple higher than 100%. Thus, the constraint of having an equal amplitude of the current of the healthy phase has to be removed.

6.7.2 Sinusoidal currents, but with different amplitude

The new current system (with $\tilde{i}_c = 0$ and $\tilde{i}_d = 0$) becomes

$$\begin{aligned} \tilde{i}_a(t) &= \cos(\varphi_a + \alpha_i^e + \alpha) \\ \tilde{i}_b(t) &= \rho_1 \cos(\varphi_b + \alpha_i^e + \beta) \\ \tilde{i}_e(t) &= \rho_1 \cos(\varphi_e + \alpha_i^e + \epsilon) \end{aligned} \tag{6.54}$$

The symmetry with the fault requires to satisfy (6.53) while the $\sum \tilde{i} = 0$ yields

$$\rho_1 = \frac{-1}{2\cos(\beta - \frac{2\pi}{5})} \tag{6.55}$$

The torque becomes

$$\tau_{\rho\beta}(t) = T_1 A_6(t) + T_6 B_6(t) \tag{6.56}$$

with

$$A_6(t) = \frac{1}{2} + \rho_1 \cos\beta + \left[\frac{1}{2} + \rho_1 \cos\left(\beta - \frac{4\pi}{5}\right)\right] \cos 2(\varphi_a + \alpha_i^e) \tag{6.57}$$

$$B_6(t) = \left[\frac{1}{2} + \rho_1 \cos\left(\beta + \frac{4\pi}{5}\right)\right] \cos 2(\varphi_a + \alpha_i^e) + \tag{6.58}$$

$$+ \left[\frac{1}{2} + \rho_1 \cos\left(\beta + \frac{2\pi}{5}\right)\right] \cos 4(\varphi_a + \alpha_i^e) \tag{6.59}$$

The second torque harmonic is reduced to zero by imposing

$$T_1 \left[\frac{1}{2} + \rho_1 \cos\left(\gamma - \frac{4\pi}{5}\right)\right] + T_3 \left[\frac{1}{2} + \rho_1 \cos\left(\gamma + \frac{4\pi}{5}\right)\right] = 0 \tag{6.60}$$

that, together with the imposed constraints, yields

$$\tan\beta = \frac{(T_1 + T_3)\sin\frac{\pi}{5}\sin\frac{3\pi}{5}}{T_1 \sin\frac{\pi}{5}\cos\frac{3\pi}{5} - T_3 \sin\frac{3\pi}{5}\cos\frac{\pi}{5}} \tag{6.61}$$

In the case of the motors under test, it has been computed:

$\beta^{(ds)}$ = -1.419 rad (-81.31 degrees) and $\rho_1^{(ds)} = 0.560$ in the case of double–layer winding,

$\beta^{(ss)}$ = -1.437 rad (-82.34 degrees) and $\rho_1^{(ss)} = 0.555$ in the case of single–layer winding.

The corresponding torque behaviors is shown in Figs. 6.21 and 6.22 using dot–dash line. The numerical results are reported in Table 6.5.

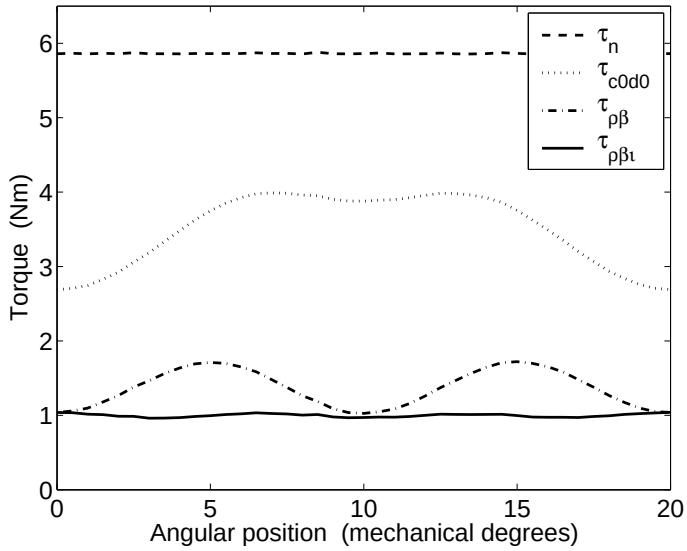

Figure 6.21: Double–layer winding motor. Torque behavior with c– and d–phases open–circuited.

6.7.3 Third time-harmonic current injection

By introducing the third time-harmonic of the current, the current system becomes

$$\begin{aligned}
\tilde{i}_a(t) &= \cos(\varphi_a + \alpha_i^e) + \iota \cos 3(\varphi_a + \alpha_{i3}^e) \\
\tilde{i}_b(t) &= \rho_1 \cos(\varphi_b + \alpha_i^e + \beta) + \iota\rho_3 \cos 3(\varphi_b + \alpha_{i3}^e + \beta_3) \\
\tilde{i}_e(t) &= \rho_1 \cos(\varphi_e + \alpha_i^e - \beta) + \iota\rho_3 \cos 3(\varphi_e + \alpha_{i3}^e - \beta_3)
\end{aligned} \tag{6.62}$$

where $\alpha_{i3}^e = \alpha_i^e$ is fixed. Factor ρ_3 is chosen with the constraint of having zero–sequence current equal to zero, which is

$$\rho_3 = \frac{-1}{2\cos(3\beta_3 - \frac{6\pi}{5})} \tag{6.63}$$

The torque is given by

$$\tau_{\rho\beta i3}(t) = T_1 A_6(t) + T_3 B_6(t) + \iota[T_1 C_6(t) + T_3 D_6(t)] \tag{6.64}$$

where $A6(t)$ and $B6(t)$ are given in (6.57) and

$$\begin{aligned}
C_6(t) &= \left[\frac{1}{2} + \rho_3 \cos\left(3\beta_3 - \frac{4\pi}{5}\right)\right] \cos 2(\varphi_a + \alpha_i^e) + \left[\frac{1}{2} + \rho_3 \cos\left(3\beta_3 + \frac{2\pi}{5}\right)\right] \cos 4(\varphi_a + \alpha_i^e) \\
D_6(t) &= \left[\frac{1}{2} + \rho_3 \cos 3\beta_3\right] + \left[\frac{1}{2} + \rho_3 \cos\left(3\beta_3 - \frac{2\pi}{5}\right)\right] \cos 6(\varphi_a + \alpha_i^e)
\end{aligned} \tag{6.65}$$

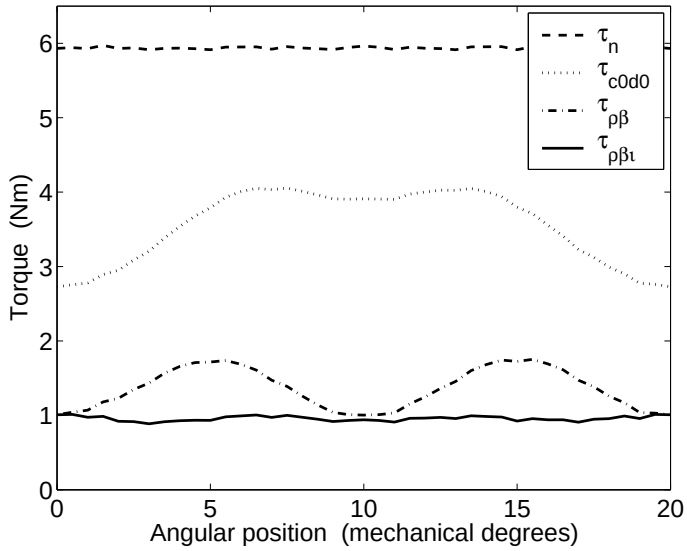

Figure 6.22: Single–layer winding motor. Torque behavior with c– and d–phases open–circuited.

The conditions to reduce the second and fourth torque harmonic to zero are

$$T_1\left[\frac{1}{2}+\rho_1\cos\left(\beta-\frac{4\pi}{5}\right)\right]+T_3\left[\frac{1}{2}+\rho_1\cos\left(\beta+\frac{4\pi}{5}\right)\right] \quad + \\ +\iota T_1\left[\frac{1}{2}+\rho_3\cos\left(3\beta_3-\frac{4\pi}{5}\right)\right] \quad = \quad 0 \qquad (6.66)$$

$$T_3\left[\frac{1}{2}+\rho_1\cos\left(\beta+\frac{2\pi}{5}\right)\right]+\iota T_1\left[\frac{1}{2}+\rho_3\cos\left(3\beta_3+\frac{2\pi}{5}\right)\right] \quad = \quad 0 \qquad (6.67)$$

that, together with (6.55) and (6.63), form a system of four equations in the four unknown β, ι, ρ_1, and ρ_3 (with $\beta_3=\beta$).

However, this system does not yield any acceptable solution (there are problems of instability of the solutions and high value of the currents). From the physical point of view, effect of the third time–harmonic of the a–phase current tends to decrease the effects of the third time–harmonic of the c– and d–phase currents, instead of compensate the torque harmonics due to the loss of the b– and e–phases. To the aim of obviating this limitation, a third time–harmonic current is supplied only in the c– and d–phases. To satisfy the constraint $\sum i=0$, this current have equal amplitude (ρ_3 will be fixed to unity) and an opposite phase angle. In this case we should distinguish the angles β for the fundamental current and β_3 for the third current harmonic. The

condition $i_{3b} + i_{3e} = 0$ yields

$$\cos 3(\varphi_b + \alpha_i^e + \beta_3) + \cos 3(\varphi_e + \alpha_i^e - \beta_3) = 0 \tag{6.68}$$

that is

$$3\beta_3 + \frac{4\pi}{5} = \pm\frac{\pi}{2} \tag{6.69}$$

In the following, it is fixed $\beta_3 = \pi/10$.

In the torque equation (6.64), the factor $C_6(t)$ and $D_6(t)$ have to replaced by

$$\begin{aligned} C_7(t) &= \cos\frac{9\pi}{10}\cos 2(\varphi_a + \alpha_i^e) + \cos\frac{\pi}{10}\cos 4(\varphi_a + \alpha_i^e) \\ D_7(t) &= \cos\frac{3\pi}{10} + \cos\frac{7\pi}{10}\cos 6(\varphi_a + \alpha_i^e) \end{aligned} \tag{6.70}$$

The conditions to reduce the second and fourth torque harmonic to zero become

$$\begin{aligned} T_1\left[\frac{1}{2} + \rho_1\cos\left(\gamma - \frac{4\pi}{5}\right)\right] + T_3\left[\frac{1}{2} + \rho_1\cos\left(\gamma + \frac{4\pi}{5}v\right)\right] + \iota T_1\cos\frac{9\pi}{10} &= 0 \\ T_3\left[\frac{1}{2} + \rho_1\cos\left(\beta + \frac{2\pi}{5}\right)\right] + \iota T_1\cos\frac{\pi}{10} &= 0 \end{aligned} \tag{6.71}$$

Using (6.55), from (6.71) the unknown ι can be expressed as a function of β:

$$\iota = -\frac{T_3\sin\frac{2\pi}{5}\sin\beta}{T_1\cos\frac{\pi}{10}\cos(\beta - \frac{2\pi}{5})} \tag{6.72}$$

and β is computed by an iterative process from

$$\beta = -\frac{2\pi}{5} - \arcsin\left\{\frac{T_3\sin\frac{2\pi}{5}}{T_1\sin\frac{\pi}{5}}\left[\sin(\beta + \frac{\pi}{5}) + \sin\beta\right]\right\} \tag{6.73}$$

In case of the motors under test, it can be computed as

$\beta^{(ds)}$=-1.696 rad (-97.15 degrees), $\iota^{(ds)}$=0.142, and $\rho_1^{(ds)}$=0.509 in the case of double–layer winding,

$\beta^{(ss)}$=-1.742 rad (-99.84 degrees), $\iota^{(ss)}$=0.153, and $\rho_1^{(ss)}$=0.505 in the case of single–layer winding.

and the corresponding current phasors are shown in Fig. 6.23.

The resulting torque behavior is shown in Figs. 6.21 and 6.22 using solid line. It is worth noticing that the torque ripple is minimized but the cost is a high reduction of the average torque. The numerical values are reported in Table 6.5, referring the ripple to the corresponding average torque.

From these results, one can observe that the effect of the constraint of $\sum i = 0$ (a zero–sequence current equal to zero) on the average torque is well evident. The

average torque collapses. A current control strategy exists able to achieve a smooth torque behavior. For this purpose, the adoption of a full–bridge converter appears advantageous. Each phase could be supplied independently and a zero–sequence current is feasible. The average torque obtained removing this constraint highlights the opportunity of using a converter that allows a zero–sequence current. A suitable current control strategy can be found also in this case so as to achieve a smooth torque (torque ripple about 8%), without a high decrease of average torque (about 58%). However, this falls out the objective of this chapter and will be not dealt with.

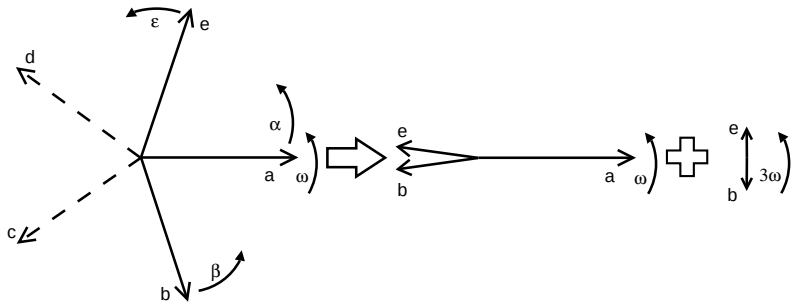

Figure 6.23: Current phasors with β=-97 degrees, ι=0.142 and $\rho_1 = 0.5$

Table 6.5: Average torque and torque ripple with different current control strategies corresponding to Fig. 6.21 and Fig. 6.22.

double–layer			
case	$T_{avg}(Nm)$	T_{avg}/T_n	ripple(%)
τ_n	5.863	1	0.40
τ_{c0d0}	3.499	0.597	37.18
$\tau_{\rho\beta}$	1.364	0.233	50.88
$\tau_{\rho\beta\iota}$	0.999	0.170	7.86
single–layer			
case	$T_{avg}(Nm)$	T_{avg}/T_n	ripple(%)
τ_n	5.939	1	0.98
τ_{c0d0}	3.536	0.597	37.45
$\tau_{\rho\beta}$	1.359	0.229	55.07
$\tau_{\rho\beta\iota}$	0.958	0.161	13.25

6.7.4 Experimental results

The currents are forced in the coils as described above, achieving $\tau_{\rho\beta}$ and $\tau_{\rho\beta\iota 3}$. The measured torques vs. mechanical angle are reported in Fig. 6.24 and Fig. 6.25. The estimated decrease of average torque is verified: the average torque is about 1.5 Nm in both motors (i.e. 25% of nominal torque), when sinusoidal current waveforms are imposed. The average torques decreases to about 1 Nm (i.e. 17% of nominal torque) in both motors, when third time–harmonics of current are injected. It is worth to observe the good agreement with the predicted results reported in Table 6.5.

It can be also observed that a torque harmonic of fourth order (i.e. with 36 periods per rotor turn) is evident in Fig. 6.24(a) and Fig. 6.25(a). It disappears when the third time–harmonic is adopted, as shown in Fig. 6.24(b) and Fig. 6.25(b).

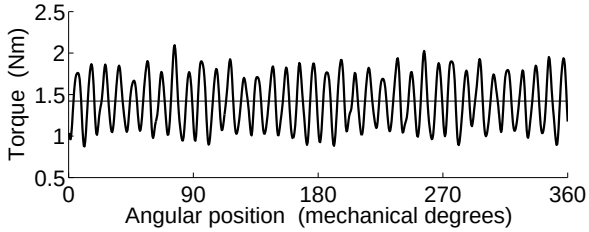

(a)

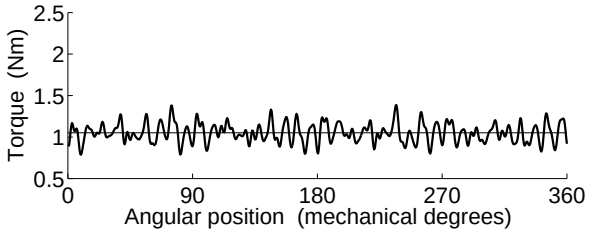

(b)

Figure 6.24: Double–layer winding. Open circuit of two adjacent phases: torque behavior (a) without and (b) with third time–harmonic of current (Experimental test).

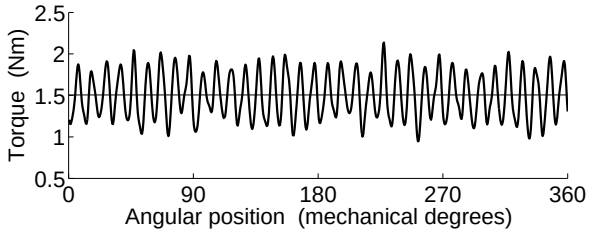

(a)

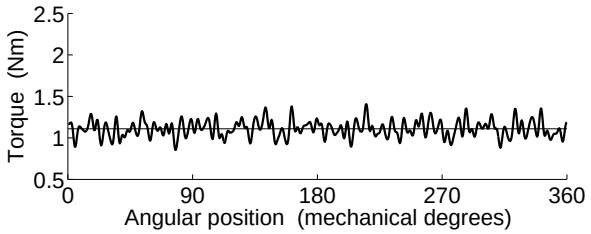

(b)

Figure 6.25: Single–layer winding. Open circuit of two adjacent phases: torque behavior (a) without and (b) with third time–harmonic of current (Experimental test).

6.8 Short circuit fault of one phase

In this section, let us suppose that the a–phase is short–circuited. In the computation of the short–circuit current the mutual inductances can be reasonably neglected with respect to the self inductances (as verified in the 20–slot 18–pole motor under test). A limited or null mutual coupling among the phases is essential in fault–tolerant motors: it has to be avoided that the flux produced by the healthy phases may be coupled by the short–circuited phase, sustaining the fault. Thus, considering the fundamental components only, the short–circuit current is computed as

$$i_{shc}(t) = -\frac{\omega\hat{\Lambda}}{Z_{sch}}\sin(\omega t - \phi_{shc}) \tag{6.74}$$

where $e(t) = \omega\hat{\Lambda}\sin(\omega t)$ is the back EMF, with $\hat{\Lambda}$ the flux–linkage due to the PM, $Z_{shc} = \sqrt{R^2 + (\omega L)^2}$ is the phase impedance formed by the series resistance and reactance, ϕ_{shc} is the impedance phase ($\tan\phi_{shc} = \omega L/R$). If the resistance R is negligible with respect to the reactance ωL, the short–circuit current becomes $\hat{I}_{shc} = -\hat{\Lambda}/L$. Then, from (6.74) it is evident that each phase of the fault–tolerant motor has to exhibit a suitably high inductance, so as to limit the short–circuit current.

In order to test the short circuit effect, the terminal of the a–phase have been short–circuited. The other four coils have been connected two by two, so as a 3–phase inverter can be adopted.

The short circuit current is lower than nominal current at rotor speeds lower than 100 rpm, while it becomes 1.5 times higher at 200 rpm (nominal speed). It is shown

in Fig. 6.26(a) and Fig. 6.26(b) with and without healthy phase currents, respectively, at rotor speed of 43 rpm. From this test it is possible to note that (**i**) the amplitude of the short circuit current is limited and (**ii**) it is the same in the two operating conditions (due to the negligible mutual coupling between phases).

From Fig. 6.26 the experimented third time–harmonic current is about 14% of the fundamental one. This confirms the presence of the third time–harmonic of the back EMF, due to the third space harmonic of air–gap flux density distribution and the winding factor of third harmonic different from zero.

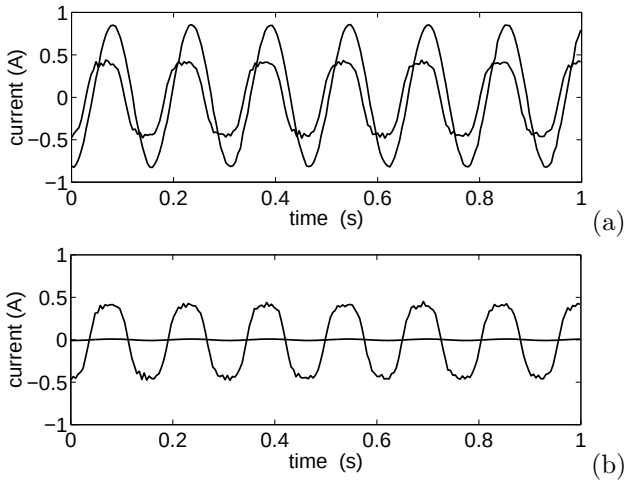

Figure 6.26: Measured short circuit current (a) with and (b) without currents in healthy phases, at rotor speed of 43 rpm.

6.8.1 Sinusoidal currents of different amplitude

The considered system of current functions is

$$\begin{aligned}
\tilde{i}_a &= \iota_{shc} \sin(\omega t - \phi_{shc}) \\
\tilde{i}_b &= (1-\kappa) \cos(\phi_b + \alpha_i^e + \tfrac{\pi}{5} + \phi) \\
\tilde{i}_c &= (1+\kappa) \cos(\phi_c + \alpha_i^e - \phi) \\
\tilde{i}_d &= (1-\kappa) \cos(\phi_d + \alpha_i^e + \phi) \\
\tilde{i}_e &= (1+\kappa) \cos(\phi_e + \alpha_i^e - \tfrac{\pi}{5} - \phi)
\end{aligned} \tag{6.75}$$

where $\iota_{shc} = \hat{I}_{shc}/\hat{I}_n$ is the ratio between short circuit and nominal currents, κ and ϕ consider the variation of amplitude and phase of the healthy phase currents. It is also assumed that ι_{shc} and ϕ_{shc} are known, since they only depend on motor parameters and operating speed. The system (6.75) implicitly satisfies the constraints of symmetry with respect to the faulty phase and $\sum \tilde{i} = 0$: b– and d–phase currents are chosen

π radians out of phase, and similarly the c– and e–phase currents. Consequently the amplitude of the opposite currents are chosen to be equal.

The corresponding torque is computed introducing (6.75) into (6.9). To the aim of reducing the torque ripple also in faulty mode, the second order torque harmonic is equated to zero,

Of course ι_{shc} and ϕ_{shc} vary with the frequency. Fig. 6.27 shows the values of ϕ and κ as a function of ι_{shc} and ϕ_{shc}.

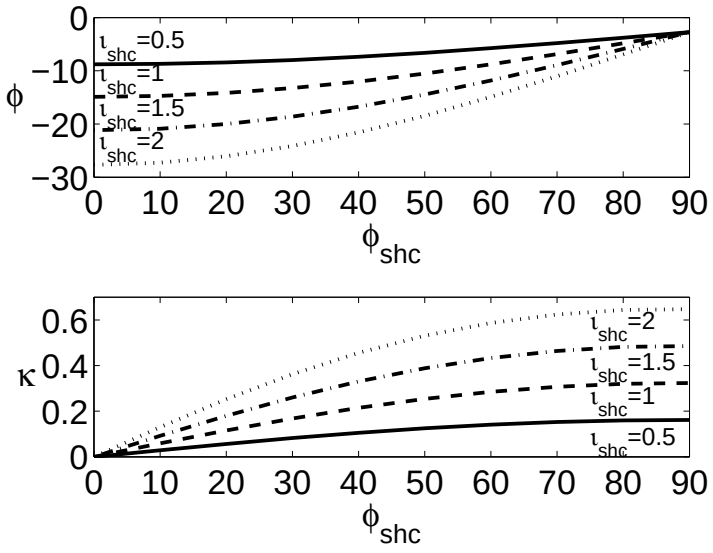

Figure 6.27: ϕ and κ as a function of ι_{shc} and ϕ_{shc}

Assuming $\iota_{shc} = 1$ and ϕ_{shc}=80 degrees, it results ϕ=–4.83 degrees and κ=0.32.

Fig. 6.28(a) shows the torque behavior with a–phase short circuit fault and current phasors rotated of $\delta = \gamma = 0$ and $\beta = -\epsilon = \pi/5$ (see left hand side of Fig. 6.11 for reference angles) Referring to following subsection, this corresponds to κ=0 and ϕ=0 in (6.75). Fig. 6.28(b) shows the torque behavior with current phasors computed according to the proposed strategy, that is, with κ and ϕ computed from Fig. 6.27 at the actual motor speed. Thus, the average torque remains the same but the torque ripple is effectively reduced.

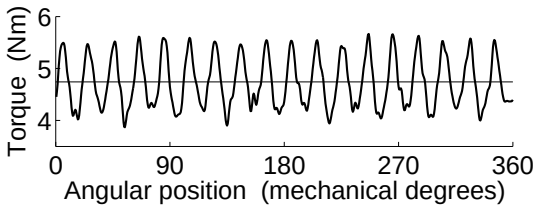

(a)

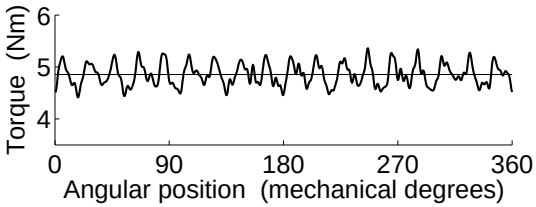

(b)

Figure 6.28: Short circuit of one phase: torque behaviors (a) with κ=0 and ϕ=0 and (b) adopting the proposed strategy: κ and ϕ computed from Fig. 6.27 (Experimental test).

6.9 Open circuit fault with zero–sequence current control

The proposed current control strategies are chosen so as to achieve a smooth and adequately high torque even in presence of one or two faulty phases. Actually, even if torque amplitude falls down, due to the decreasing number of active phases, the torque profile is maintained fairly smooth. The motor drive can satisfactorily operate in the presence of fault with a minimum torque ripple. Thanks to the analytical approach, the results can be applied to five–phase motors in a broad power range. Since the current waveforms are sinusoidal or, at the most, with a third time–harmonic superimposed, they are easily implemented in any control unit. Current control strategies are considered to the aim of enabling a smooth running after fault. With a full–bridge converter as shown in Fig.5.4 fundamental, third time–harmonics and zero–sequence current (i.e. $\sum i \neq 0$) current are considered. Purposely, a smooth torque after fault is sought, and the maximum average torque. This is possible thanks to the zero–sequence current.

6.10 One–phase open circuit fault with zero–sequence current control

Each healthy phase maintains the same current amplitude. The current symmetry is maintained by assuming that $\epsilon = -\beta$ and $\delta = -\gamma$.

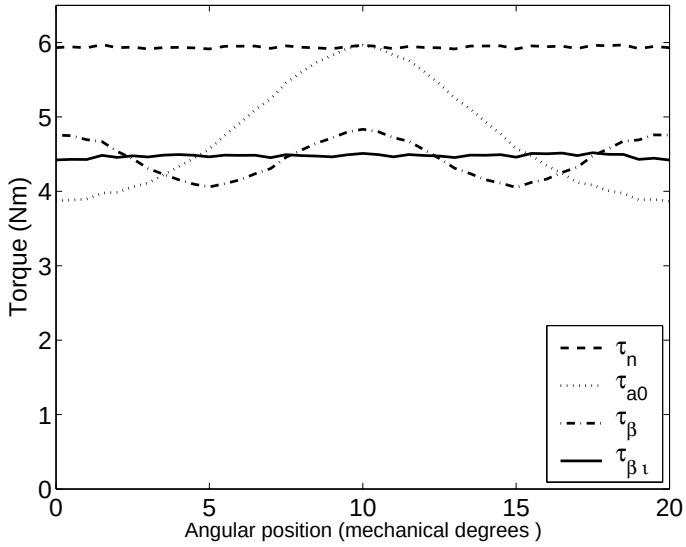

Figure 6.29: Single–layer winding motor. Torque behavior with a–phase open–circuited with zero–sequence current (Finite element simulation).

Then, by imposing these currents in the torque equation and equating the second order harmonic of the torque to zero, the optimal value for β can be found analytically. It is $\beta = 0.516rad$, for the single–layer winding prototype. The corresponding torque behavior (labeled t_β) is drawn with a dot–dashed line in Fig. 6.29. Although the second order harmonic has been reduced to zero, a fourth order torque harmonic still remains. Its amplitude, higher than 15%,is not negligible at all.

In order to reduce also the fourth order torque harmonic to zero, a third time–harmonic of current is injected. However, since this current harmonic produces a torque harmonic of both second and fourth order, the fundamental current harmonic has to be modified consequently. The current control strategies computed above have been tested adopting a 5-phase full–bridge inverter. The measured torque vs. mechanical angle is reported in Fig.6.30. Fig. 6.30(a) shows the measured torque behaviors imposing in healthy–mode operation. Fig. 6.30(c) and Fig. 6.30(d) highlight the favorable effect of the post fault control strategies, proposed above. It is worth noticing that with this latter current control strategy both torque harmonics of second and fourth order are strongly reduced as shown in Table 6.6.

Table 6.6: Average torque and torque ripple with different current control strategies corresponding to Fig. 6.29 .

	single–layer		
case	$T_{avg}(Nm)$	T_{avg}/T_n	ripple(%)
τ_n	5.939	1	0.98
τ_{a0}	4.731	0.797	44.26
τ_β	4.447	0.749	17.57
$\tau_{\beta\iota}$	4.476	0.754	2.19

Table 6.7: Average torque and torque ripple with different current control strategies corresponding to Fig. 6.31 .

	single–layer		
case	$T_{avg}(Nm)$	T_{avg}/T_n	ripple(%)
τ_n	5.939	1	0.98
τ_{c0d0}	3.607	0.607	88.77
$\tau_{\rho\beta}$	3.768	0.634	15.45
$\tau_{\rho\beta\iota}$	3.578	0.602	3.10

6.11 Two open–circuited non–adjacent phases with zero–sequence current control

The choice of the faulty phases is completely arbitrary: $b-$ and $e-$ phases are chosen for the sake of simplicity. Assuming that healthy phase currents remain unchanged, the torque behaviors are shown in Fig. 6.31. Dashed line (τ_n) refers to the healthy operating condition, dotted line (τ_{b0e0}) refers to the faulty operating condition with no variation of the currents: a high second order torque harmonic is evident. Numerical values are reported in Table 6.11. The decrease of average torque results about 40% of the nominal torque τ_n, as expected due to the loss of two of five phases, while the torque ripple is about 90% that can not be accepted.

The currents are forced in the coils as described above, achieving τ_γ and $\tau_{\gamma\iota}$. The measured torques vs. mechanical angle are reported in Fig.6.32. As far as the average value is concerned, both torques τ_γ and $\tau_{\gamma\iota}$ reach the predicted values (over than 3.7 Nm and over 3.5 Nm respectively for the single–layer winding). The torque ripple is almost as predicted. The torque harmonic of fourth order (i.e. with 36 periods per rotor turn) is visible in Fig. 6.32(b). It disappears when the third time–harmonic is adopted, as shown in Fig. 6.32(d).

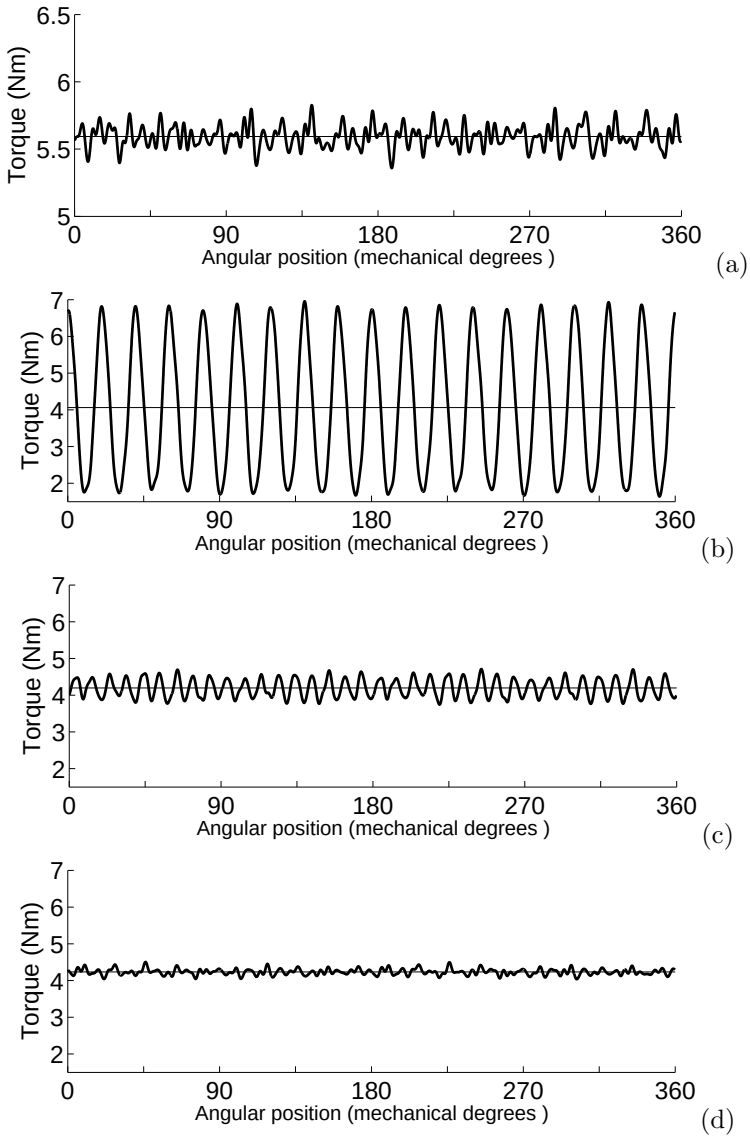

Figure 6.30: Single–layer winding motor. Open circuit of one phase: torque behaviors measured: (a) healthy operation mode, (b) β=0 radians and ι=0, (c) β=0.516 radians and ι=0, (d) β=0.449 radians and ι=0.0867. (Experimental tests)

6.12 Two adjacent open–circuited phase with zero–sequence current

In this case, the $c-$ and $d-$ phases are considered to be open circuited. Assuming that healthy phase currents remain unchanged, the resulting torque behaviors are shown in

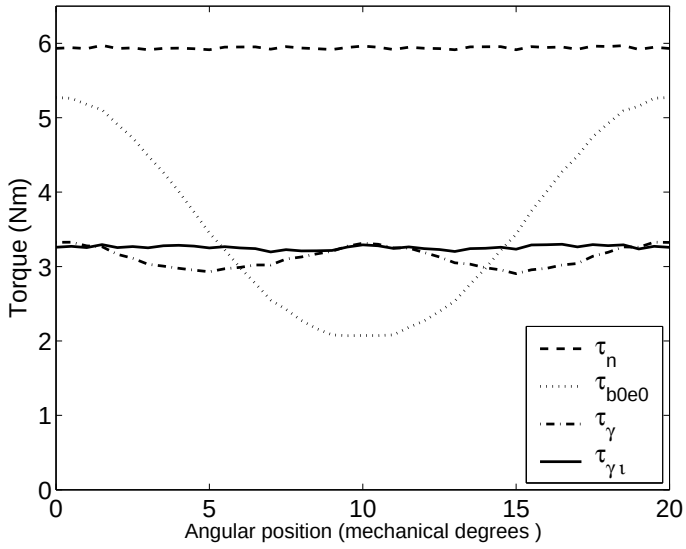

Figure 6.31: Single–layer winding motor. Torque behavior with the non–adjacent b– and e–phase open circuit fault and zero–sequence current control (Finite element simulation).

Fig. 6.33 using dotted line (τ_{c0d0}). The motor performance are reported in Table 6.8. As above, the decrease of average torque is again about 40% of the nominal torque, as expected due to the loss of two of five phases. The torque ripple is about 60%, and the zero–sequence current becomes 1.62 times higher than the nominal current.

The currents are forced in the coils as described above, achieving τ_β and $\tau\beta\iota$. The measured torques vs. mechanical angle are reported in Fig. 6.33. The estimated decrease of average torque is verified: the average torque is about 3.1 Nm (i.e. 54% of nominal torque), when sinusoidal current waveforms are imposed. The average torques increases to about 3.2 Nm (i.e. 55% of nominal torque), when third time–harmonics of current are injected. It is worth to observe the good agreement with the predicted results reported in Table 6.8. It can be also observed that a torque harmonic of fourth order (i.e. with 36 periods per rotor turn) is evident in Fig.6.34(b). It disappears when the third time–harmonic is adopted, as shown in Fig.6.34(d). Comparing the torque behavior with the same fault shown in Fig. 6.25(b) it results that the injection of the zero sequence of current yields an increase of the mean torque of almost 3 times.

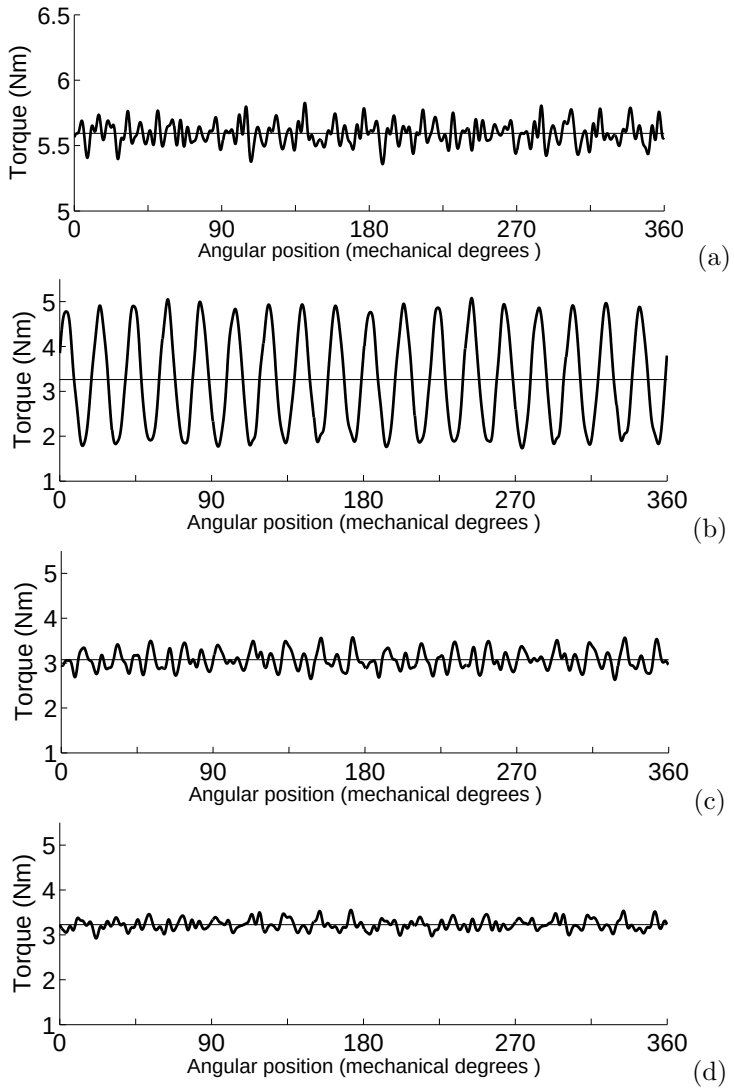

Figure 6.32: Single–layer winding. Open circuit of two non–adjacent phases: torque behavior (a) healthy operation mode, (b) γ=0 radians and ι=0, (c) γ=0.619 radians and ι=0, (d) γ=0.519 radians and ι=0.122. (Experimental test).

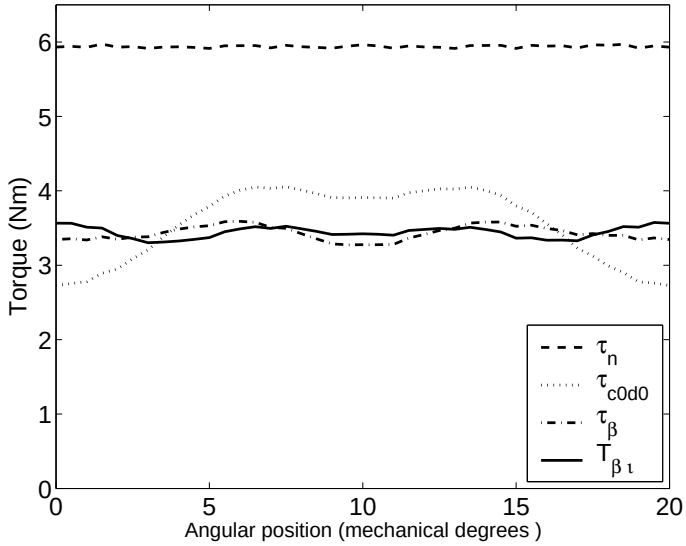

Figure 6.33: Single–layer winding motor. Torque behavior with the adjacent c– and d–phase open circuit fault and zero–sequence current control (Finite element simulation).

Table 6.8: Average torque and torque ripple with different current control strategies corresponding to Fig. 6.33 .

	single–layer		
case	$T_{avg}(Nm)$	T_{avg}/T_n	ripple(%)
τ_n	5.939	1	0.98
τ_{c0d0}	3.607	0.607	88.77
$\tau_{\rho\beta}$	3.124	0.548	13.54
$\tau_{\rho\beta\iota}$	3.256	0.548	3.19

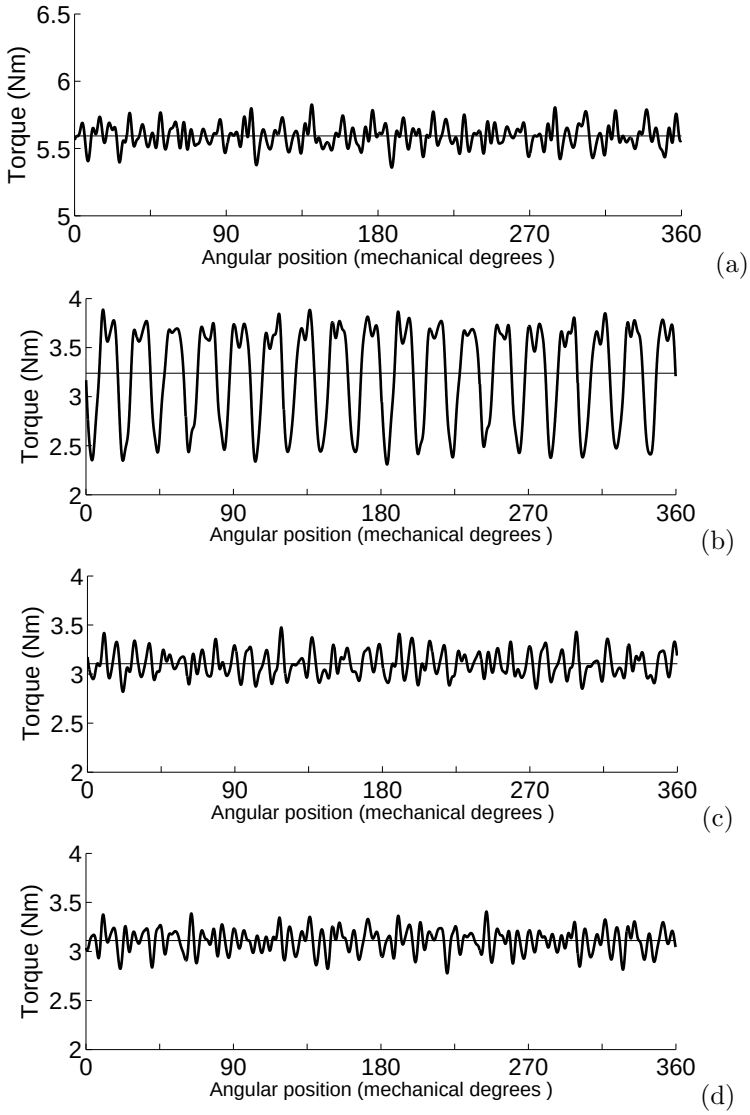

Figure 6.34: Single–layer winding. Open circuit of two adjacent phases: torque behavior (a) healthy operation mode, (b) β=0 radians and ι=0, (c) β=0.336 radians and ι=0, (d) β=0.348 radians and ι=-0.107. (Experimental test).

6.13 Thermal analysis

This section highlights that the physically separation between the phases increase the thermal isolation.

In case of one–phase short circuit fault the current in the faulty phase becomes 4-times the nominal current and the Joule losses in the coils produce an increase of the temperature. The physically separation between the phases reduces the fault propagation. A thermal analysis with finite element method is carried out as shown in Fig.6.35. For a good agreement of the simulation and the measure on the real prototype a special care has to devote to the thermal resistance, in particular it is very important the air layer between stator and case with a width equal to 0.1 mm. The machine losses considered in the thermal analysis are the winding losses P_{Cu}, the back iron losses P_{bi}, the teeth losses P_t. The thermal resistances consider the radial heat transmission in the shaft R_{sh}, the yoke R_{yoke}, the PM R_{pm}, the airgap R_{gap},the tooth R_t, the insulating lining R_{ins}, the copper into the slot R_{Cu}, the back iron R_{bi}, the case R_{case} and, at last, the air layer R_{air}.

As regard the motor components conductivity, a radial section of the motor is considered for the thermal analysis. The materials conductivities considered in the radial analysis are reported in Table 6.9.

Table 6.9: Materials conductivity for radial analysis [W=mK]

MATERIAL	SYMBOL	(W/mK)
$Insulating\ lining$	λ_{ins}	0.15
$Equivalent\ Varnish$	λ_{Cu-var}	0.771
$Iron$	λ_{Fe}	83
$Aluminium$	λ_{Al}	220
Air	λ_{air}	0.026
$Airgap$	λ_{gap}	0.097
$Permanent\ magnet$	λ_{pm}	9
$Shaft$	λ_{sh}	70

Fig.6.35 shows a thermal analysis with FEM and it shows the increase of the temperature only in the slot with the faulty phase. Therefore the machine can operate with a short circuit fault indefinitely and with 80% of nominal torque as shown in section 6.8.

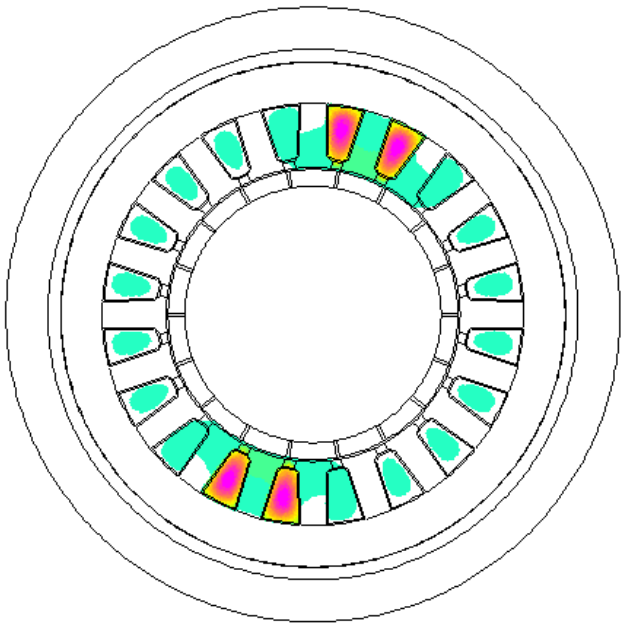

Figure 6.35: Thermal analysis in case of short-circuit fault

6.14 Conclusions

In post–fault operations, optimal current amplitudes and current phases are only slightly modified with respect to the healthy conditions. Sinusoidal currents are required or, at the most, with an additional third time–harmonic term.

It has been shown that the currents that have to be supplied in a five–phase PM motor in presence of an open–circuit fault can be computed analytically. Simulations and experimental tests confirmed that a smooth torque with a reasonably high average value can be obtained. The experimental tests also verified the advantageous effect of the introduction of the third time–harmonic of current on the torque ripple reduction.

It has been also verified that the current control strategies can be applied to five–phase PM motor with both double–layer and single–layer winding. When correctly supplied, both motors exhibit a smooth and high torque, even in faulty–mode operation.

Current amplitudes remain almost the same as in healthy–mode operation, with a maximum overrating of 30%. Thus, the current reaction (which is higher in single–layer winding motor) has a marginal effect on motor performance.

Chapter 7

The 12–slot 10-pole PM Motor

This chapter deals with the analysis of three–phase fractional–slot PM motors with 12-slots and 10-poles and non–overlapped coils. It is suitable for fault–tolerant applications.

In order to verify the fault–tolerant capability of the motor, some motor parameter are measured. Two motors with two different windings are compared: double– and single–layer respectively.

7.1 Three–phase PM machines

The three–phase PM motor with fractional slot winding has been proposed for its inherently high fault–tolerant capability to reduce the fault occurrence, as well as to operate indefinitely in the presence of fault. In fact, many applications require a fault–tolerant capability to electrical motor drives, for instance automotive [20] and aeronautic applications [21].

The electric power in a three–phase motor is divided into two inverters, reducing the power of each inverter. In addition, with two independent inverters, in the event of failure of one inverter, the remaining inverter let the motor to operate properly.

Two PM motor prototypes are considered.

They are characterized by a double– and a single–layer winding, respectively as shown in Fig. 7.1 and their star of slots (Fig.7.2) are useful for calculation of several coefficient, as explained in section 2.3.

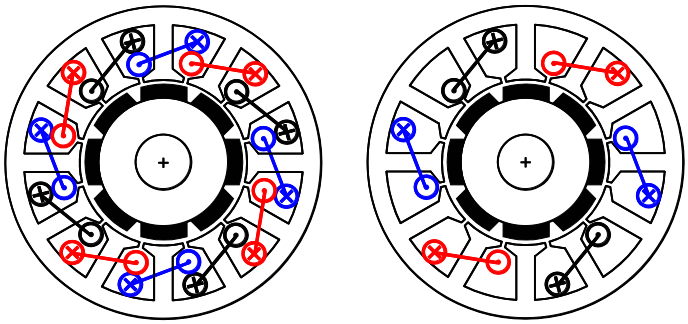

Figure 7.1: Three–phase 12–slot 10–pole PM motors with double– and single–layer winding

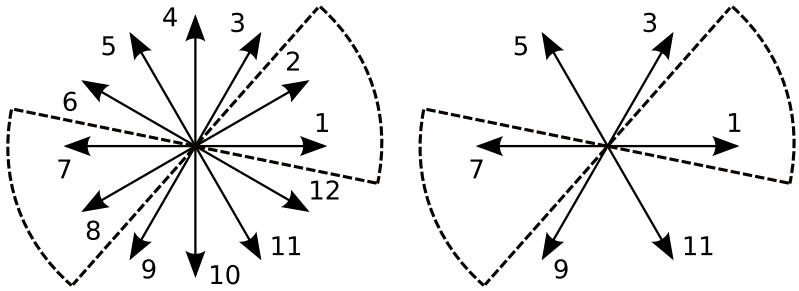

Figure 7.2: Three–phase 12–slot 10–pole machine: double– and single–layer star of slots

7.2 Prototypes used in experimental tests

Two 12–slot 10–pole prototype has been realized. Fig. 7.3 shows the 10–pole rotor with surface–mounted PMs and Fig. 7.4 shows the two stators: with double– and single–layer winding respectively. Finally, Fig. 7.5 shows a particular of the single–layer winding. The physical separation between the phases is evident.

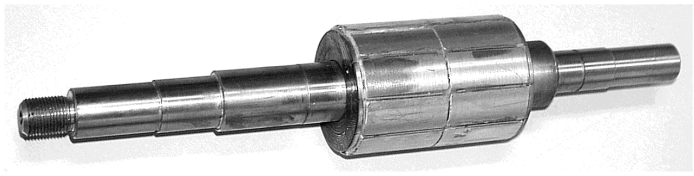

Figure 7.3: Ten–pole rotor used in the machine prototype

Figure 7.4: The two stators used in the prototype

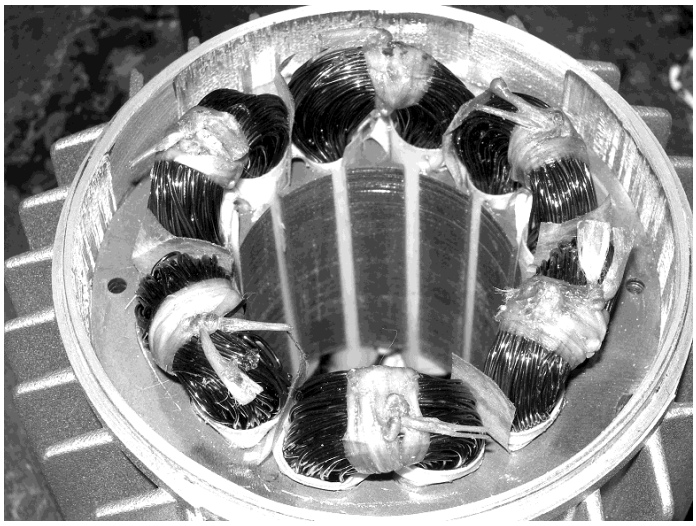

Figure 7.5: Particular of the single–layer winding

7.3 Torque ripple

A key advantage of the PM motors with fractional–slot winding is their low torque ripple. The measured torques versus position of the two motor prototypes are reported in Figs. 7.6 to 7.8. Fig. 7.6 shows the cogging torque, of course the same for the two motors. The cogging torque is quite low, even though it results slightly higher than predicted. This is probably due to a minor dissymmetry of the rotor.

Fig. 7.7 shows the torque at the nominal current of the motor with the double–layer winding, and Fig. 7.8 shows the torque at the nominal current of the motor with the single–layer winding. It is worth noticing that the peak to peak torque ripple is quite low, with a higher value (about 9%) when the single–layer winding is adopted. This is due to the higher MMF harmonic contents. The same ripple has be also found in [10].

However, the unbalanced radial forces, which cause magnetic noise, have not to be left out, as also observed in [8, 31, 32]. Minimum unbalanced radial forces occur adopting solutions with t even and/or Q/t even (or $Q/(2t)$ even in case of single–layer winding).

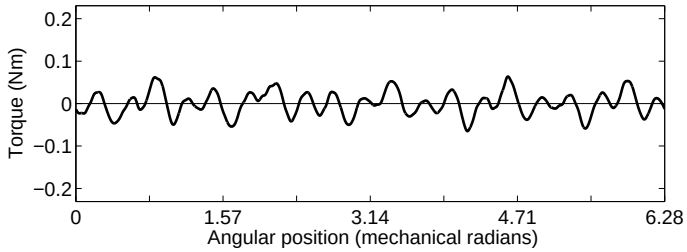

Figure 7.6: Cogging torque versus rotor position (experimental test)

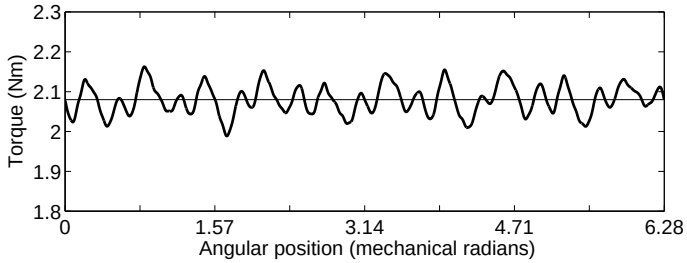

Figure 7.7: Torque versus rotor position at nominal current with the double–layer winding (experimental test).

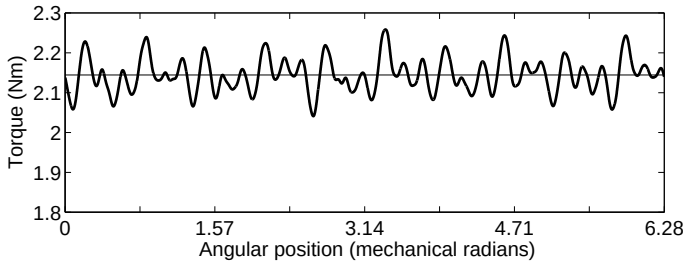

Figure 7.8: Torque versus rotor position at nominal current with the single–layer winding (experimental test).

7.4 Presence of MMF harmonics and their order

The machine with 12 slots and 10 poles yields t=1, Q/t and $Q/(2t)$ even. Due to the low machine periodicity (t=1), the sub–harmonic of order ν=1 exists, as shown in the upper part of Fig. 7.9. Then, only harmonics of odd order exist (i.e. ν=5, 7, 11, 13, ...). When the double–layer winding is transformed into a single–layer one, the harmonics remain the same order, but their harmonic amplitude increases. The winding factor of the main harmonic (i.e. of order ν=p=5) slightly increases.

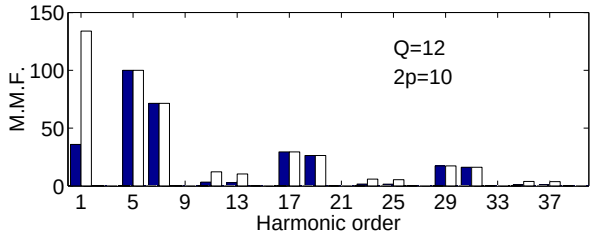

Figure 7.9: MMF harmonic contents of 12–slot 10–pole motor (black bars refer to double–layer winding, white bars refer to single–layer winding)

7.4.1 Measurement of subharmonic EMF

For the sake of experimenting the presence of subharmonic and its different value when a double– and a single–layer winding is adopted, a 2–pole rotor has been introduced into the two stators. Since the winding factor of order one (i.e. corresponding to two poles) is not zero for both of them, a EMF is induced in the windings. Its waveform is shown in Fig. 7.10. The EMF induced in the single–layer winding is more than three times higher than the EMF induced in the double–layer winding, verifying the prediction reported in Fig. 2.7(a).

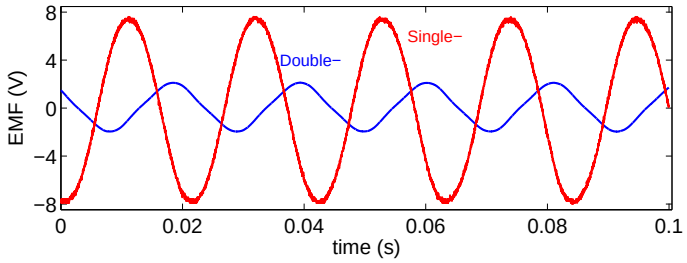

Figure 7.10: Back EMF induced in the stator single– and double–layer windings by a 2–pole rotor (experimental test).

7.4.2 Measurement of EMF and torque

In order to verify the increase of winding factor, the back EMF has been measured in both windings. The same 10–pole rotor of Fig. 7.3 has been used for the test of the two stators. The measured back EMFs are reported in Fig. 7.11. Actually, they have the same waveform, while the amplitude of the single–layer winding is slightly higher. Theoretically an amplitude 3.5 % higher is expected, equal to the ratio of the winding factors.

A further confirmation is given by the torque vs. current characteristic. The torque at different stator currents has been measured, as reported in Fig. 7.12. Actually, the two motors shown the same characteristic. It is worth noticing that the motor with single–layer winding exhibits a higher torque at nominal current (about 2 A). However, it is mainly affected by the iron saturation: when the current increases, the torque of the single–layer winding motor becomes lower than the torque of the other motor (see the torque at current higher than 5.5 A).

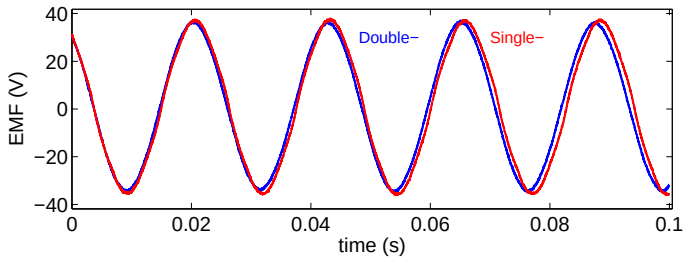

Figure 7.11: Back EMF induced in the two stator windings by the 10–pole rotor (experimental test).

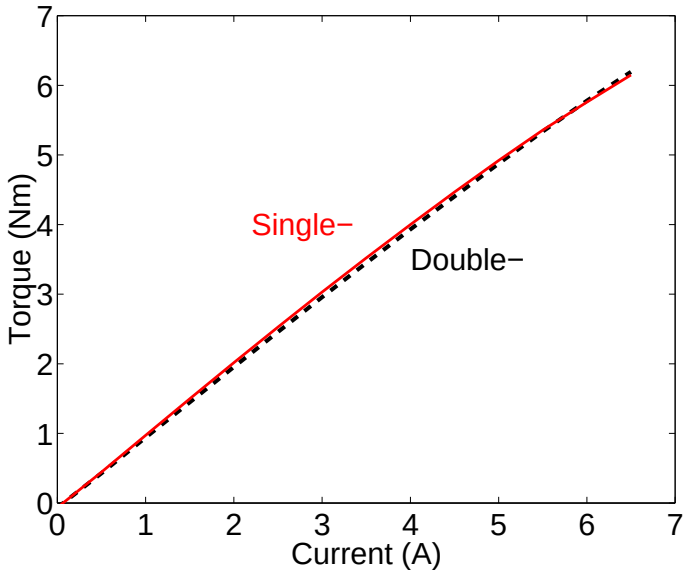

Figure 7.12: Torque versus current with double–layer (dashed line) and single–layer (solid line) windings

7.5 Mutual inductance equal to zero

If the fractional–slot winding has to be designed for fault–tolerant applications a common requirement is that the mutual coupling among the phases is zero, i.e. M=0. This is to avoid the interaction between the healthy and the faulty phases.

To this purpose, windings with non–overlapped coils (i.e. with a unity coil throw $y_q = 1$) are firstly adopted.

Secondly, the winding of each phase can be split in couples of coils producing rectangular–shaped MMF distributions of opposite sign. The positive contribution of one coil is compensated by the negative contribution of the other coil. Therefore the resulting MMF distribution is zero in any point not embraced by these two coils. An example is shown in Fig. 7.13 that reports the armature MMF distribution due to only one phase of a 12–slot 10–pole machine. The MMF is different from zero only in correspondence of the supplied coils.

7.5.1 General rule to achieve M=0

A general rule can be found to achieve a winding with no coupling among the phases. The mutual inductance M results to be zero when Q/t is even with a double–layer winding, and when $Q/(2t)$ is even with a single–layer winding. This general result is also reported in Table 2.1.

The examples mentioned above belong to this group. They can be located in the Table 2.1. In fact all of them have y_q=1 and Q/t even. In the case of single–layer winding, they show $Q/(2t)$ even so as M=0 as well.

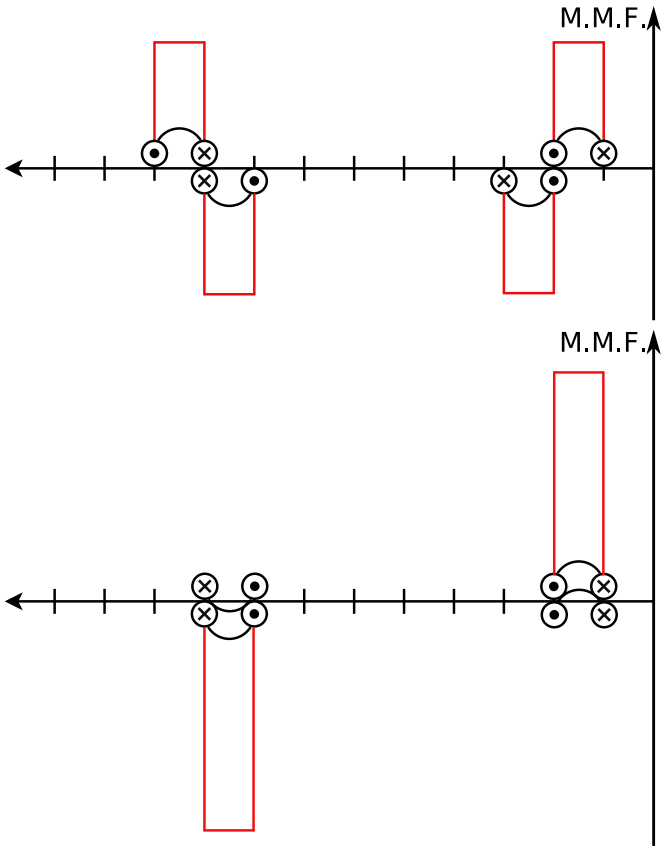

Figure 7.13: Armature MMF distribution of a 12–slot 10–pole (with $M = 0$) and of a 12–slot 8–pole motor (with $M \neq 0$) RIFARE

7.5.2 Measurement of mutual coupling among the phases

In order to verify the absence of mutual coupling among the phases, the coils of one phase have been supplied by an alternating voltage and the voltage induced in the coils of the adjacent phase has been measured. The measured voltages are reported in Fig. 7.14 for the double–layer winding and in Fig. 7.15 for the single–layer winding. As expected, the induced voltage is zero for both windings.

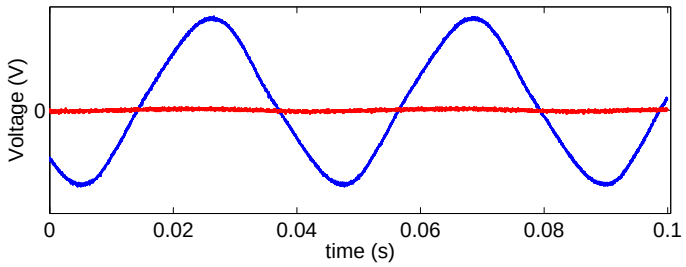

Figure 7.14: Measured voltages: in the supplied phase and in the adjacent open–circuited phase (double–layer winding)

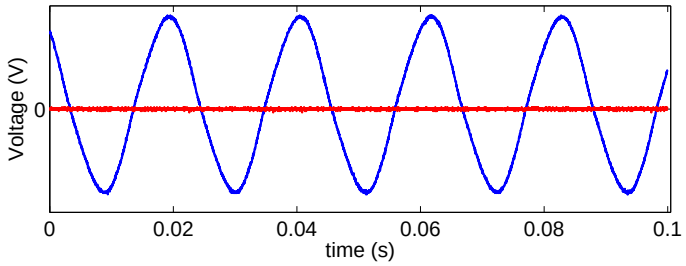

Figure 7.15: Measured voltages: in the supplied phase and in the adjacent open–circuited phase (single–layer winding)

7.6 Double inverter

For increasing the fault-tolerance of the drive two inverters supply the motor. This choice increases the price of the system but in case of fault of one inverter as shown in Fig.7.16, the motor can operate even in case of fault. The winding changes as shown in Fig.7.17, but the symmetry of the machine is guaranteed, therefore no radial force appears.

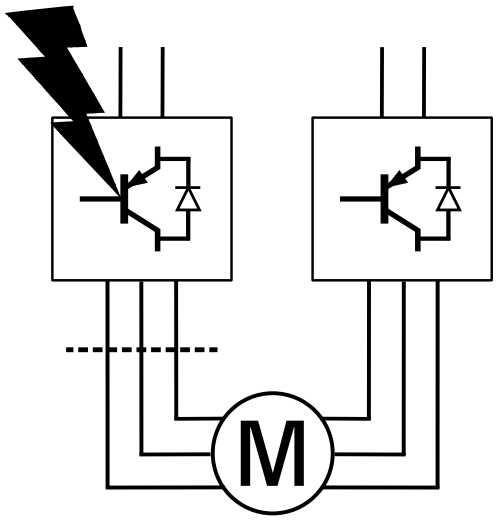

Figure 7.16: Fault–tolerant scheme: two 3-phase inverter and the 12 slot 10 pole motor

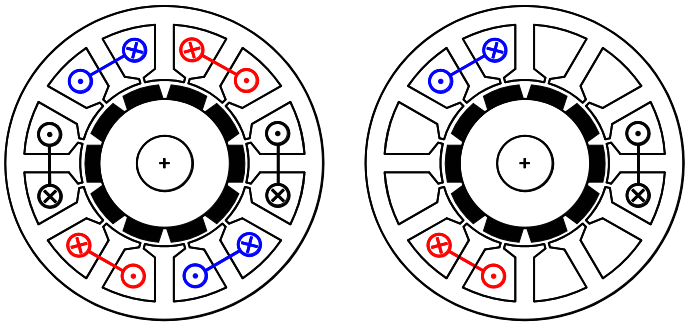

Figure 7.17: 12 slot 10 pole motor: healthy and faulty solution

Fig.7.18 shows the torque vs. angular position in healthy mode operation. The mean torque is 2.4 Nm. When the fault appears the mean torque is halved and it remains quite flat as shown in Fig.7.19

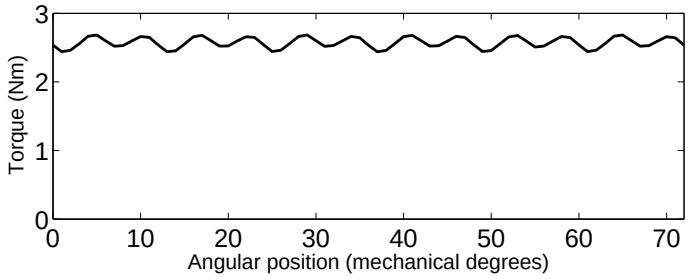

Figure 7.18: 12 slot 10 pole motor: healthy solution

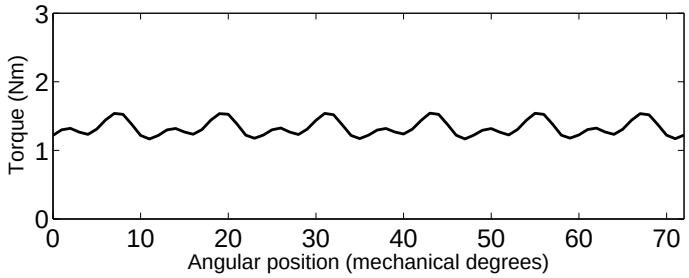

Figure 7.19: 12 slot 10 pole motor: faulty solution

7.7 Conclusions

This chapter would claim to be a valid help for the choice of the more suitable combination of slots and pole of a synchronous fractional–slot machine with non–overlapped coils. Several issues have been considered, among them the double– and single–layer winding, the MMF harmonic order, the zero mutual coupling among the phases, the peak magnetic potential due to the stator currents, and so on. Some reference tables are reported, summarizing the key performance of the fractional–slot motors. The suggestions of the tables are commented in the chapter and verified by means of examples and measures.

Part III

Design concepts of a wave generator

Chapter 8

Wave Generator

This chapter reports the results of my activity during the period spent at ABB Corporate Research, and my contribution to the EU project: Sustainable Economically Efficient Wave Energy Converter (SEEWEC). My physical duty was the analysis and design of the innovative electrical generator.

New concepts for the direct conversion of the movement of a vertical heaving buoy point absorber to electricity are presented in this chapter. The low loss direct conversion and generation system without intermediate hydraulic system permits hereto unprecedented speed and force control flexibility of the buoy movement.

This chapter develops and studies concepts where the guide system of the buoy is mechanically directly connected to the electrical generator. This can be either a linear generator or a rotating generator with a gear mechanism. The energy conversion from the resulting buoy forces and buoy speed is direct into electrical energy without intermediate system. This approach is referred to as direct generation, or direct drive, since the power electronic converter connected to the generator needs actively to control speed and forces at all instances of time while following respectively damping the incoming waves.

Three solutions are compared: an induction generator with a rack-pinion linear to rotary motion conversion and a step-up gear, a high pole application specific permanent magnet (PM) generator with a belt-pulley linear to rotary conversion, and a linear PM generator mounted directly on the guide of the buoy. The linear generator is the least robust and most challenging in design, while the induction generator solution is found best due to its cost and maintenance advantages. The PM rotating generator solution shows the highest efficiency.

A 1:5 scaled test system using this direct conversion was installed at shore in real sea waves. Experimentally measured energy capture widths for wave-to-electricity in the range of 25% are reported.

8.1 Description of power take-off (PTO) systems

The attempt to convert of water wave energy into electrical energy has a long history and a vast plurality of technical approaches. One of the basic concepts is using point absorbers, whereby the movement of the buoy is converted into useful energy. In the present day 1:5 scaled model Fig. 8.1, five buoys are connected via a guide rod to a hydraulic pump, pipe and control system, all mounted on a platform. The hydraulic pressure is intended to turn a fixed speed generator that could be connected towards the grid directly.

Figure 8.1: Buldra wave energy converter test platform (1:5 model) with hydraulic PTO

Figure 8.2: Envisioned 1:1 prototype with 21 buoys and new energy conversion system

The guide system of the buoy is mechanically directly connected to the electrical generator (linear or rotating) without intermediate system. The power electronic converter connected to the generator needs actively to control speed and forces at all instances of time while following respectively damping the incoming waves.

Currently only the heaving motion (z-direction movement) is utilized. The 1:1 prototype (Fig. 8.2) is then to be equipped with a large number (presumably 21) of heaving buoys 8 with the most favorable PTO system. The main subsystems necessary for such a complete wave farm and the basic technical solutions for the direct generation system are discussed in the next sections.

8.2 Wave Farm system with direct drive PTO

To establish a common terminology and clarify the system environment and the specific sub-systems in this chapter, Fig. 8.3 shows the key components of an entire wave farm with direct drive energy take-off.

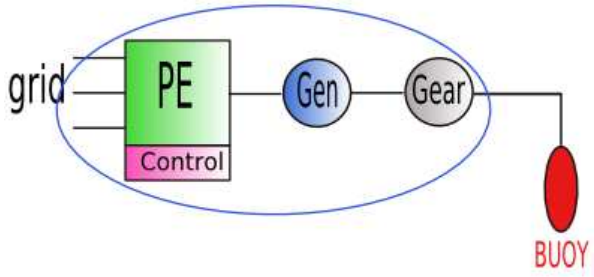

Figure 8.3: Complete Wave energy Farm Systems and sub-systems overview

The key system components are:

a) Plant control: The functions implemented here are for example related to the waves climate, the grid demand, the farm operation, the main platform and platform protection functions, operational status, land communication, etc. Only marginally addressed at this stage in this report.

b) Higher control loops: Power Flow, Energy optimization through maximum power tracking or dynamic (slow) model tuning. These functions may also include, high wave protection, and grid protection/interaction functions.

c) Lower control loops: These loops control the generator forces or torques, the buoy position, the guide speed, the mechanical accelerations, etc. Probably executed in the 1kHz to several kHz range for dynamic response reasons and are usually included in the electronics and software of the converter.

d) Buoy (or egg) point absorber.

e) Mechanical system to transport the energy from the buoy to the generator; this may include a gear that can include a mechanical transformation from a linear movement to a bi-directional or unidirectional rotating movement. This system may also include brakes or end-stops or other mechanical components only indirectly related to the actual conversion principle (but very relevant for survivability)

f) Electrical generator: Linear or rotating, utilizing various known electrical machine concepts.

g) Power electronic Converter on the generator side converter: This is the drive converter that controls the power take out from the buoy movement. It implements a generator control (PWM, Vector control, DTC) similar in flexibility to a robotic or other highly dynamic drive. The power electronics converts a variable voltage, variable current, variable frequency to DC power

h) Line side converter: This converter transforms the DC voltage to a AC voltage of fixed frequency (same as the grid). Many functions related to the grid, (reactive control, voltage support, voltage sag rid-through control, protections) are implemented here. Not discussed in this report.

8.3 Direct electric power conversion

Direct conversion was in the past avoided due to the overrating of the system compared to the average energy. One well known control principle with a claimed maximization of the energy take out from the wave would require a peak power handling of typically factor $4-7$ above the (RMS) rating of the system.

As it can be implemented in hydraulics where power flow smoothing is available much cheaper than after conversion to electricity, direct drive was avoided. Further, power electronic systems and their control techniques as used e.g. in robots may not have been available or sufficiently robust in the past. The direct drive system, however, allows eliminating the entire hydraulic system, and the associated comparatively low efficiencies and control complexity.

Active fully dynamic control of the generator force used to extract energy from the buoy movement is expected to open new ways to optimize the energy absorbed from the waves. It becomes possible to apply nearly arbitrary control concepts with any of speed, force, and position conditions on the buoy system simply by software choices. This is expected to improve the primary efficiency observed in practice significantly.

At this point, this primary energy take out from the wave i.e. from the wave energy to the buoy energy is still by far the dominating loss. The power electronics is fully rated, i.e. the fully electric energy from the generator flows through the drive and line side converter. While each generator requires it own drive converter to have full control of the primary power take out, a group of buoys or even a full platform requires only one line side converter. The drive converter supplies the variable frequency, voltage and current necessary to produce the desired generating force on the guide and buoy. The power electronic drive hardware is identical, for unidirectional or for bidirectional operation. This eliminates the need for a gear transforming the linear up and down movement to a unidirectional rotating movement, and opens the flexibility to use much further developed rotating generators rather than necessitating a linear electric generators.

The line side converter converts the DC power to fixed frequency grid power. This system, with one line converter and multiple drive converters is rather common

in industrial multi-axis applications such as robots or material handling equipment. Even axis control is very comparable to buoy control. As side remark is mentioned, that further research will need to investigate if and under which conditions one drive converter could control several buoy/generator units to further improve the economics of the wave farm.

This work aims to optimize the size of the generator and the converter of the described system only. However, that approach is based on an innovative but rather complicated counter-rotating electromagnetic arrangement to achieve unidirectional rotation only. No mention of force control, power take out optimization, dimensioning optimization, or efficiency is made.

8.4 Contrasting options of the linear and rotating generators

The last section established that the power electronic converters are identical fully-rated units for most generator approaches and that one converter for each buoy and generator is needed. Both unidirectional and bidirectional rotation or linear up and down movement are very similar handled in this direct drive concept. Of course the mechanical system, the system inertias, and other details do alter the concepts and exact ratings of converter and generator, the power extraction efficiency, etc., and each has its specific advantages.

The key advantage of constructing a specialized linear generator as sketch in Fig. 8.4 is that no mechanical conversion to rotating movement is needed and thereby eliminates gears and the associated efficiencies. However, a linear generator does require rather exact bearings and has high requirements on the mechanical stability. No bending moments are permitted, as otherwise the carefully chosen air gap of the generator cannot be maintained. Furthermore, the nature of the system and size of the selected buoys leads to rather high forces and low or even very low speeds during certain ranges of the wave operating cycle. Such linear generators do not exist on the commercial markets.

The dominant disadvantage of rotating direct generation as sketch in Fig. 8.5 is the need for a mechanical gear. The purpose of this gear is to transform the linear up and down movement of the buoy and guide into rotating motion. A number of options to achieve this are discussed in Section 8.8. This gear is an extra component and introduces cost and (a small) power loss. However, it may implement protection functions that handle the end-stop and other overload issues relevant for survivability. It also allows the use of well established technologies for the electric generator such as the robust induction generator manufactured in high volumes. The basic generator efficiency may also be higher for rotating generators driven by a gear due to more fortunate speed and force ratios. The dimensioning of two rotating generators options potentially suitable for this system are discussed in Sections 4.2.4 and 4.2.6 and the resulting systems in Section 5.4 and 5.6.

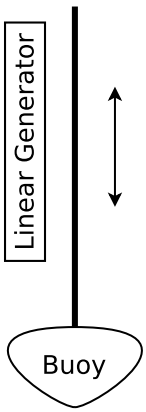

Figure 8.4: Linear generator

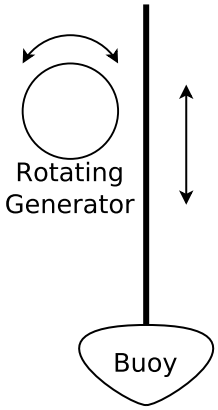

Figure 8.5: Rotating generator

Hence, at this early state of development, it is not possible to decouple the development of this level of control from the design of the generator and the preliminary power efficiency calculations. Two schematic structures are shown in Fig.8.4 and Fig.8.5 and is at that level identical for linear and rotating generator.

In summary, the hardware concept with buoy/guide, linear generator, alternative gear and rotating generator, and a fully rated converter for each buoy have been outlined as new power conversion concept for the new platform (Fig. 8.2). The crucial and iterative nature of researching for appropriate control as basic necessity

to learn about and establish the rating and operating conditions of this subsystem are established.

8.5 Requirements and operating conditions of PTO system

The preliminary simulation of the described power take-off, has even after the taken simplifications, probably in excess of many dozens parameters relevant for the system optimization efficiency of the power take-off. To avoid this impenetrable problem, more narrow specifications for the exact conditions for which the system is calculated are made in this chapter.

The buoy parameters, the wave parameters, the model approach, and the wave climate are all defined and restricted to as few cases as possible. Likewise, it is decided which few of the many possible mechanical and generator technological ideas from Chapter 4 are further investigated for the complete optimization and dimensioning. While this restricts the range and number of parameters significantly, the approach still allows pointing out possible areas, where different choices should have been made, or where another combination would have allowed further knowledge. The chosen approach was to gather these observations in the section for future work, so refinement for the chosen concepts can be made before the final report on this deliverable. These restrictions resulted in essentially one specific buoy, a dimensioning procedure for only 3representative waves, with one additional irregular wave as benchmark, one generalized algorithm of control but leaving some of the parameter space open, and only 3 chosen technology combinations for gear and generator. The converter technology was not varied as this is considered mature technology in this context.

8.6 The buoy

In a complete optimization the buoy plays one of the most crucial roles in the entire system. Primary are the mass/ weight, the buoyancy as controlled by the outer geometric shape some examples are shown in Fig.8.6, the free degrees of motion and limitations on the stroke length, and the shape determining the buoy water interaction. Candidate buoys were those optimized and calculated in an anther project. For the modeling of the PTO for the dimensioning of the electrical equipment, simplifying assumptions regarding the buoy shape can safely be made.

The buoys characteristic are reported in Tab. 8.6.

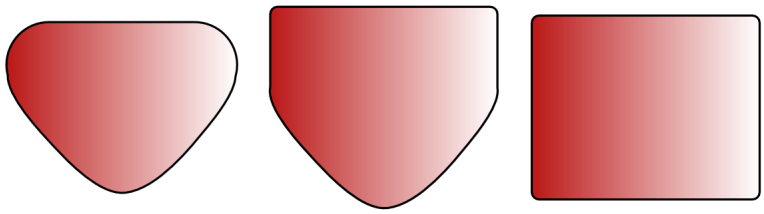

Figure 8.6: Defined buoy shapes for this work

Table 8.1: Buoys Characteristic

Buoys	Dimension
Diameter	4.5 m
Total Height	1.389 m
Mass	3000 kg
Free height above static waterline	1.2 m
Max stroke length	5 m
Volume	22.08 m^3
Static draft	0.189 m
Free buoyancy force	18723 N

8.7 The wave

Real waves feature rather complex traces versus time. While good statistical definitions exist essentially the entire literature reverts to regular waves (see Tab. 8.2), calculates under regular (linearized) motion assumptions. However, not only are irregular waves challenging to analyze, even statistically recreated wave amplitudes versus time at the absorber location are to difficult to track in a first step of the design and dimensioning of the PTO.

First, there is the Design Wave, whereby we have in mind to maximize the power efficiency and optimize the system at this wave condition. There is Minimal Wave, which represents the point in the wave climate where energy still is to be extracted. At lower waves than this, it is possible to turn-off the plant. There is also the Maximal Wave. At this point energy shall still be extracted, but the extraction efficiency does not need to be at the highest anymore. Rather conditions stemming from survivability aspects start to become relevant. At waves higher than the maximal wave, the plant is allowed to turn off and go to a save mode where no energy at all is extracted.

Table 8.2: Sinusoidal waves

Wave	Peak to Peak Amplitude	Wave Period
Design wave (optimal efficiency)	1.94 m	6.25 s
Minimal Wave for power take–off	0.88 m	4.75 s
Maximal Wave for power take–off	3.36 m	7.75 s

8.8 The mechanical converter

For extracting energy from the wave of the sea, there are two methods: the first one is to use a linear generator and the second one is to use a rotating generator. The rotary solution needs a system to transform the linear movement into rotating movement. So, the first step is to look at several mechanical solutions for changing the linear movement in rotating movement.This section explains the mechanics system, the key equations of the system and the pros and cons.

8.8.1 The rack and pinion mechanism

A rack and pinion set-up is a pair of gears which convert rotational motion into linear motion. The circular pinion engages teeth on a flat bar - the rack. Rotational motion applied to the pinion will cause the rack to move to the side, up to the limit of its travel. The rack and pinion arrangement is commonly found in the steering mechanism of cars or other wheeled, steered vehicles. This arrangement provides a lesser mechanical advantage than other mechanisms such as recirculating ball, but much less backlash and greater feedback, or steering "feel". The scheme of Fig. 8.7 shows one solution in where the buoy produces a linear movement of the rack. The pinion transforms the linear movement into rotating movement, and the radius of the pinion fixes the torque and the speed of the generator.

The system is controlled fron the equations 8.1. explains the

$$\begin{aligned} T - rF &= I\ddot{\theta} \\ F &= m\ddot{x} \end{aligned} \tag{8.1}$$

where:

T	is the input torque applied on the pinion
F	is the reaction force at the contact point between rack and pinion
I	is the rotational inertia of the pinion along the z-axis
r	is the pitch radius of the pinion
m	is the mass of the rack
θ	is the rotation angle of the pinion
x	is the translational displacement of the rack
$\ddot{\theta}$	is the angular acceleration of the pinion
$\ddot{x}$	is the linear acceleration of the rack

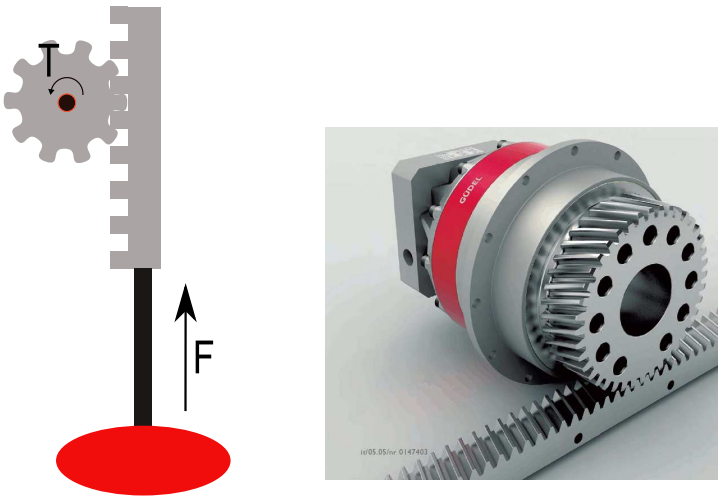

Figure 8.7: The rack and pinion mechanism: scheme and commercial solution

8.8.2 The ball-screw mechanism

A ball screw is a mechanical device for translating rotational motion to linear motion and vice versa. A threaded shaft provides a spiral raceway for ball bearings which act as a precision screw as shown in Fig.8.8(b). As well as being able to apply or withstand high thrust loads they can do so with minimum internal friction. They are made to close tolerances and are therefore suitable for use in situations in which high precision is necessary.

The ball assembly acts as the nut while the threaded shaft is the screw. While reducing friction, ball screws can operate with some preload, effectively eliminating backlash (slop) between input (rotation) and output (linear motion). This feature is essential when they are used in computer-controlled motion-control systems, e.g. CNC (computer numerical control) machine tools. To maintain their inherent accuracy and ensure long life, great care is needed to avoid contamination with dirt and abrasive

particles. This may be achieved by using rubber or leather bellows to completely or partially enclose the working surfaces. Another solution is to use a positive pressure of filtered air when they are used in a semi-sealed or open enclosure. Low friction in ball screws yields high mechanical efficiency compared to other alternatives. A typical ball screw may be 90% efficient. The higher cost of ball screws may thus be offset by lower power requirements for the same net performance. Due to their low internal friction, ball screws can be back-driven. Ball screw shafts may be fabricated by rolling, yielding a less precise, but inexpensive and mechanically efficient product. Rolled ball screws have a positional precision of several thousandths of an inch per foot. High-precision types are ground, and are typically precise to one thousandth of an inch per foot or better. Fig. 8.8 shows an example of the linear into rotating converter, the buoy pushes the screw and the nut with the rotor of the motor rotating. The effort of this solution is the small size of the system, on the other hand the cost the ball-screw yields less interesting this solution.

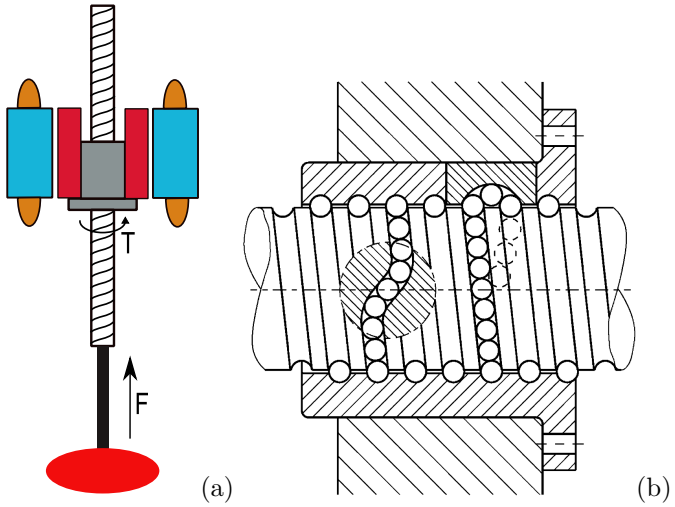

Figure 8.8: Mechanic scheme of the ball-screw system

The ball-screw system is reversible but with different efficiency when the mechanism transform the rotating movement into linear movement and vice versa. The ball-screw is characterized by the dimensions of the screw and the lead, when these two parameters are set the torque can be computed with the 8.2.

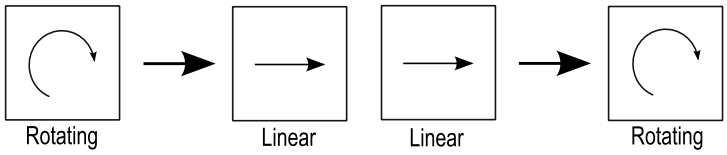

$$\eta = \frac{1}{1 + \frac{K d_0}{P_h}} \qquad \eta' = 2 - \frac{1}{\eta}$$

The dimensions of the ball–screw are determined thanks 8.2

$$T = \frac{F P_h}{2000 \eta \pi} \tag{8.2}$$

where:

K	is the ball screw constant (0.0180.02)
d_0	is the nominal screw diameter
P_h	is the lead
η	is the direct efficiency
η'	is the mass of the rack
θ	is the indirect efficiency
F	is the linear force
T	is the torque

8.8.3 The piston-crankshaft mechanism

A crank is a bent portion of an axle, or shaft, or an arm keyed at right angles to the end of a shaft, by which motion is imparted to or received from it. It is also used to change circular into reciprocating motion, or reciprocating into circular motion. Familiar examples of a crank for manual use include the crank on a manual pencil sharpener and the crankset that drives a bicycle via the pedals. Fig. 8.9 shows the functioning modalities of the system. Equations 8.3 explains the system movement. The maximum length of the system need to correspond to the maximum length of the wave. This system is able to have a complete rotation only with the maximum wave but with the other waves the rotation is not complete. In the following, the equations for determining the length of the component are reported.

$$\begin{aligned} C &= -M \cos\alpha + B \sin\beta \\ \beta &= \frac{M \sin\alpha}{B} \\ T &= FM \end{aligned} \tag{8.3}$$

8.8.4 The belt-pulleys mechanism

Belts are used to mechanically link two or more rotating items. They may be used as a source of motion, to transmit power at up to 98% efficiency between two points, or

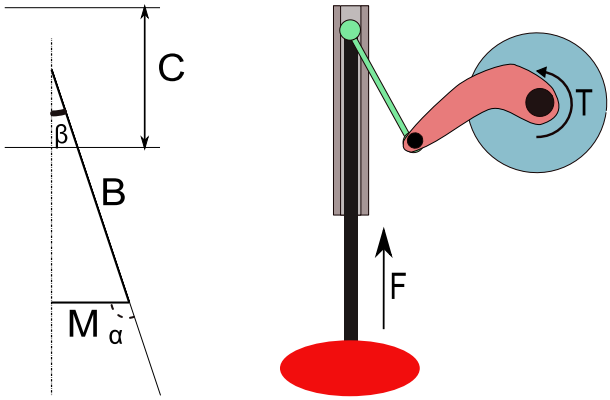

Figure 8.9: Piston system

to track relative movement. As a source of motion, a conveyor belt is one application where the belt is adapted to continually carry a load between two points. A belt may also be looped between two points so that the direction of rotation is reversed at the other point. Fig. 8.10 shows the mechanism that transform the linear to rotating movement; the belt is fixed to the buoys shaft and it transmits all the force. The equations of the system are the same as for the other solutions as shown in 8.4, where F is the force of the buoy, T the torque of the generator and r the radius of the wheel that transmits the torque to the generator.

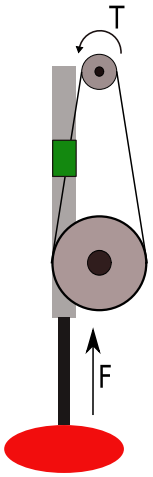

Figure 8.10: Belt system

$$T = Fr \tag{8.4}$$

To choose the proper belt solution for the considered application, a short description of the different belt system is provided. Power transmission is achieved by specially designed belts and pulleys. The demands on a belt drive transmission system are large and this has led to many variants.

- The earliest was the flat belt, used with line shafting. It is a simple system of power transmission that was well suited to its time in history. The flat belt also tends to slip on the pulley face when heavy loads are applied. In practice, such belts were often given a half-twist before joining, so that wear was evenly distributed on both sides of the belt.
- Round belts are a circular cross section belt designed to run in a pulley with a circular groove. They are for use in low torque situations and may be purchased in various lengths or cut to length and joined, either by a staple, gluing or welding.
- Vee belts are an early solution that solved the slippage and alignment problem. The "V" shape of the belt tracks in a mating groove in the pulley, with the result that the belt cannot slip off. The belt also tends to wedge into the groove as the load increases, the greater the load, the greater the wedging, action improving torque transmission and making the vee belt an effective solution. The belts can be supplied at various fixed lengths or as a segmented section, where the segments are linked to form a belt of the required length. For high-power requirements, two or more vee belts can be joined side-by-side in an arrangement called a multi-V, running on matching multi-groove sheaves.
- Timing belts (also known as Toothed, Notch or Cog) belts can track relative movement. These belts have teeth that fit into a matching toothed pulley. When correctly tensioned, they have no slippage and are often used to transfer direct motion for indexing or timing purposes.

Belts normally transmit power only on the tension side of the loop. However, designs for continuously variable transmissions exist that use belts that are a series of solid metal blocks, linked together as in a chain, transmitting power on the compression side of the loop.

Pros and cons of this solution are:

- elasticity: the robustness increases but the demand upon control of the system becomes more complicate;
- cheaper solution: the cost for the entire system is cheaper than the other solutions;
- maintenance is cheaper: the simple system means cheaper maintenance.

8.8.5 The friction wheel system

Fig. 8.11 shows a simple solution where two rubber wheels are pressed on the buoy shaft that transform the linear movement of the buoys into rotating movement. The movement is guaranteed to the friction of the rubber of the wheel on the shaft.

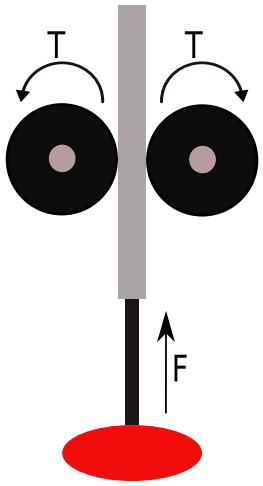

Figure 8.11: The friction wheel system

This solution has several problems. Rolling friction is the resistance that occurs when a tire rolls as shown in Fig. 8.12(a). It is much smaller than sliding friction. It is caused by the deformation of the wheel or tire or the deformation of the shaft. It depends very much on the material of the tire and the sort of shaft. It is classified under static friction because the patch of the tire in contact with the shaft, at any point, while the tire spins, is stationary relative to the ground. It is due to the different pressure of the wheel on the shaft and it is proportional to the speed of the wheel.

In addition, little slip occurs near the contact zone of the tire that increases the losses of the system.

Another problem is the maximum force applied to the system. When the force increases more than the maximum force value the wheel slips and the friction coefficient changes as shown in 8.12(b). The wear and tear of the tire need also considered.

8.8.6 The gear reduction mechanism

A gearbox is a system of gears that transmits mechanical power from a prime mover such as an engine or electric motor to some form of useful output device, usually, at a reduced rate of angular speed but at a higher shaft torque. Generally, transmissions

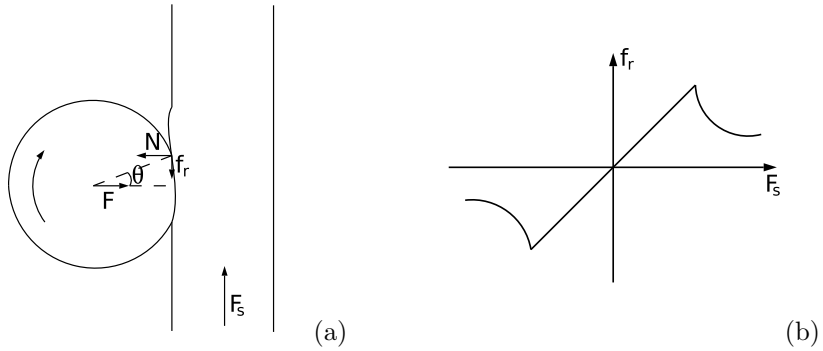

Figure 8.12: Rolling friction and friction factor

will provide a significant speed-power conversion known as gear reduction (in speed or torque) to a higher torque or speed. Two example of gear reduction are shown in Fig.8.13 and Fig.8.14.

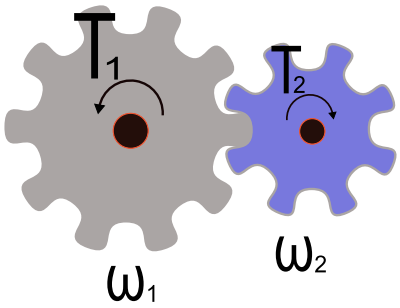

Figure 8.13: Gear reduction

8.8.7 Summary of gear options

In signs Table 8.7, a comparison between the above discussed solutions is made. The number of + increases with favorability.

8.9 The generator solutions

The generator design is aimed at having the physical dimensions and the performance parameter of the generator like the efficiency. The constant parameters are the nominal torque and the nominal speed for the thermal design, and the maximum force for the magnetic design. Different generator solution are presented. The first approach

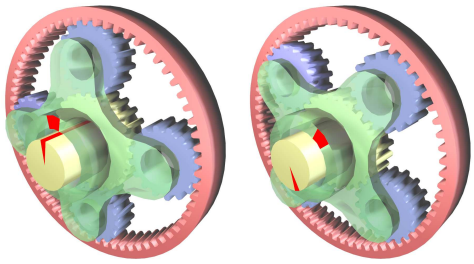

Figure 8.14: Epicyclic gearing

Table 8.3: Summary of gear options

Solutions	Efficiency	Weight	Control	Cost
Rack and pinion	0.96	++	++++	+++
Ball-screw	0.90	++++	++	+
Piston-crankshaft	0.95	+	+++	+++
Belt-pulley	0.96	+++	+	++++
Friction wheel	0.95	+++	+	++++

is to consider possibilities that are close to the wind generator concepts. This means that both gear and gearless solutions are considered.

8.9.1 The induction machine

The first solution is the induction generator (see Fig. 8.15) due to its robustness and its cost. However, the efficiency and the power factor are less than a PM motor. An optimization analysis is needed for choosing the best dimension of the generator for this application.

For designing the generator the application imposes several constrains: the motor can operate in flux weakening and the inertia of the system must be as less as possible. The design of the generator respects the input data (torque and speed) and several constrains. The typical parameters of the induction machine are reported in Table 8.4

A constrain of the wave generator is to operate with high speed and low force but also with low speed and high force, therefore the efficiency of the generator is not constant and Fig. 8.16 shows the map of the efficiency for different working point. The system is sensitive to inertia, so an optimization is necessary. The nominal frequency of the system and the power take off from the buoy is fixed. If the number of pole pairs increases the angular speed decreases as shown by 8.7, but the torque increases as shown by 8.8 and for each angular speed a suitable gear ratio is adopted. In addition the inertia of the rotor is proportional to the rotor diameter which depends upon the

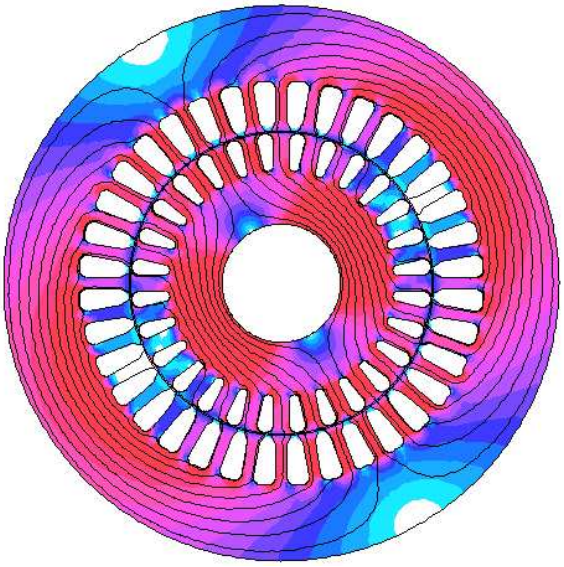

Figure 8.15: Induction generator

Table 8.4: Typical Induction Generator parameter

Typical Data	Value
K_s	30000 A/m
V	400 V
B_{gM}	0.8 T
J	6 A/mm^2
h_c	6
k_{fill}	0.4
η	0.90

torque.

$$P = T\omega \tag{8.5}$$

$$P_{gen} = T\omega\eta \tag{8.6}$$

$$\omega = \frac{2\pi f}{p} \tag{8.7}$$

$$T \propto p \tag{8.8}$$

$$T_i = I\dot{\omega} \tag{8.9}$$

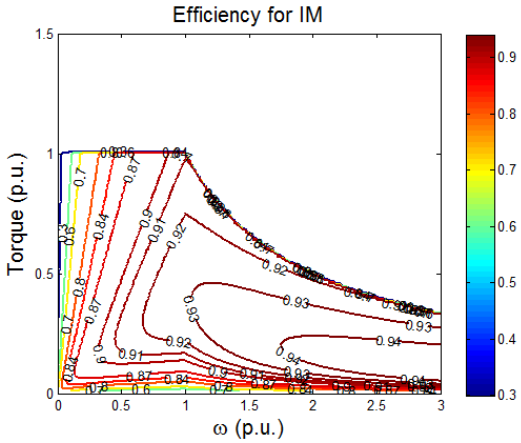

Figure 8.16: Measured voltages: in the supplied phase and in the adjacent open–circuited phase (single–layer winding)

8.9.2 The linear PM generator

The linear PM (see Fig. 8.17) generator is the most challenging solution being a non-mature variant compared to the commercial products. Even though it doesnt require a mechanical transducer and gear reduction, the robustness of the generator structure is a very serious issue. A PM generator is chosen because the power density and the efficiency are bigger than the other solutions. A tubular structure is investigated because a flat structure shows severe problems with structure stability. For this

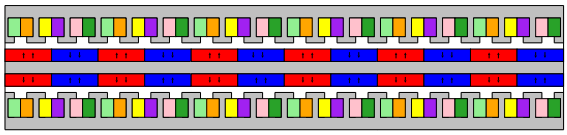

Figure 8.17: Linear PM generator

application an axial flux generator is chosen because it is the only relatively mature solution with a few industrial applications. The other PM configuration, the transversal flux generator has a low power factor and a more mechanically weak structure and is thus not considered.

For designing the linear generator the typical parameters are assumed stated below. For reducing the design dimensions the water cooling is adopted. So the parameters change as shown below:

Draw backs of linear generator are:

Table 8.5: Buoys Characteristic

Typical Data	Value
K_s	30000 A/m
V	400 V
B_{gM}	0.8 T
J	6 A/mm^2
h_c	6
k_{fill}	0.4
η	0.93
Water Cooling	
K_s	60000 A/m
J	12 A/mm^2

- the dimensions of the generator are quite big in comparison to the rotating generator because the dimensioning depends only upon the force. In the discussed application, the force is high but the speed is low therefore this results in a lower power to volume ratio.
- A section of either the stator or the translator of a linear machine is always inactive as shown in Fig. 8.18.
- There is a magnetic discontinuity both in the stator and in the translator, which reduces power transfer capability of end poles. The back iron and the poles requires a higher amount for reducing the saturation.

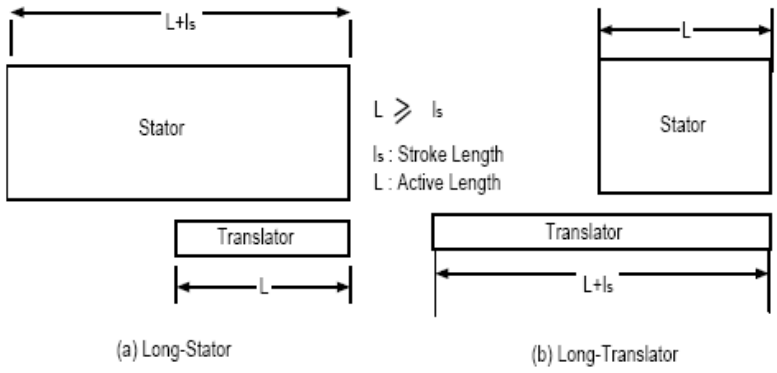

Figure 8.18: Linear machine definitions

8.9.3 The low speed PM generator

The low speed PM generator isnt a standard solution, but it is cheaper than traditional PM and it is a fault-tolerant solution. The high pole motor can be a fractional-slot winding motor with modular teeth. The weight of this generator is high because it produces high torque but with low speed. The cost for building the generator is decreased due to the modular structure. As regards the fault-tolerant capability, this generator allows the reduction of the possibility of the fault. The phases are physically separated, the mutual inductance is very low and the short circuit current is less than the traditional solutions.

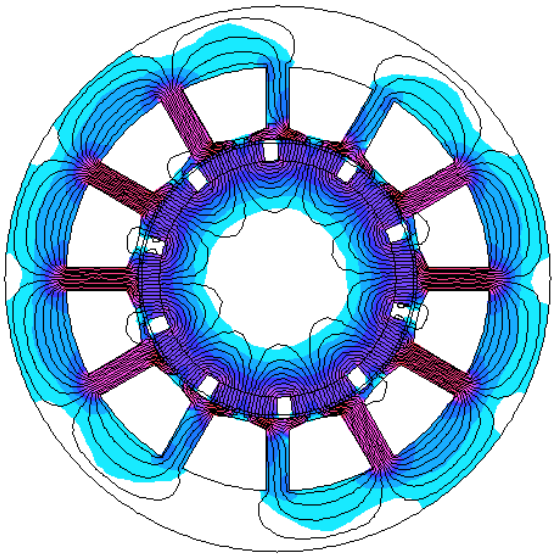

Figure 8.19: The low speed PM generator (SPM)

The flux-weakening capability is a constrain of this application so the surface mounted generator (see Fig. 8.19) is not suitable for this application. A single-layer winding with internal PM is proposed as shown in Fig. 8.20.

Fig. 8.21 shows the efficiency map of the generator for different working point.

The wave generator is sensitive of the inertia and this solution shows an high inertia due to the high number of poles therefore a low speed with high torque.

8.9.4 Summary

In Table 8.7, a comparison between the above discussed solutions is made. The number of + signs increases with favorability.

Table 8.6: Buoys Characteristic

Typical Data	Value
K_s	30000 A/m
V	400 V
B_{gM}	0.8 T
J	6 A/mm^2
h_c	6
k_{fill}	0.4
η	0.95

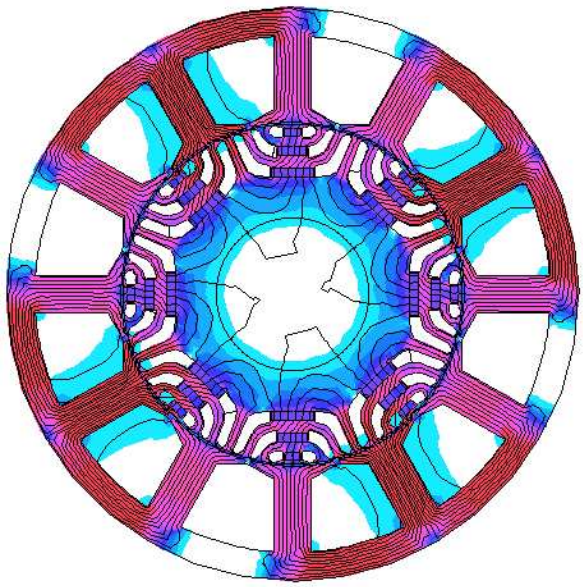

Figure 8.20: The low speed PM generator (IPM)

From Table 8.7 it can be seen, that the induction machine is the best compromise for the discussed application. It has the lowest weight, is very cheap and quite robust. Unfortunately, the efficiency is less than the other solutions, and a slightly bigger converter may be required.

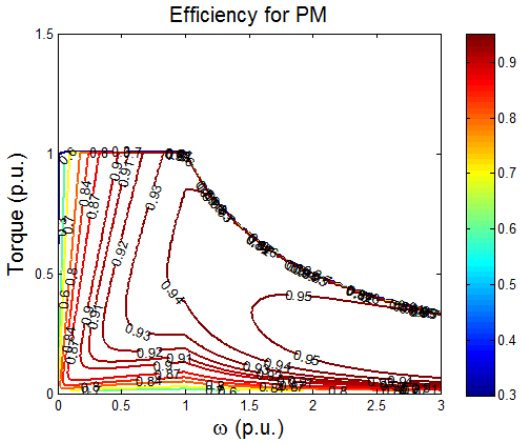

Figure 8.21: Efficiency map of the PM generator

Table 8.7: Summary of gear options

Solutions Generator	Efficiency	Weight	Dimension of the converter	Robustness	Cost
Induction	0.90	++++	++	++++	++++
Linear	0.93	++	++	+	+
PMHP	0.95	+	+++	++	++

8.10 Concept System

The different generator solution possibilities are mentioned but only the more applicable solutions are discussed in details. Three solution are proposes:

- induction generator with two step gear and standard components, see Fig. 8.22; This solution is the cheapest solution because it uses standard components. In order to minimize the generator dimensions and the torque inertia a 2 pole pairs generator is used. The mechanical transducer is a rack and pinion plus a gear box.

Figure 8.22: Standard components solution

- linear PM generator, gear less, see Fig. 8.23; This solution is a true direct drive solution because it has no mechanical transformation of the movement. The buoy produces a big force and the speed of the system is low, so the power is the same as that of the previous solution but the dimensions of the generator are increased.

Figure 8.23: linear PM generator solution

- low speed generator with single step gear, see Fig. 8.24. This solution is a mix of the previous solutions, it needs only a mechanical converter from linear into rotating movement then it characterized to low speed and high dimensions.

Figure 8.24: Low speed generator

The generator parameter and performance are reported in Tables 8.8, 8.9 and 8.10. As regard the maximum energy extraction , the tables highlight that the best solution is the low speed PM generator. Its efficiency and its $\cos\varphi$ allows to choose an inverter with lower VA rating than the other solution. On the other hand the low speed of the generator involves that the dimension of the generator are greater than the other solutions.Therefore the first realistic solution is the induction generator due to its robustness and costs.

Table 8.8: Generator performance

Generator	*Power* (kW)	*Speed*	η	$\cos\varphi$	I_n (A)	T_n/F_n	T_{max}/T_n F_{max}/F_n
Induction	37	1475 rpm	0.93	0.85	68	240 Nm	3.1
Linear PM	32	0.475 m/s	0.93	0.68	69	67 N	3
Low speed PM	32	49.2 rpm	0.95	0.9	52	6077 N	3

Table 8.9: Mechanical parameters of the generator

Generator	$Inertia$ (kgm^2)	$Whight$ (kg)	D_{est} (mm)	L_{est} (mm)
Induction	0.32	216	386	698
Linear PM	/	825	220	2480
Low speed PM	96	1538	1186	334

Table 8.10: Inverter characteristic

Generator	$Power$ (kVA)	V_n (V)	I_n (A)	$Weight$ (kg)
Induction	90	$380-480$	180	69
Linear PM	110	$380-480$	180	69
Low speed PM	75	$380-480$	180	69

8.11 Conclusion

This chapter would claim a comparison among several solution for an innovative and efficient wave energy converter. Different mechanical converters and generator have been compared. The innovative aspects and the innumerable unknown problems of this application impose to chose a commercial solution. Therefore a commercial IM motor and inverter will be adopted on the 1:1 prototype (Fig. 8.2).

8.12 Acknowledgment

This work was financed by the EU SEEWEC (Sustainable Economically Efficient Wave Energy Converter). Author is very grateful to Dr. Heinz Lendenmann and Dr. Freddy Magnussen (ABB Corporate Research, Sweden) for the opportunity to work to this project.

My Publications

1. Nicola Bianchi, Silverio Bolognani, Giorgio Grezzani and Michele Dai Pré, "Impact of Soft Magnetic Materials to the Electrical Machines Design" *Proc. of ANAE Conference*, Bressanone (TN), Italy, 5-7 March 2005, p.1-21

2. Nicola Bianchi, Michele Dai Pré, Giorgio Grezzani, and Silverio Bolognani, "Design considerations on fractional-slot fault-tolerant synchronous motors", *in Proc. of IEEE International Electric Machines and Drives Conference, IEMDC'05*, San Antonio, Texas, 15-18 May 2005, p.902-909.

   republished as

   Nicola Bianchi, Michele Dai Pré, Giorgio Grezzani, and Silverio Bolognani, "Design considerations on fractional-slot fault-tolerant synchronous motors", in *IEEE Trans. on Industry Applications*, Vol. 42, No. 4, July-August 2006, pp. 997-1006.

3. Nicola Bianchi, Diego Bon, and Michele Dai Pré, "Investigation of fault-tolerant IPM motors for critical applications", *in Proc. of Power Convereter, Intelligent Motion Europe Conference, PCIM 2005*, Nrnberg, Germany, 7 - 9 June 2005, 6 pages, CD-Rom.

4. Nicola Bianchi, Silverio Bolognani and Michele Dai Pré, "Design of a fault-tolerant IPM motor for electric power steering" *in Proc. of IEEE Power Electronics Specialist Conference, PESC'05*, Recife, Brazil, 13-16 June 2005, pp.2873-2880.

   republished as

   Nicola Bianchi, Silverio Bolognani and Michele Dai Pré, "Design of a fault-tolerant IPM motor for electric power steering" *in IEEE Trans. on Vehicular Technology*, Vol. 55, No. 4, July 2006, pp.1102-1111.

5. Angela Benedetti, Nicola Bianchi, Silverio Bolognani, Michele Dai Pré, Pier-Gabriele Molari, Piero Morelli, Matteo Tomasini, Luca Tubiana, and Mauro

Zigliotto, "PM Motor Drives for Steer-by-Wire Applications", *in Proc. of IEEE Industry Applications Society Meeting, IAS'05*, Hong-Kong, China, 2 - 6 Oct 2005, pp. 2857-2864.

accepted for republication as

Nicola Bianchi, Silverio Bolognani, Michele Dai Pré, Matteo Tomasini, Luca Peretti, and Mauro Zigliotto, "PM Motor Drives for Automotive Steer-by-Wire", *in IEEE Magazine on Industry Applications*, Vol. –, No. –, March 2008, pp.–

6. Nicola Bianchi and Michele Dai Pré, "Use of the star of slots in designing fractional-slot single-layer synchronous motors", *in IEE Proc., Electric Power Applications*, (online EPA no. 2005-0284), Vol.153, No.3, May 2006, pp. 459-466.

7. Nicola Bianchi, Silverio Bolognani, Michele Dai Pré, "Design and Tests of a Fault-Tolerant Five-Phase Permanent Magnet Motor", *in Proc. of IEEE Power Electronics Specialist Conference, PESC'06*, Jeju, Korea, 18-22 June 2006, pp.2540-2547.

8. Nicola Bianchi, Silverio Bolognani, Michele Dai Pré, "Strategies for the Fault-Tolerant Current Control of a Five-Phase Permanent-Magnet Motor", *in IEEE Trans. on Industry Applications*, Vol. 43, No. 4, July/August 2007, pp.960-970.

9. Nicola Bianchi, Silverio Bolognani, Diego Bon, and Michele Dai Pré, "Torque Harmonic Compensation in a Synchronous Reluctance Motor", *in Proc. of IEEE Power Electronics Specialist Conference, PESC'06*, Jeju, Korea, 18-22 June 2006, pp.1689-1694.

   accepted for republication as

   Nicola Bianchi, Silverio Bolognani, Diego Bon, and Michele Dai Pré, "Torque Harmonic Compensation in a Synchronous Reluctance Motor", *in IEEE Trans. on Energy Conversion*, Vol. , No. , month 2008, pp. - .

10. Nicola Bianchi, Silverio Bolognani, Michele Dai Pré, "Magnetic loading of fractional-slot three-phase PM motors with non-overlapped coils", *in Conf. Records of the 41st IEEE IAS Annual Meeting*, Tampa Florida, 8-12 October, 2006, CD Rom 9 pages.

    accepted for republication as

    Nicola Bianchi, Silverio Bolognani, Michele Dai Pré, "Magnetic loading of fractional-slot three-phase PM motors with non-overlapped coils", *in IEEE Trans. on Industry Applications*, Vol. , No. , month 2008, pp. - .

11. Nicola Bianchi, Silverio Bolognani, Diego Bon, and Michele Dai Pré, "Rotor flux-barrier design for torque ripple reduction in synchronous reluctance motors", *in Conf. Records of the 41st IEEE IAS Annual Meeting*, Tampa Florida, 8-12 October, 2006, CD Rom 8 pages.

12. Nicola Bianchi, Michele Dai Pré, Luigi Alberti, Emanuele Fornasiero, "Theory and Design of Fractional-Slot PM Machines", *Tutorial Course Notes, sponsored by the IEEE-IAS Electrical Machines Committee*, presented at the IEEE IAS Annual Meeting, 23 September 2007, pages 195.

Bibliography

[1] N. Bianchi and S. Bolognani, "Parameters and volt–ampere ratings of synchronous motor drive for flux–weakening applications," *IEEE Transactions on Power Electronics*, vol. 12, pp. 895–903, Dec 1997.

[2] N. Bianchi and M. D. Pré, "Use of the star of slots in designing fractional–slot single–layer synchronous motors," *IEE Proc. – Electr. Power Appl.*, vol. 153, no. 3, pp. 459–466, May 2006, (online no. 20050284).

[3] A. Jack, B. Mecrow, and J. Haylock, "A comparative study of permanent magnet and switched reluctance motors for high–performance fault–tolerant applications," *IEEE Trans. on Industry Applications*, vol. IA–32, no. 4, pp. 889–895, July/Aug 1996.

[4] N. Bianchi, M. D. Pré, G. Grezzani, and S.Bolognani, "Design Considerations on Fractional–Slot Fault–Tolerant Synchronous Motors," *IEEE Trans. on Industry Applications*, vol. 42, no. 4, pp. 997–1006, 2006.

[5] J. Cros, P. Viarouge, and A. Halila, "Brush dc motors with concentrated windings and soft magnetic composites armatures," in *Conf. Rec. of IEEE Industry Applications Annual Meeting, IAS'01*, vol. IV, Chicago, 30 September – 4 October 2001, pp. 2549–2556.

[6] A. Mitcham, G. Antonopoulos, and J. Cullen, "Favourable slot and pole number combinations for fault–tolerant PM machines," *IEE Proc. – Electr. Power Appl.*, vol. 151, no. 5, pp. 520–525, Sept. 2004.

[7] F. Magnussen, P. Thelin, and C. Sadarangani, "Performance Evaluation of Permanent Magnet Synchronous Machines with Concentrated and Distributed Winding Including the Effect of Field Weakening," in *in Proc. of 2nd IEE International Conference on Power Electronics, Machines and Drives (PEMD 2004)*, vol. 2, March 31 – April 2, 2004, pp. 679–685.

[8] F. Magnussen and H. Lendenmann, "Parasitic Effects in PM Machines with Concentrated Windings," in *Conf. Rec. of 40th IEEE Industry Applications Annual Meeting, IAS'05*, vol. 2, Kowloon, Hong–Kong, 2–6 October 2005, pp. 1044–1049.

[9] N. Schofield, K. Ng, Z. Zhu, and D. Howe, "Parasitic rotor losses in a brushless permanent magnet traction machine," in *Proc. of Electric Machine and Drives Conference, EMD97*, I. C. No.444, Ed., 1–3 Sept. 1997, pp. 200–204.

[10] A. El-Refaie, T. Jahns, P. McCleer, and J. McKeever, "Experimental Verification of Optimal Flux Weakening in Surface PM Machines using Concentrated Windings," *IEEE Trans. on Industry Applications*, vol. 42, no. 2, pp. 443–453, March/April 2006.

[11] A. El-Refaie, T. Jahns, and D. Novotny, "Analysis of Surface Permanent Magnet Machines with Fractional–Slot Concentrated Windings," *IEEE Trans. on Energy Conversion*, vol. 21, no. 1, pp. 34–43, March 2006.

[12] N. Bianchi, *Electrical Machine Analysis using Finite Elements*, ser. Power Electronics and Applications Series, CRC, Ed. Boca Raton, FL, USA: CRC Press, Taylor & Francis Group, 2005.

[13] D. Ishak, Z. Zhu, and D. Howe, "Permanent–magnet brushless machines with unequal tooth widths and similar slot and pole number," *IEEE Trans. on Industry Applications*, vol. 41, no. 2, pp. 584–590, March/April 2005.

[14] B. Welchko, T. Jahns, W. Soong, and J. Nagashima, "IPM synchronous machine drive response to symmetrical and asymmetrical short circuit faults," *IEEE Transactions on Energy Conversion*, vol. EC–18, pp. 291–298, Jun. 2003.

[15] T. Jahns, *Design, Analysis, and Control of Interior PM Synchronous Machines (N. Bianchi, T.M. Jahns editors)*. IEEE IAS Tutorial Course notes, IAS Annual Meeting, CLEUP, Seattle, October 3, 2005, ch. *Fault-mode operation*, pp. 10.1–10.21, (info@cleup.it).

[16] N. Bianchi, S.Bolognani, and G. Grezzani, "Fractional-slot IPM servomotors: analysis and performance comparisons," in *Proc. of International Conference on Electrical Machines, ICEM'04*, vol. CD Rom, paper no. 507, Cracow, Poland, 5–8 Sept. 2004, pp. 1–6.

[17] T. M. Jahns, "Improved reliability in solid state a.c. drives by means of multiple independent phase–drive units," *IEEE Trans. on Industry Applications*, vol. IA–16, no. 3, pp. 321–331, May 1980.

[18] L. Parsa and H. Toliyat, "Fault–tolerant five–phase permanent–magnet motor drives," *Proc. of IEEE Industry Applications Annual Meeting*, pp. 1–7 (CD–Rom), October 3–7, 2004.

[19] ——, "Five–phase permanent–magnet motor drives," *IEEE Trans. on Industry Applications*, vol. 41, no. 1, pp. 30–37, Jan/Feb 2005.

[20] D. Diallo, M. Benbouzid, and A. Makouf, "A fault tolerant control architecture for induction motor drives in automotive applications," *IEEE Transactions on Vehicular Technology*, vol. 53, no. 6, pp. 1847–1855, November 2004.

[21] J. Haylock, B. Mecrow, A. Jack, and D. Atkinson, "Operation of fault tolerant PM drive for an aerospace fuel pump application," *IEE Proc. – Electr. Power Appl.*, vol. 145, no. 5, pp. 441–448, Sept. 1998.

[22] M. Lazzari and P. Ferrari, "Phase number and their related effects on the characteristics of inverter–fed induction motor drives," in *Conf. Rec. of IEEE Industry Applications Annual Meeting, IAS'83*, vol. 1, Mexico City, Mexico, October 1983, pp. 494–502.

[23] G. Singh and V. Pant, "Analysis of a multiphase induction machine under fault condition in a phase–redundant ac drive system," *Electric Machines and Power Systems*, vol. 28, no. 6, pp. 577–590, Dec. 2000.

[24] N. Bianchi, S. Bolognani, and M. D. Pré, "Design and tests of a fault–tolerant five–phase permanent magnet motor," in *Proc. of IEEE Power Electronics Specialist Conference, PESC'06*, Jeju, Korea, 18–22 June 2006, pp. 2540–2547.

[25] C. French, P. Acarnley, and A. Jack, "Optimal torque control of permanent magnet motors," in *Proc. of International Conference on Electrical Machines, ICEM'94*, vol. 1, Paris (F), 5–8 Sept. 1994, pp. 720–725.

[26] T. Gobalarathnam, H. Toliyat, and J. Moreira, "Multi–phase fault–tolerant brushlerss dc motor drives," in *Conf. Rec. of IEEE Industry Applications Annual Meeting, IAS'00*, vol. 2, Rome (Italy), 2000, October 8–12, pp. 1683–1688.

[27] J. Wang, K. Atallah, and D. Howe, "Optimal torque control of fault–tolerant permanent magnet brushless machines," *IEEE Trans. on Magnetics*, vol. 39, no. 5, pp. 2962–2964, September 2003.

[28] J. Ede, K. Atallah, J. Wang, and D. Howe, "Effect of optimal torque control on rotor loss of fault–tolerant permanent magnet brushless machines," *IEEE Trans. on Magnetics*, vol. 38, no. 5, pp. 3291–3293, September 2002.

[29] B. Mecrow, A. Jack, D. Atkinson, G. Atkinson, A. King, and B. Green, "Design and testing of a four–phase fault–tolerant permanent–magnet machine for an engine fuel pump," *IEEE Trans. on Enegy Conversion*, vol. 19, no. 4, pp. 671–678, December 2004.

[30] M. Liwschitz-Garik and C. C. Whipple, *Electric Machinery, vol.II, A–C Machines*. New York: D. Van Nostrand Company Inc., 1960.

[31] J. Wang, Z. Xia, and D. Howe, "Analysis of three–phase surface–mounted modular permanent magnet machines," in *Proc. of IEE International Conference on*

Power Electronics, Machines and Drives (PEMD'04), Edinburgh, UK, March 31 – April 2, 2004, pp. CD–Rom.

[32] D. Ishak, Z. Zhu, and D. Howe, "Unbalanced magnetic forces in permanent magnet brushless machines with diametrically asymmetric phase windings," in *Conf. Rec. of 40th IEEE Industry Applications Annual Meeting, IAS'05*, vol. 2, Kowloon, Hong–Kong, 2 – 6 October 2005, pp. 1037–1043.